UNIVERSITY OF CALIFORNIA
SANTA CRUZ

SEARCH FOR HIGGS BOSONS PRODUCED VIA VECTOR BOSON FUSION AND DECAYING TO A PAIR OF B-QUARKS IN ASSOCIATION WITH A HIGH-ENERGY PHOTON IN THE ATLAS DETECTOR AT THE LARGE HADRON COLLIDER

A dissertation submitted in partial satisfaction of the
requirements for the degree of

DOCTOR OF PHILOSOPHY

in

PHYSICS

by

Carolyn M. Gee

March 2023

The Dissertation of Carolyn M. Gee
is approved:

Professor Jason Nielsen, Chair

Professor Michael Hance

Professor Bruce Schumm

Peter Biehl
Vice Provost and Dean of Graduate Studies

Contents

List of Figures

List of Tables

Abstract

Search for Higgs bosons produced via vector boson fusion and decaying to a pair of b-quarks in association with a high-energy photon in the ATLAS detector at the Large Hadron Collider

by

Carolyn M. Gee

A search for the Standard Model Higgs boson produced in association with a high-energy photon is performed using 132 fb^{-1} of pp collision data at $\sqrt{s} = 13$ TeV collected with the ATLAS detector at the Large Hadron Collider. This dissertation presents a complete analysis of the vector boson fusion production mode of the Higgs boson, which is a particularly powerful channel for studying the $H(\to b\bar{b})+\gamma$ final state because the photon requirement greatly reduces the multijet background and because the Higgs boson decays primarily to bottom quark-antiquark pairs. Extending and updating background Monte Carlo samples, training a neural network to distinguish between signal and background events, and optimizing binned-liklihood signal and background model fitting techniques are new strategies used in this analysis.

To Ye-ye, Nyin-nyin, Po-po, and Gong-gong, who always valued learning.

Acknowledgments

Thanks to Jason Nielsen for your advising, encouragement, and for sharing your passion for particle physics. Thank you to Bruce Schumm and Michael Hance, for serving as my committee members and for your guidance about ATLAS and silicon sensors.

Thank you to ATLAS advisors Hartmut Sadrozinski and Abe Seiden, for your mentorship and counsel in ATLAS instrumentation and sensors. Thank you to the ATLAS post-docs and scientists Giordon Stark, Matthew Gignac, Andrea Sciandra, and Simone Mazza for helping me learn the ropes of ATLAS. Thanks to ATLAS graduate students Jake Pasner and Natasha Woods for helping me join and navigate the ATLAS group, and to ATLAS officemates Cole Helling, Nathan Kang, and Yuzhan Zhao for making the office a fun and productive place to work. Thanks especially to Hava Schwartz for your friendship and for collaborating closely with me on the VBF $H(b\bar{b}) + \gamma$ legacy analysis that makes up the bulk of this thesis, including many results and a number of the plots shown. Thanks to ATLAS collaborator Matthew Klein for your helpful advice and assistance with all things related to $H(b\bar{b})$.

Thanks to Nora Norvell, for your encouragement during tough classes, long research problems, and dissertation writing to work towards the goal of becoming Doctors of Philosophy in Physics together. A pact with Nora was made the first month of graduate school that 100% of the women in our cohort would graduate, so this dissertation is in partial fulfillment of that pact.

Thanks to Brent Limyansky, Roy Sfadia, and Dominic Pasquali for doing hours of homework with me and for preventing any boring lunch times. Thanks to Vincent for your support and patience as I keep saying that I'm close to graduating. Thanks especially to Mom, Dad, Michelle, and Ruffy for your continuous love and encouragement.

Introduction

In 1897, J.J. Thomson observed that cathode rays were negatively charged particles in motion.[1] These charged particles, identified as electrons, were the first of many particles to be discovered since then. Modern particle physics has made leaps and bounds in our understanding of particle properties and has resulted in the discovery of many new particles in the last 125 years. Moving from benchtop experiments to large high-energy collider experiments to study particle physics is relatively recent, with large, cutting-edge colliders aiming to create the conditions that might be suitable for the existence of particles yet-to-be discovered on Earth and which previously only existed naturally in the cosmos.

This naturally-existing lab began 13.8 billion years ago with a hot Big Bang–a high-energy, rapid expansion of the matter in the universe that slowly cooled over time to a less dense state we know it as today, but which is still expanding.[2] Several observations of the universe reveal, though, that there is more matter in the universe than we can see– Doppler shifts of stars in a galaxy are used to calculate the rotational velocity of the astronomical bodies as a function of radius from the galaxy's center. In these rotation curve plots, it is evident that the rotational velocity is faster than expected, so the

amount of matter needed to gravitationally interact with the astronomical bodies in the galaxy must be in excess of what we can see. The types of matter we do know about in all the stars and galaxies only account for 5% of the universe. Dark matter makes up about 27% of the universe, and is not luminous enough to be detected by current technology in astronomy.[2]

Modern high-energy particle physics aims to answer the same questions about the origins of matter in the universe from the Big Bang–What is Dark Matter? Why is there more matter than anti-matter? Why are there asymmetries in the universe that we observe today? Why do particles have different masses? What particles are out there that are yet to be discovered?

At the low energy levels we experience in everyday life, we cannot observe many types of particles that existed immediately after the Big Bang. We also observe that matter dominates over anti-matter. Particle accelerators aim to simulate on the high-energy conditions that existed at the Big Bang in order to observe from Earth what types of particles existed at the beginning of the universe and how asymmetries originated.

Fermilab, the SLAC National Accelerator Laboratory, and the European Organization for Nuclear Research (CERN) have all been pivotal high energy physics laboratories in the search for new particles (or rather, particles that existed during the Big Bang but which are new to us in this state of the universe). Although numerous particles have been discovered in Nobel prize-winning experiments at these labs, the identity of dark matter and causes of asymmetries observed remain mysteries that

physicists are still trying to learn more about. Much is still unknown about the Higgs boson, discovered in 2012, but which is a particle with couplings to other particles that could tell us a lot about the origins of matter.

In this dissertation, I will describe the research I worked on at the world's largest particle physics laboratory CERN. Part I describes theory motivations, the Standard Model, and how the Higgs boson fits into that. Part II describes the Large Hadron Collider (LHC) and ATLAS (A Toroidal LHC ApparatuS) detector at CERN. Part III describes the research I conducted at CERN as part of an effort to piece together our understanding of the Higgs boson, specifically on a search for Higgs bosons produced through vector boson fusion and decaying to a pair of b-quarks with an associated photon using the full Run 2 dataset.

Part I

The Standard Model and Higgs Boson Theory

Chapter 1

The Standard Model

The Standard Model (SM) of particle physics is the theory describing all known elementary particles and their interactions through four fundamental forces–the electromagnetic, weak, strong, and gravitational forces. Similarly to how the periodic table in chemistry organizes elements by atomic number properties, the SM organizes particles by their properties including charge, spin, isospin, and mass. Charges and spins are identical for fermions in each row in the Standard Model shown in Figure 1.1, but masses vary. The reasons for each particle's specific mass are mysteries still to be understood.

The SM began from experimental observations, and it has been the basis on which predictions of the existence of new types of particles are made. At present, it includes quarks, leptons, and gauge bosons, as well as the recently-discovered Higgs boson, as shown in Figure 1.1. However, there are many mysteries that the Standard Model does not explain, such as the hierarchy of masses, the hierarchy problem (issue

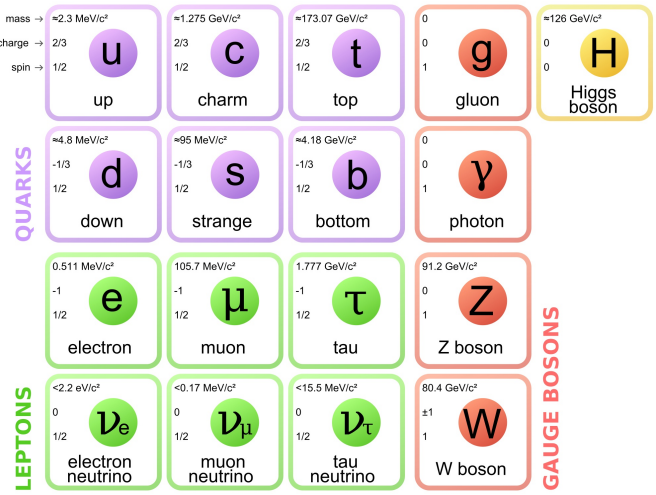

Figure 1.1: The Standard Model of Particle Physics is organized by the particles' properties, and includes quarks, leptons, gauge bosons, and the scalar Higgs boson.[3–6]

that the Higgs mass quantum correction is much larger than the Higgs mass itself), dark matter, dark energy, and the domination of matter over anti-matter.[7]

1.1 Fundamental Particles

1.1.1 Fermions

Fermions were named by Paul Dirac in 1945 after the physicist Enrico Fermi, who built the statistical theories describing these half-integer spin particles that follow the Pauli exclusion principle forbidding them from simultaneously occupying the same quantum space as another particle.[8] Fermions include quarks and leptons.

There are six quarks that all have spin $\frac{1}{2}$ and interact through the strong force: up (u), down (d), charm (c), strange (s), top (t), and bottom (b), as well as their antiparticles. The u, c, and t-quarks all have electric charge $\frac{2}{3}$, while d, s, and b-quarks

all have charge -$\frac{1}{3}$. The u, d, and s-quarks were theorized independently by Murray Gell-Mann and George Zweig in 1964 to explain strong interaction symmetry.[4, 5] The first experimental evidence of them came shortly after that in 1968, when electron-proton scattering experiments at Stanford Linear Accelerator Center (SLAC) indicated that the protons contained point-like particles inside of them.[9]

There are six leptons with spin $\frac{1}{2}$– e^-, μ^-, τ^-, ν_e, ν_μ, and ν_τ–as well as their antiparticles. The e^-, μ^-, τ^- all have -1 electric charge, while the neutrinos are all electrically neutral. Leptons are the lightest group of known particles, so it is fitting that the name comes from the Greek word for "light and small." They are stable and do not decay into any lighter particles. Since leptons have no color charge, they participate in Electromagnetic and Weak Force interactions but do not participate in Strong Force interactions.

Baryons are made up of three quarks and come from the word "heavy" in Greek since they were heavier than the particles known at the time they were discovered. Protons and neutrons are examples of baryons.

1.1.2 Bosons

Bosons, named by Paul Dirac in 1945 after the physicist Satyendra Nath Bose who developed the theories describing the fundamental behavior of such particles, are particles with integer spin.[10] Unlike fermions, they do not follow the Pauli exclusion principle and can occupy the same state and space as another particle simultaneously. They include mesons and force carrier particles known as gauge bosons.

Mesons are made up of a quark-antiquark pair, so they are sensitive to the Strong Force. Their namesake comes from the word "middle" in Ancient Greek because they are lighter than baryons but heavier than leptons. Mesons were theorized by Hideki Yukawa in 1935 as an exchange particle holding protons and neutrons in an atomic nucleus.[11] The first mesons were discovered experimentally in 1947 by Cecil F. Powell and Giuseppe P. S. Occhialini in cosmic radiation showers.[12]

W and Z bosons are intermediate vector bosons, the force carriers in Weak Force interactions. The "weak" interaction is thought to be the inspiration for the nomenclature $W^{\pm}$ boson. The Z boson is thought to be named so for its "zero" or neutral charge, in contrast to the $W^{\pm}$ boson which carries a charge. Both particles were discovered at CERN in 1983.[13–15]

The massless photon is described as a quantum of light and is the force carrier particle for electromagnetic interactions. Its namesake comes from the Greek word for light, "phos."

The Higgs boson (H) is the last known force carrier particle, and it is the only fundamental scalar in the SM. Although many physicists contributed to its theories, including Robert Brout, François Englert, Philip Anderson, Gerald Guralnik, Carl Hagan, Tom Kibble, and Gerard t'Hooft, it was shortened by other physicists who simply called it the "Higgs."[6, 16–19] Without the Higgs boson, we would have a hard time explaining the mass of every other particle in the SM. This will be further explained in Section 1.5.

1.2 Fundamental Forces

The electromagnetic, weak, and strong forces are the fundamental forces of interest in particle physics, which govern fermion and boson interactions. A fourth force, the gravitational force, is many orders of magnitude weaker than the other three forces for particles, so it is not discussed in this dissertation.

1.2.1 The Strong Force

Appropriately named, the strongest fundamental force is the strong force. The strong force's strength compared to the other fundamental forces is described by the strong coupling constant α_S, which is orders of magnitude stronger than the electromagnetic force denoted by the fine structure coupling constant, $\alpha \approx 1/137$.[20] The strong force is 10^6 times stronger than the weak force at QCD scale. However, its range limits it to holding together protons and neutrons in a medium-sized nucleus. At this short range, the strong force overcomes the electromagnetic force of protons that classically would have been expected to repel each other. One of eight types of gluons are exchanged during strong force interactions. Since gluons carry a charge known as color, or the force holding quarks together that make up protons and neutrons, they can couple to other gluons unlike photons which cannot self-couple.[21]

The three types of color charges are in the $SU(3)$ color group, as well as the corresponding anti-color charges. To describe the three distinct quantum states the arbitrary names red, green, and blue are used.[22] The quark color charge must change

when a gluon carries a color charge as it is emitted or absorbed, a process which occurs frequently in hadrons. As a result, the quark color rotates in $SU(3)$ space in order to conserve overall color charge.[22] Hence, these strong force interactions between quarks and gluons are described by the theory of quantum chromodynamics (QCD).

1.2.2 The Electromagnetic Force

The electromagnetic theory describes the classical interactions between electric charges and magnets in the theory of electrodynamics, and has been a cornerstone of classical physics since Maxwell pioneered it more than 100 years ago.[23] In the 1940s, Sin-Itiro Tomonaga, Richard Feynman, and Julian Schwinger adapted the theory for quantum electrodynamics (QED).[24–26] QED interactions are mediated by the exchange of a neutral massless photon that is either emitted or absorbed, thereby causing an electromagnetically-induced momentum transfer between charged particles. Unlike the strong and weak forces which have strengths that fall off with distance at magnitudes equal to or smaller than an atom's nucleus, the electromagnetic force has an infinite range that falls off with the inverse square as a function of distance, and is large enough to dominate as the force that holds atoms and molecules together.

1.2.3 The Weak Force

The weak force describes the interactions between leptons and quarks, and is responsible for changing quark flavor when mediated by the W or Z intermediate vector bosons, which are emitted in a decay process.[27] As noted by its name, it is significantly

weaker than the other two previously mentioned fundamental forces, and also has a very short range on the order of 10^{-18} m. Yet, the weak force plays an important role in particle physics decays, as it is a flavor-changing interaction and mediates the force between two quarks or leptons.

Weak force interactions can be charged, involving a $W^{\pm}$ boson, or neutral, involving a Z boson. As a result of their charge, W^{+} and W^{-} bosons are the only force carriers that change a lepton to the corresponding neutrino, or change quark flavor within the same generation.

1.3 Electroweak Unification

It was a mystery why the electromagnetic force is much stronger than the weak force, and why the weak force W and Z boson mediators are so massive (later measured to be 80.385 ± 0.015 GeV and 91.1875 ± 0.0021 GeV, respectively) but the electromagnetic force-mediating photon is massless.[15, 28] Sheldon Glashow, Abdus Salam, and Steven Weinberg proposed unifying the theories of the weak interactions with the electromagnetic interactions in order to understand the disparities between the two forces strengths and mediator masses, the same way Maxwell unified electromagnetism.[29–31] This later became known as the GSW electroweak model. The GSW electroweak model also predicted that a neutral Z boson must exist to mediate weak neutral currents.[29–31]

SM electroweak interactions are based on the gauge group $SU(2)_L \times U(1)_Y$.

To ensure that the Lagrangian is gauge invariant, the covariant derivative is defined as:

$$\partial_\mu \rightarrow D_\mu = \partial_\mu + ig_W \mathbf{T^a} \cdot \mathbf{W}_\mu + ig' \tfrac{Y}{2} B_\mu. \tag{1.1}$$

The $SU(2)_L$ component refers to the weak isospin group with the three gauge bosons $W_\mu^{(1)}$, $W_\mu^{(2)}$, $W_\mu^{(3)}$ and coupling constant g_W. The generators for the doublets are $T^a = \frac{1}{2}\sigma^a$, where σ^a are the Pauli spin matrices. It has been observed experimentally that the charged weak currents only couple with left-handed particles and right-handed antiparticles, but not right-handed particles or left-handed antiparticles–this asymmetry is yet another mystery, and the reason the symmetry group is called $SU(2)_L$.[32]

The $U(1)_Y$ component refers to the weak hypercharge with the gauge boson B_μ and the coupling constant g'. Y is the weak hypercharge, defined as $Y = 2(Q - I_W^{(3)})$, where Q is the electric charge and $I_W^{(3)}$ is the 3rd component of isospin.

The weak charged current corresponds to the $SU(2)_L$ local gauge symmetry, with the W^+, W^-, and neutral gauge field $W^{(3)}$ arising from each of the Pauli spin matrices. The charged weak boson field for the physical W boson is given by the linear combinations of $W^{(1)}$ and $W^{(2)}$:

$$W^\pm = \frac{1}{\sqrt{2}}(W^{(1)} \mp iW^{(2)}) \tag{1.2}$$

The $SU(2)_L$ gauge symmetry also suggests that a neutral current exists. However, this cannot be the neutral Z boson because $I_W^{(3)} = 0$ prevents couplings to right-handed particles and left-handed antiparticles, but it is observed experimentally that the

Z boson couples to both right and left-handed chiral states.[33] Using the weak mixing angle θ_W, linear combinations of the B_μ gauge field and the neutral $W_\mu^{(3)}$ are instead used to describe the photon and Z boson mass eigenstate fields, given by the set of linear equations:

$$A_\mu = B_\mu \cos\theta_W + W_\mu^{(3)} \sin\theta_W \tag{1.3}$$

and

$$Z_\mu = -B_\mu \sin\theta_W + W_\mu^{(3)} \cos\theta_W. \tag{1.4}$$

Experimentally, θ_W is measured in numerous ways with an average value of $\sin^2\theta_W = 0.23150 \pm 0.00006$.[34] Knowing θ_W specifies the properties of the Z boson, supporting the GSW electroweak model that predicted the Z boson would exist. θ_W also shows how the couplings of the photon and weak bosons are related by the electron charge, e:

$$e = g' \cos\theta_W = g_W \sin\theta_W = g_Z \sin\theta_W \cos\theta_W. \tag{1.5}$$

1.4 Spontaneous Symmetry Breaking

In 1918, Emmy Noether published her theorem stating that every symmetry has a conservation law associated with it.[35] Since then, much of physics has consisted of searching for these symmetries and their consequences. Yet, broken symmetries are observed in particle physics, such as the dominance of matter over anti-matter, the disparity in strengths between the weak and EM forces, and particle masses. These

observations of broken symmetries have sent physicists on a hunt to understand how theories relying on fundamental symmetries give rise to physical broken symmetries.

Physicists have understood for some time how local gauge invariance principles are consistent with the strong force and electromagnetic force interactions. In electromagnetism, the physical **B** and **E** are invariant under gauge transformation. Similarly, QED comes from requiring invariance under local $U(1)$ transformations fulfilling

$$\hat{U} = e^{iq\chi(x)}. \tag{1.6}$$

Local gauge invariance principles mean that there must be a gauge field that can couple to Dirac particles and is massless in weak interactions–this is consistent with the properties of the massless photon. However, $U(1)$ local gauge invariance is not consistent with the heavy W and Z boson particles. Including the massive gauge fields would require breaking $U(1)$ local gauge symmetry.

Breaking the SM electroweak $SU(2)_L \times U(1)_Y$ local gauge symmetry gives rise to the Higgs mechanism, which was proposed by Peter Higgs in 1964 theorizing that all elementary particles would have mass by interacting with a "Higgs field."[6] On the order of 10^{-12} seconds after the Big Bang, it is thought that particles interacted with the non-zero Higgs field (vacuum expectation value) as the universe rapidly cooled. Some particles such as the W and Z bosons gained mass from their interaction with the field, while spontaneous symmetry breaking meant that photons remained massless.[6] This field must be scalar–or uniform in all directions–and a stronger interaction with the Higgs

field results in a larger particle mass. This interaction is called the Brout-Englert-Higgs mechanism, named after theoretical physicists Robert Brout, François Englert, and Peter Higgs.[6, 16]

The Lagrangian for a three-dimensional, complex scalar field

$$\phi = \frac{1}{\sqrt{2}}(\phi_1 + i\phi_2) \tag{1.7}$$

is given by

$$\mathcal{L} = \frac{1}{2}(\partial_\mu \phi_1)^*(\partial^\mu \phi_1) - \frac{1}{2}\mu^2(\phi_1^2 + \phi_2^2) - \frac{1}{4}\lambda(\phi_1^2 + \phi_2^2)^2. \tag{1.8}$$

This Goldstone boson Lagrangian is gauge invariant under the rotation $\phi \rightarrow e^{i\alpha}\phi$.[36] The mass parameter μ^2 and and scalar field self-interaction parameter λ are real constants. The first term of Equation 1.7 is the kinetic energy term, and the last two terms (starting from μ^2) are the potential energy terms. Figure 1.2a shows the two-dimensional potential when $\mu^2 > 0$ where there is a single minimum at $\phi = 0$, which corresponds to the vacuum state.[36]

The parameter λ must be greater than zero so that there is a finite minimum, but when $\mu^2 < 0$, the potential is represented by Figure 1.2b.[36] There are an infinite number of minima with non-zero vacuum expectation values satisfying

$$V_{\text{min}} = -\frac{\mu^4}{4\lambda} \tag{1.9}$$

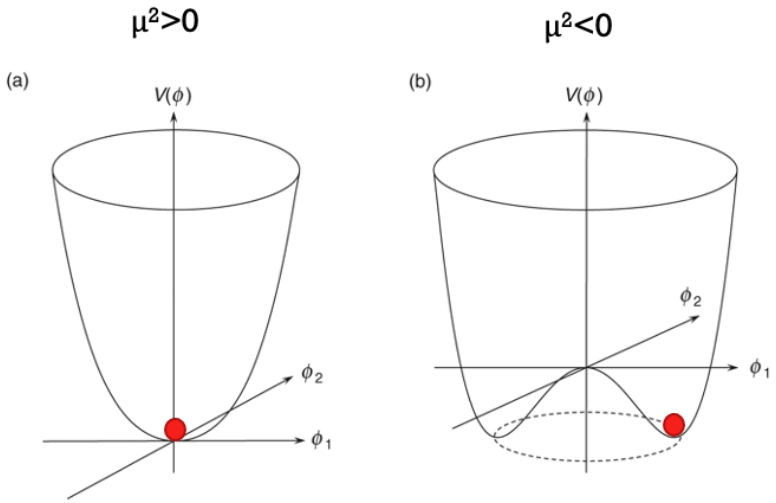

Figure 1.2: The 3 dimensional potential for (a) $\mu^2 > 0$ and (b) $\mu^2 < 0$.

when

$$\phi_1^2 + \phi_2^2 = -\frac{\mu^2}{\lambda} \tag{1.10}$$

at any point on the dotted circle shown in Figure 1.2b.

A physical state must correspond to a particular point lying along that dotted circle, but by picking one of the minima as the physical state, the symmetry of the Lagrangian is broken. Since none of the vacuum state minima should be preferred, spontaneous symmetry breaking has occurred. $U(1)$ symmetry is not broken because it is still invariant under rotations in ϕ_1 and ϕ_2.

1.5 The Higgs Mechanism and Mass Generation

The Higgs Mechanism $SU(2)$ doublet of complex fields can be expressed as

$$\phi = \begin{pmatrix} \phi^+ \\ \\ \phi^0 \end{pmatrix} = \frac{1}{\sqrt{2}} \begin{pmatrix} \phi_1 + i\phi_2 \\ \\ \phi_3 + i\phi_4 \end{pmatrix}. \tag{1.11}$$

The doublet used in the Lagrangian is given by:

$$\mathcal{L} = \frac{1}{2}(\partial_\mu \phi)^\dagger (\partial^\mu \phi) - \mu^2 \phi^\dagger \phi - \lambda(\phi^\dagger \phi)^2. \tag{1.12}$$

Similarly to how the Lagrangian in Equation 1.7 above has degenerate solutions, the Higgs potential in this Lagrangian has an infinite number of degenerate minima when

$$\phi^\dagger \phi = \frac{1}{2}(\phi_1^2 + \phi_2^2 + \phi_3^2 + \phi_4^2) = -\frac{\mu^2}{2\lambda} = \frac{v^2}{2}, \tag{1.13}$$

where v is the vacuum expectation value (VEV).

Considering only the real-valued physical fields, we have

$$\phi = \frac{1}{\sqrt{2}} \begin{pmatrix} 0 \\ \\ v + H(x) \end{pmatrix}, \tag{1.14}$$

which is achieved from expanding about the vacuum state. In order to identify the mass

terms, we can then use the covariant derivative from Equation 1.1 to get:

$$(D_\mu\Phi)\dagger(D^\mu\Phi) = \frac{1}{2}\partial^\mu H\partial_\mu H + \left[\left(\frac{g_W v}{2}\right)^2 W^{\mu+}W^-_\mu + \frac{1}{2}\frac{(g_W^2+g'^2)v^2}{4}Z^\mu Z_\mu\right]\left(1+\frac{H}{v}\right)^2. \tag{1.15}$$

[37]

From this, the W boson and Z boson masses can be picked out from the coefficients, and are given by:

$$m_W^2 = \frac{g_W^2 v^2}{4} \tag{1.16}$$

and

$$m_Z^2 = \frac{(g_W^2+g'^2)v^2}{4}, \tag{1.17}$$

respectively. The Higgs boson is said to "give mass" to the W and Z bosons because of the dependence on the vacuum expectation value v, which is the lowest-energy state of the field ϕ.[38] Experimental measurements give us M_W, Fermi constant calculations give us g, and the relationship from Equation 1.16 above allows us to calculate that $v = 246.22$.[39] The parameter λ can now be calculated since $m_H = \sqrt{2\lambda}v$ and the Higgs mass has been measured experimentally, as will be described in Section 2.1.

Since the Higgs mechanism is required to generate masses of electroweak gauge bosons, one field must be neutral matching ϕ^0 and the other must be charged matching ϕ^+. These fields correspond to the neutral Z boson and charged $W^\pm$ bosons. The mass of the photon is derived from the eigenvectors of the mass matrix shown in Equation 1.3

and is still given by $m_A = 0$.

Thus, the Higgs boson couplings to the gauge boson are proportional to the boson masses, and explain how the W and Z bosons acquire mass without breaking the local gauge symmetry of the SM:

$$g_{HWW} = \frac{1}{2} g_W^2 v = g_W m_W \tag{1.18}$$

and

$$g_{HZZ} = g_Z m_Z. \tag{1.19}$$

The Higgs mechanism also gives mass to the fundamental down-type fermions:

$$\mathcal{L}_e = -\frac{g_e}{\sqrt{2}} v(e_L e_R + e_R e_L) - \frac{g_e}{\sqrt{2}} h(e_L e_R + e_R e_L), \tag{1.20}$$

where $m_e = \frac{g_e}{\sqrt{2}} v$ is the mass of the electron. The fields can only generate masses for the fermion in the lower component of the $SU(2)$ doublet in this case, but a similar process can be performed for up-type quarks. Because only one Higgs boson is needed for all of the masses as was just described, it is commonly said that the Higgs boson "gives mass" to particles.

1.6 Higgs Boson Theory

The landmark discovery of the Higgs boson was announced by the ATLAS and Compact Muon Solenoid (CMS) Collaborations in 2012. More on the discovery will be

described in Section 2.1. While a lot has been learned about the Higgs boson since then, many properties of this long-sought-after particle are still unknown. The interest has been on understanding the Higgs boson mass and couplings–in particular, analyses have focused on measuring the Higgs boson coupling strengths to other particles, production rates, and decay branching ratios to make comparisons with Standard Model predictions. Deviations from the SM predictions would give hints about Beyond the Standard Model (BSM) physics.

1.6.1 Higgs Boson Branching Ratios

The Higgs boson lifetime is only 1.6×10^{-22} seconds, which results in a decay length too short to be measured in the detector before it decays to other particles.[40] When measuring the Higgs boson, measurements are actually being taken of the final state particles that the Higgs boson quickly decayed to. The partial decay width of the Higgs boson for fermions is given by:

$$\Gamma(H \to X\bar{X}) = 3\frac{m_X^2 m_H}{8\pi v^2}, \tag{1.21}$$

where "X" is a decay product of the Higgs. The Higgs boson decays most frequently (57% of the time) to a pair of b-quarks as shown in Figure 1.3.[41] With a mass of about 4.2 GeV, b-quarks are the most massive fermions that the Higgs boson, with a measured mass of about 125 GeV, can decay to.[42] The b-quark lifetime of about 1.5 ps ($\langle c\tau \rangle \approx 450\mu$m) means that it travels a few millimeters from its production vertex in

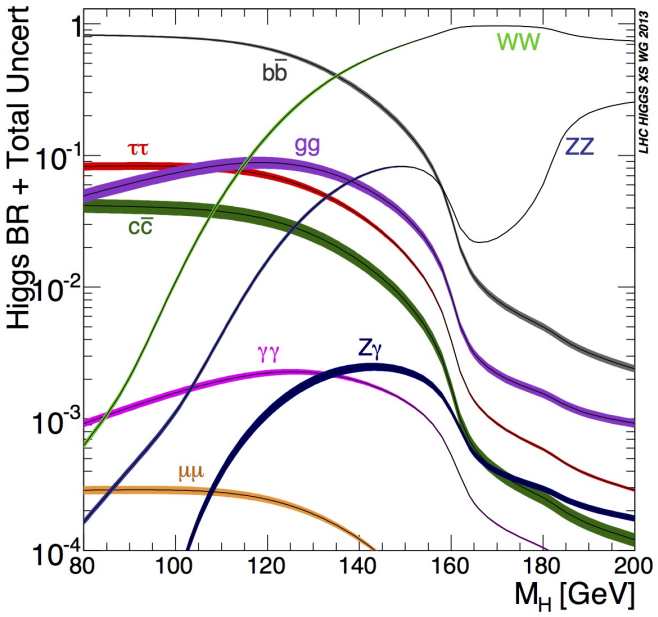

Figure 1.3: SM Higgs boson decay branching ratios as a function of Higgs boson mass. With a Higgs boson mass of 125 GeV, the Higgs most frequently decays to a pair of b-quarks.[44]

the detector before decaying, making it much easier to measure than the Higgs boson.

Other common Higgs branching fractions are shown in Table 1.1. Although the Higgs boson most frequently decays to b-quarks, $H \to \gamma\gamma$ and $H \to ZZ \to 4l$ were the first observed evidence of the Higgs boson because photons and leptons leave clearer experimental signatures in the ATLAS and CMS detectors and less background contamination, making it easier to pick out the Higgs bosons.[43]

1.6.2 Higgs Boson Production

The four largest cross section production modes of the Higgs boson are shown in Figure 1.4. Starting with the largest cross section, they are Gluon-Gluon Fusion (ggF),

Decay Mode	Branching Ratio
$H \to b\bar{b}$	57.8%
$H \to WW^*$	21.6%
$H \to gg$	8.6%
$H \to \tau^+\tau^-$	6.4%
$H \to c\bar{c}$	2.9%
$H \to ZZ^*$	2.7%
$H \to \gamma\gamma$	0.2%

Table 1.1: Predicted branching ratios of the SM Higgs boson for $m_H = 125$ GeV, in order from most to least frequent.[41]

Vector Boson Fusion (VBF), Vector-associated Higgs production (VH), and associated production of a Higgs boson and a top quark-antiquark pair ($t\bar{t}H$).

In the gluon-gluon fusion processes, one gluon from each of the colliding LHC protons fuses through a t-quark loop to produce a Higgs boson. It is the most frequent process because of α_S couplings and the gluon parton distribution function (PDF) requirements in producing a Higgs boson. Vector boson fusion occurs when two incoming quarks from each of the colliding LHC protons radiates either a W boson or Z boson. The pair of W bosons or Z bosons then fuses to produce a Higgs boson, and the initial quarks are deflected from their initial paths. Vector-associated Higgs production occurs when a Higgs boson is produced in association with a W boson or Z boson. Associated production of a Higgs and top quark-antiquark pair occurs when a $t\bar{t}$ pair fuses to produce a Higgs boson, or when a Higgs boson radiates off of a t-quark.

The production cross section of ggF is more than 10 times larger than that of the second-largest cross section VBF, and the VBF cross section is about three times larger than the VH cross section as shown in Figure 1.6.[45] However, ggF and VBF

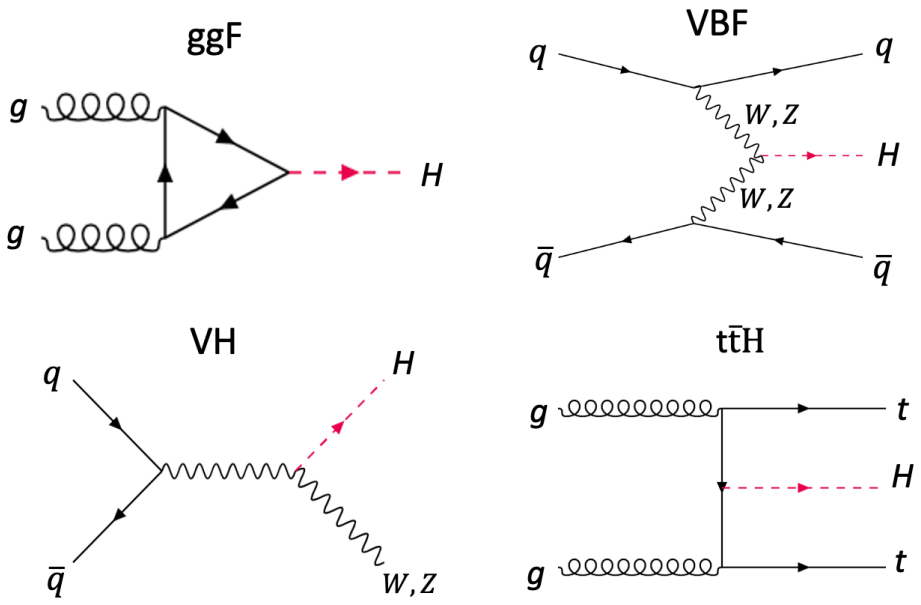

Figure 1.4: The four main Higgs boson production modes. Top: Gluon-gluon fusion (ggF) and vector boson fusion (VBF) processes. Bottom: Vector-associated Higgs (VH) production and associated production of a Higgs boson with a top quark-antiquark pair ($t\bar{t}H$).

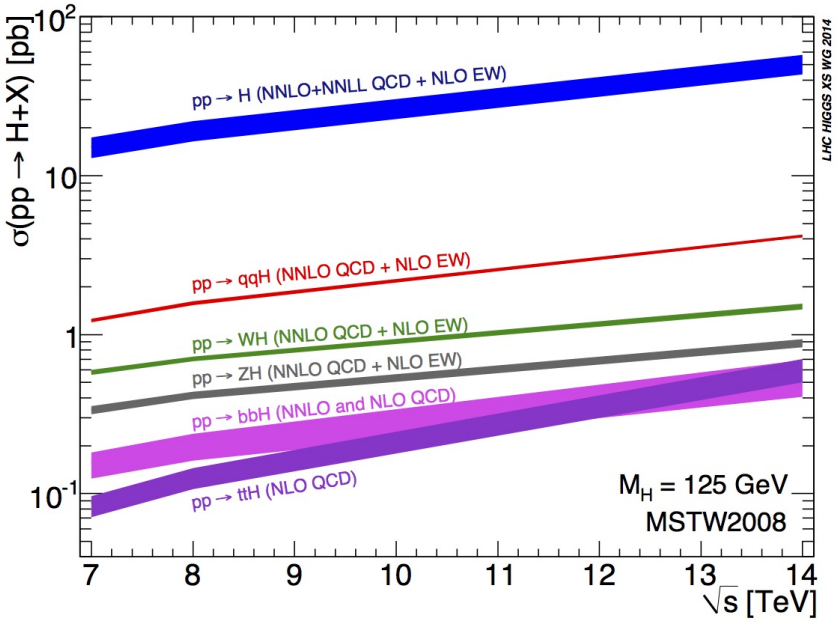

Figure 1.5: SM Higgs Production Modes: ggF production is $pp \to H$ and is shown in blue. It is the dominant production mode, and is about 10 times more common than the VBF process $pp \to qqH$, shown in red.[44]

analyses suffer from high levels of background QCD radiation, making it difficult to distinguish clean signal events from the background. VH analyses, on the other hand, have taken advantage of measuring the cleaner leptonic final states which makes it easier to suppress QCD background. For this reason, the most sensitive measurements of Higgs bosons decaying to a pair of b-quarks are from the VH production mode.[46]

The Higgs boson can also be produced in association with a photon. VBF becomes the leading production cross section when a high-energy photon requirement is added–its cross section is about six times larger than that of ggF at $\sqrt{s} = 13$ TeV.[45] This production mode will be the main focus of this thesis, and will be described more in Section 2.3 and Chapter III.

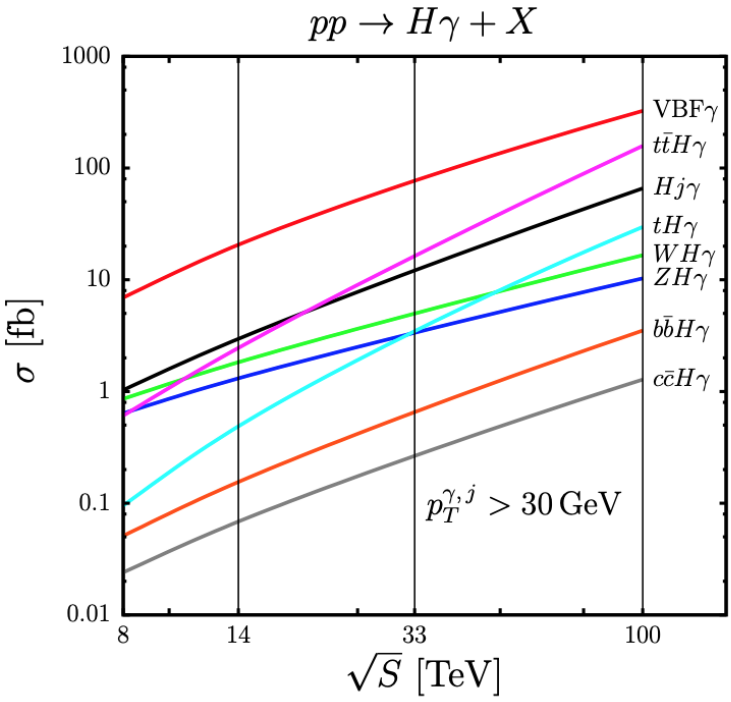

Figure 1.6: SM Higgs plus photon Production Modes: The additional photon requirement in the final state makes VBF the dominant production mode, as shown by the red line.[45]

Chapter 2

Higgs Bosons at the Large Hadron Collider

2.1 Higgs Boson Discovery

Numerous experiments at the Large Electron-Positron (LEP) Collider, the Tevatron, and LHC searched for the Higgs boson for four decades, only limiting the Higgs boson mass to be in a mass region above 600 GeV or in a window from 116 GeV to 127 GeV at 95% confidence-level.[43]

On July 4, 2012, the ATLAS and CMS Collaborations jointly announced the discovery of a new particle with the properties of a neutral boson: the long searched for Higgs boson. The Higgs boson was observed from analyzing decays of $H \to ZZ^{(*)} \to 4l$, $H \to \gamma\gamma$, and $H \to WW^{(*)} \to l\nu l\nu$ at an energy of $\sqrt{8}$ TeV. The highest mass resolution came from the $H \to ZZ^{(*)} \to 4l$ and $H \to \gamma\gamma$ channels, while $H \to WW^{(*)} \to l\nu l\nu$

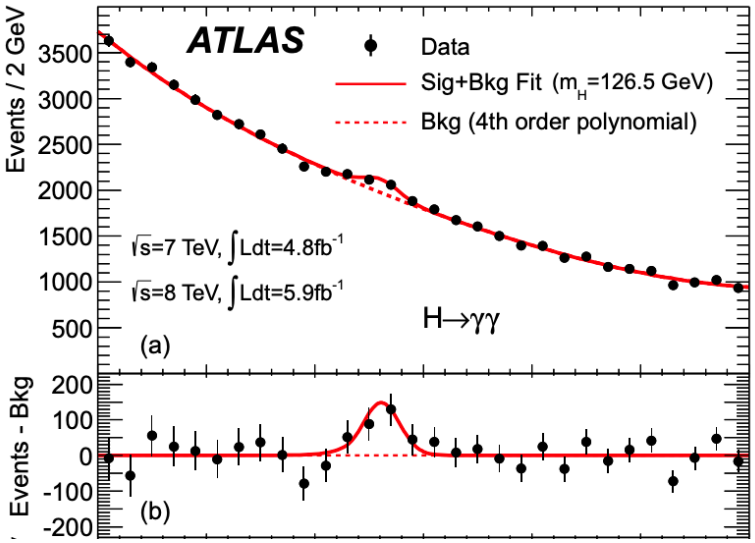

Figure 2.1: The 2012 ATLAS Higgs boson discovery plot shows the invariant mass from the decay of $H \to \gamma\gamma$ for the combined 7 TeV and 8 TeV data samples. Plot A shows the inclusive sample without weighting, while plot B shows the residuals.[43]

had lower resolution but good sensitivity from measuring the leptons and neutrinos in the final state.[43] In combining those channels, ATLAS observed an excess of events above expected background at 126.0 ± 0.4 (statistical) ± 0.4 (systematic) GeV with a significance of 5.9σ.[43] This corresponded to a signal strength $\mu = 1.4 \pm 0.3$, where μ is the ratio of the measured cross section over the SM-predicted cross section.

CMS similarly observed an excess of events above expected background levels primarily from the $H \to ZZ^{(*)} \to 4l$ and $H \to \gamma\gamma$ decay modes.[43, 47] The diphoton plot showing an excess at 125.3 GeV is shown if Figure 2.2. CMS measured a mass of 125.3 ± 0.4 (statistical) ± 0.5 (systematic) and a significance of 5.0σ, also indicating the existence of the Higgs boson.[43] Since this new Higgs boson particle was observed to decay into a pair of photons, its spin had to be a value other than one to conserve

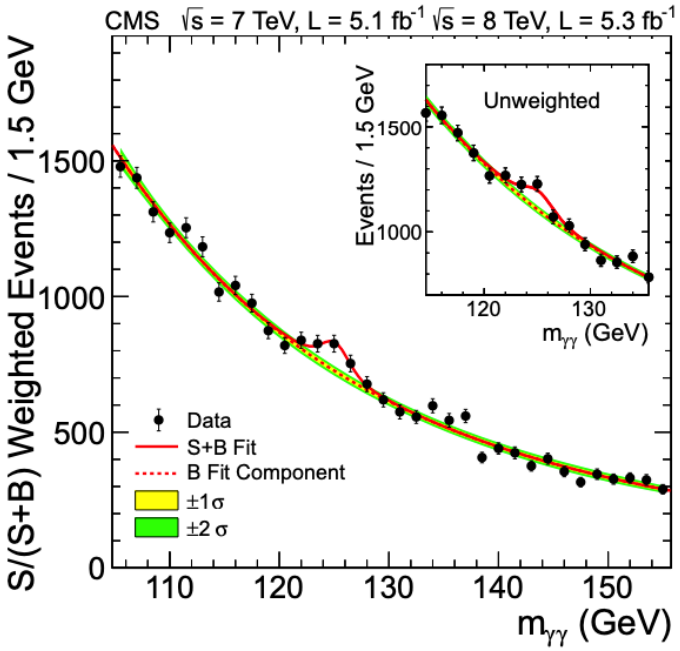

Figure 2.2: The 2012 CMS discovery plot for the Higgs to diphoton channel.[47]

angular mometum.

Experimental confirmation of this fundamental particle was so noteworthy that François Englert and Peter Higgs were awarded the 2013 Nobel Prize in Physics "for the theoretical discovery of a mechanism that contributes to our understanding of the origin of mass of subatomic particles, and which recently was confirmed through the discovery of the predicted fundamental particle, by the ATLAS and CMS experiments at CERN's Large Hadron Collider."[48]

2.2 Current Experimental Status

In the 10 years since the discovery of the Higgs boson, many of the SM theories have been verified experimentally. Most of the results of Run 1 were reported in terms of the signal strength μ. Production cross sections σ describe the Higgs production modes based on the assumptions of SM branching ratios. On the other hand, branching ratios B describe the Higgs decay modes with the assumptions of SM production cross sections. Cross section times branching fraction ($\sigma \times B$) measurements allow for fewer assumptions about the SM values.

The four main Higgs production mechanisms have been observed to be consistent with the Standard Model predictions, as shown in Figure 2.3. These production cross sections describe the Higgs boson production modes and assume Standard Model branching ratios. They are measured with a simultaneous fit to data in the region $|y_H| < 2.5$, and result in a $p_{SM} = 63\%$ compatibility between measurements and the Standard Model.[49]

One problem with measurements expressed in terms of σ and B is that they have SM theory dependencies, which arise from assuming either a SM production rate or branching ratio when measuring the other parameter. The solution is to separate the measurement and interpretation steps to avoid the theory dependencies. This is done by dividing the Higgs boson phase space into non-overlapping regions based on the Higgs production mode properties, known as Simplified Template Cross Sections (STXS), as shown in Figure 2.4.[49] Each of the main Higgs production modes is separated into

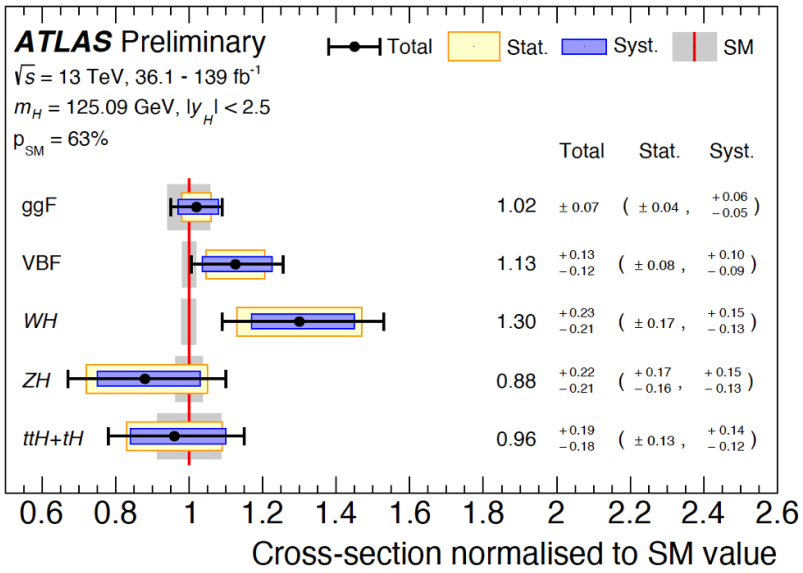

Figure 2.3: The cross sections for SM Higgs boson production modes ggF, VBF, WH, ZH, and $t\bar{t}H+tH$, normalized to the SM predictions. SM values for the decay branching fractions were assumed, and theory uncertainties on the SM cross section values are represented by the gray boxes. Total uncertainty is represented by the black bars, while statistical and systematic uncertainties are represented by the yellow and purple boxes, respectively.[49]

categories based on the number of jets, Higgs boson transverse momentum, and invariant mass of the jets. This separation reduces the theory uncertainties, and is useful for re-interpreting results, deriving cross section upper limits, and constraining anomalous couplings in Standard Model Effective Field Theory (SMEFT).[49]

Numerous Higgs boson decay modes ($\gamma\gamma$, ZZ^*, WW^*, $\tau\tau$, $b\bar{b}$, and $Z\gamma$) have been observed at the LHC to be consistent with Standard Model predictions. Analyses combining multiple Higgs production and decay modes have provided the opportunity to probe the Higgs boson at unprecedented levels of precision, as shown in Figure 2.5. The Higgs combination analysis reports $p_{SM} = 79\%$ compatibility between measurements and the Standard Model for measurements of $\sigma \times B$ normalized to SM as shown in Figure 2.5.[49]

The $H \to \gamma\gamma$ analysis remains the gold standard as one of the most sensitive channels from the Higgs discovery analysis. Despite the small branching ratio, the photon provides a clean final state measurement.[50]

The $H \to \tau\tau$ analysis includes leptonic $\tau \to l\nu_l\nu_\tau$ and hadronic $\tau \to$ hadrons $+\nu_\tau$ decays. It has the largest branching ratio of Higgs bosons decaying to leptons, and provides an opportunity to study the Yukawa mechanism.[51]

The All-Hadronic Boosted $H(b\bar{b})$ analysis was the first to study the Higgs produced with a transverse momentum greater than 1 TeV. At low Higgs boson momenta, the ggF production mode dominates Higgs production, but in this higher momentum range the VH cross section is about the same as the ggF cross section, and the VBF and $t\bar{t}H$ cross sections make substantial contributions. In this boosted domain, there is

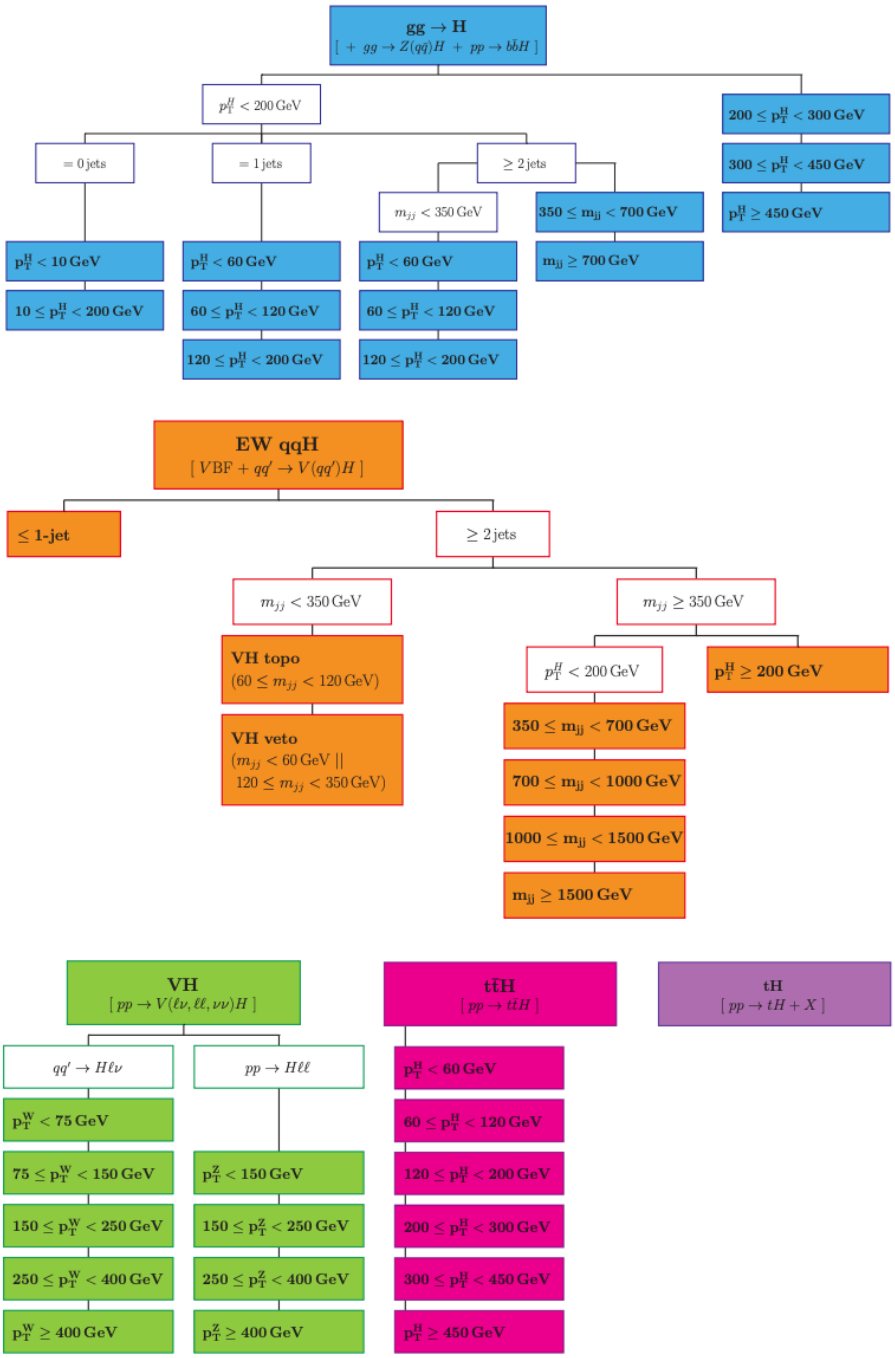

Figure 2.4: STXS 2.1 categorizations for the main Higgs boson production modes. Categories are separated into five Higgs production modes: $gg \to H$ (blue), EW qqH (orange), VH (green), $t\bar{t}H$ (pink) and tH (purple). Within each production mode, bins are separated by intermediate criteria represented by the unfilled boxes, or by final selection criteria in the colored boxes based on the number of jets, p_T of the Higgs, W, or Z boson, and m_{JJ}.[49]

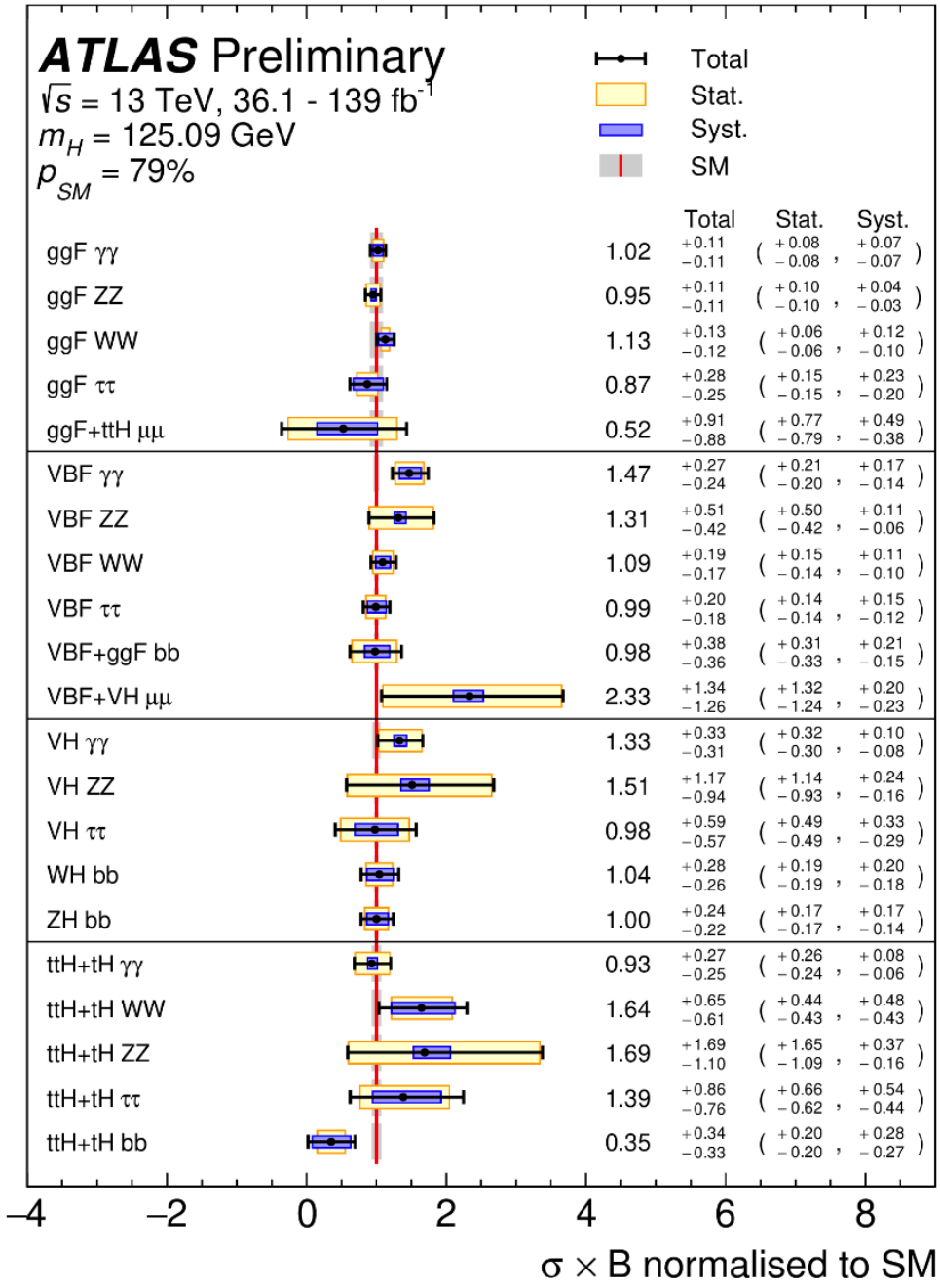

Figure 2.5: Cross section times branching ratio measurements for the four main production mechanisms in various Higgs boson decay modes.[49]

also an improved signal-to-background ratio and enhancement of potential Beyond the Standard Model (BSM) effects.[52]

Additional analyses are closing in on the rarer Higgs decays to $\mu\mu$ and $c\bar{c}$. Despite the fact that 5σ results have not yet been reached for these analyses, they still provide interesting results and additional clues about the Higgs boson. The $H \to \mu\mu$ analysis measures the four main production modes, and provides the best opportunity to measure Higgs interactions with second-generation fermions.[53]

The $H \to c\bar{c}$ analysis targets $ZH \to \nu\nu c\bar{c}$, $WH \to l\nu c\bar{c}$, and $ZH \to llc\bar{c}$.[54] When combining with the $VH(b\bar{b})$ results, the ratio of the Yukawa coupling modifiers for c-quarks and b-quarks is constrained as $|\kappa_c/\kappa_b| < 4.5$.[54] This is smaller than the ratio of $m_b/m_c = 4.578$, implying that the c-coupling to the Higgs boson is weaker than that of the b-coupling.[54, 55]

Although the limits on the c-coupling are still being constrained, the coupling strengths of a number of other particles to the Higgs boson have been measured, as shown in Figure 2.6. This plot has been updated with results from the 10 years since the Higgs discovery, and even more clearly demonstrates that the coupling strength to the Higgs boson is proportional to the particle mass, as predicted by the Brout-Englert-Higgs mechanism.

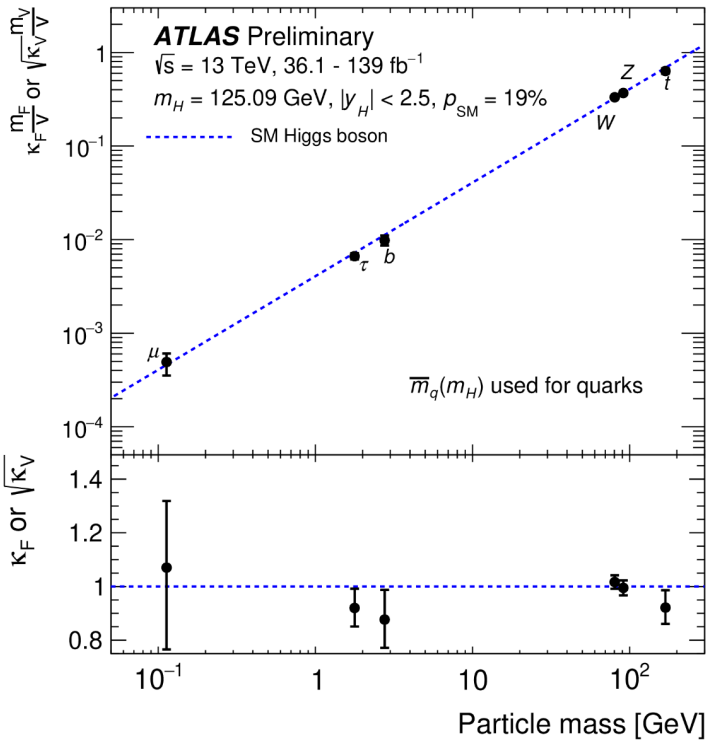

Figure 2.6: The plot of Higgs boson coupling strength shown as a function of particle mass indicates that heavier particles are more strongly coupled to the Higgs boson. There is more to learn about the μ and b-couplings, which have the largest uncertainties.[49]

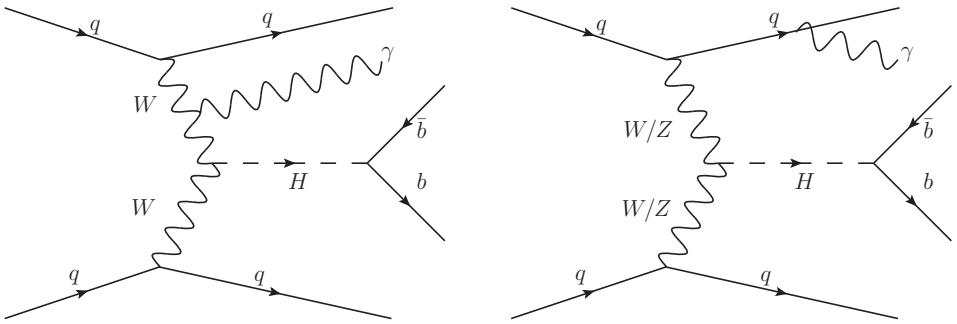

Figure 2.7: Signal Feynman diagrams for VBF $H(b\bar{b}) + \gamma$ production. A photon can radiate off one of the fusing W bosons (left), or off of an initial or final state quark (right), leaving a final state with two VBF jets, 2 b-jets, and a photon.[56]

2.3 Higgs Boson Production via Vector Boson Fusion in Association with a High-Energy Photon

One production mode that has yet to be observed is the H+γ final state. Requiring a Higgs boson plus a photon in the final state changes the hierarchical order, so that VBF becomes the leading production cross section.[45] Therefore, for studying the $H(\rightarrow b\bar{b}) + \gamma$ final state shown in Figure 2.7, the VBF production mode of the Higgs boson is particularly powerful because a clean experimental signature is achieved from triggering on a high-energy photon. The $H \rightarrow b\bar{b}$ process is of particular interest to take advantage of the high branching ratio of Higgs bosons decaying to b-quarks to compensate for the small $H + \gamma$ cross section.

This VBF Higgs boson production mode with a photon also provides a clean measurement of WW fusion due to destructive interference between diagrams with the photon radiating from the incoming quark and those with the photon radiating from the outgoing quark, which must be the case when two Z bosons fuse.[45] This destructive

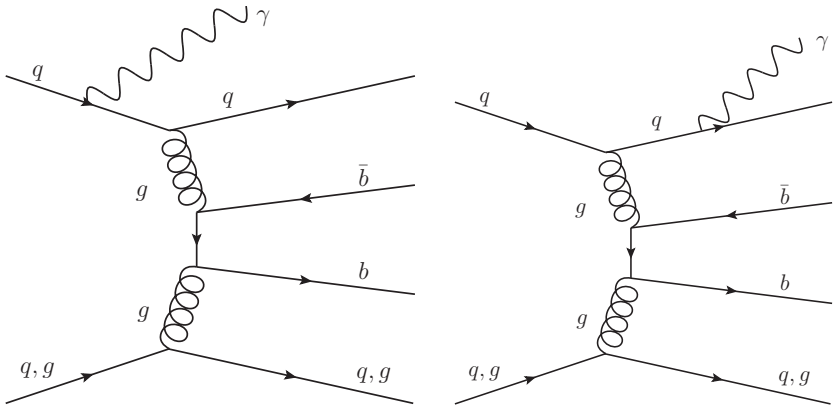

Figure 2.8: Background $b\bar{b}\gamma jj$ QCD Feynman diagrams. This QCD process leaves jets, two b-jets, and a photon in the final state.[56]

interference suppresses ZZ fusion, leaving primarily WW fusion since the photon can also radiate off of the fusing W bosons, as shown in the lefthand Feynman diagram of Figure 2.7. Although the case with photons radiating off of a b-jet would result in the same final state, this diagram is excluded for reasons described in Appendix D.

Lastly, the Higgs boson plus photon requirement is beneficial because destructive interference occurs for non-resonant QCD $b\bar{b}\gamma jj$ between diagrams with the photon radiating off of the incoming quark and those with the photon radiating off of the outgoing quark. This destructive interference greatly reduces this dominant QCD background shown in Figure 2.8.[45] The background is suppressed more than the signal, due to the diagrams where the photon radiates off of the fusing W bosons for the signal but not for the QCD background.

Although low statistics make this VBF $H + \gamma$ production challenging to study, it is the best opportunity to measure $H + \gamma$. The diboson production inherent in VBF is a good test of electroweak physics, and the advantages of this process mentioned above

make a promising and interesting search. The analysis section of this dissertation will focus on the search for vector boson fusion production of a Higgs boson decaying to a pair of b-quarks in association with a high-energy photon. The Full Run 2 dataset at $\sqrt{s} = 13$ TeV is used in this analysis. It was collected from the ATLAS detector at the Large Hadron Collider, which will be described in detail in the following chapters.

Part II

The ATLAS Detector at the Large Hadron Collider

Chapter 3

The Large Hadron Collider

To search for the Higgs boson, the world's largest accelerator and detectors were built at the Large Hadron Collider at the European Organization for Nuclear Research (CERN) on the Franco-Swiss border near Geneva, Switzerland. It has been a long journey though– starting in the early 1980s, scientists began conceptualizing the LHC and its experiments that might find the Higgs. The CERN Council approved it in 1994, and construction began in 2001.[57] The LHC was built at the site of the former Large Electron-Positron (LEP) Collider at CERN, primarily because upgrading a pre-existing tunnel with a new accelerator greatly reduced costs compared to building a completely new facility.

The main goal at the time was to discover the Higgs boson, which was predicted by the Standard Model but had not yet been observed experimentally.[43] To do so required achieving record-breaking energies that could produce a Higgs in the mass range 110-600 GeV, and even higher energies to discover heavier particles.[58]

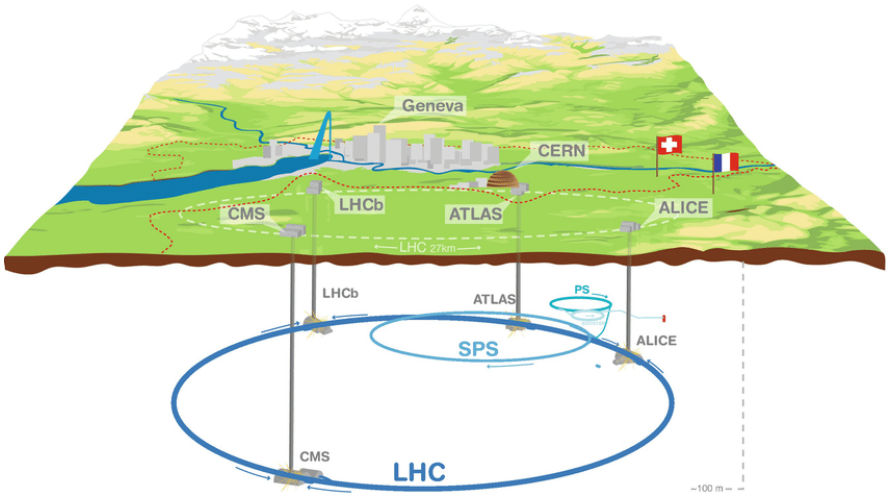

Figure 3.1: The LHC and 4 main experiments at CERN, shown below the Franco-Swiss border. The PS (Proton Synchrotron) and SPS (Super Proton Synchrotron) increase the beam energy before entering the LHC rings.[59]

Two beams of protons circulate in opposite directions 100 meters underground in a 27-km circumference ring, at up to 99.9999991% the speed of light. 8.33 T superconducting dipole magnets bend the beams through the ring, and quadrupole magnets focus the beam.[60] The design energy of the LHC is 14 TeV. The high energy is advantageous for colliding more high-energy protons that have a chance to produce a Higgs boson, but is limited by the strength of the magnets accelerating particles through the 27-km circumference ring. There are four main experiments conducted at CERN: ATLAS, CMS, LHCb, and ALICE. They are shown on the map in Figure 3.1. At each experiment's detector, the counter-circulating beams collide and particle interactions are measured by the detectors.

The center-of-mass energy, or energy in the proton-proton beam center-of-mass reference frame, is used to describe the LHC energy and is denoted as $\sqrt{s}$. During Run

2, each beam operated at an energy of 6.5 TeV, resulting in a total collision energy of $\sqrt{s} = 13$ TeV.

The Large Hadron Collider injected its first beams in September 2008, but faced electrical issues with the superconducting magnets, limiting operations to 7 TeV instead of the originally planned 13 TeV.[61] The LHC restarted in 2010 after a shutdown, and an integrated luminosity of 4.6-4.8 fb^{-1} was collected in 2011 and another 5.8-5.9 fb^{-1} was collected in 2012.[43]

Luminosity L is the ratio of the number of events detected (N) in a certain time (t) to the interaction cross-section (σ), and is given by $L = \frac{1}{\sigma}\frac{dN}{dt}$. Integrating over time gives the integrated luminosity $L_{\text{int}} = \int L dt$. The peak luminosity increased gradually during Run 2 through late 2017, until reaching a relatively consistent peak luminosity around 2×10^{34} cm^{-2}s^{-1} during 2018 as shown in Figure 3.2. The total integrated luminosity increased during each year of Run 2 as well, totaling 160 fb^{-1} (although not all of it was usable for physics analysis) as shown in Figure 3.3.

Run 2 of the LHC operated at $\sqrt{s} = 13$ TeV, which is slightly lower than the design maximum of $\sqrt{s} = 14$ TeV. Operations at slightly lower collision energy have been a result of limitations on the 1232 superconducting dipole magnets that bend and steer the beam through the 27 km ring. A higher magnetic field is needed to operate at higher beam energies, which requires a higher electric current through the magnets' superconducting coils. However, this increases the probability of a magnet quench, during which a magnet loses its superconducting properties. To minimize quenches, superconducting magnets are trained by slowly increasing the current. Running at

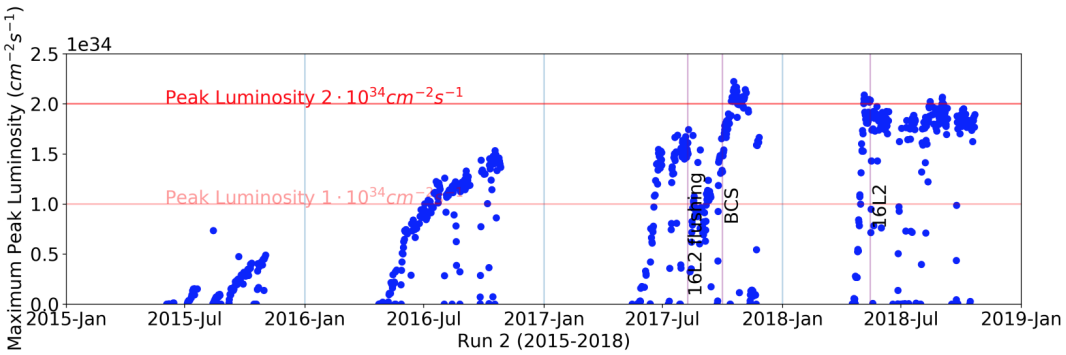

Figure 3.2: Peak luminosity increased over the first three years of Run 2 before leveling out in 2018.[63]

lower collision energies required less time for training, allowing earlier production of physics-quality beams.[62]

Run 3 is planned to operate at $\sqrt{s} = 13.6$ TeV. Since discovering the Higgs boson in 2012, the ATLAS and CMS experiments have been focusing on understanding the Higgs boson production modes, decay mechanisms, and couplings to other particles. Anything that is inconsistent with the SM would provide clues possibly related to dark matter, dark energy, and other beyond-the-Standard-Model (BSM) physics.

3.1 Injection System

Protons start their journey bound to a pair of electrons as negative hydrogen ions in the injection system. The injection system accelerates proton beams to a kinetic energy of 450 GeV through a series of linear and synchrotron accelerators, as shown in Figure 3.4.[64] First, the negative hydrogen atoms are accelerated in a linear accelerator (Linac2 until 2018, which has now been replaced by Linac4).[65] Next, the two electrons

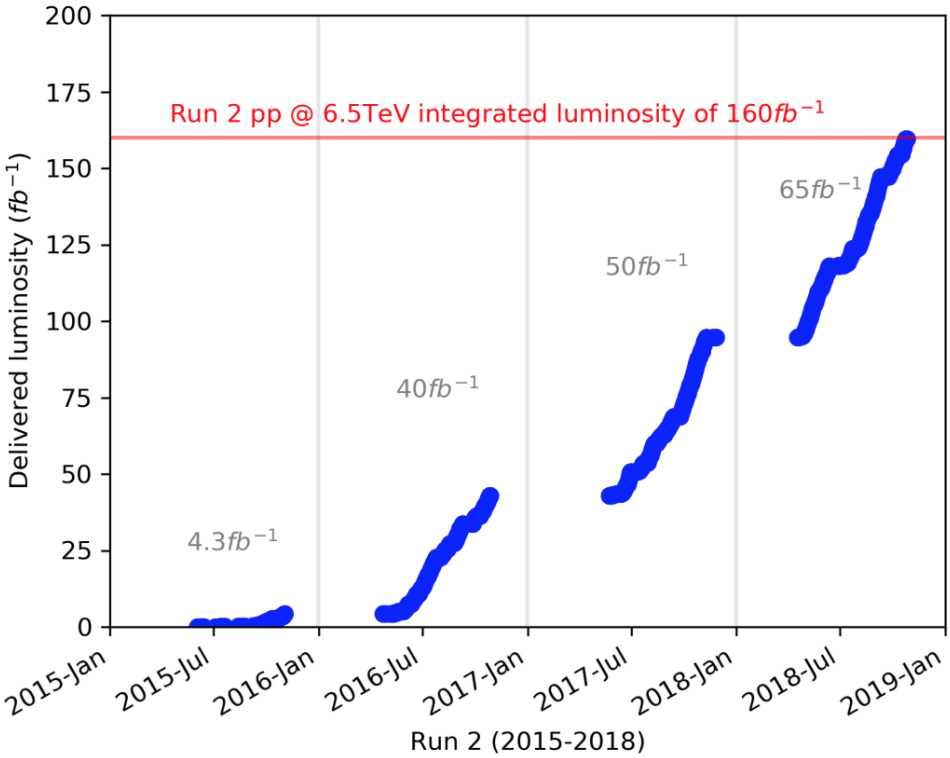

Figure 3.3: Integrated luminosity increased during each year of Run 2 from 2015-2018, reaching a total of nearly 160 fb^{-1}.[63]

are stripped from each hydrogen ion as they are injected in to the Proton Synchrotron Booster (PSB), so that only a proton remains. Next, the protons are accelerated and injected into the Proton Synchrotron (PS), where the beam energy increases to 26 GeV. The final 450 GeV injection energy is reached when protons accelerate in the Super Proton Synchrotron (SPS).[65]

Protons travel to the two LHC beam pipes, circulating in opposite directions through ultrahigh vacuum chambers. Each LHC ring takes only 4 minutes and 20 seconds to fill with protons, but the proton beams usually circulate through the beam pipes for hours before the beams are positioned to collide in one of the four detectors.[65]

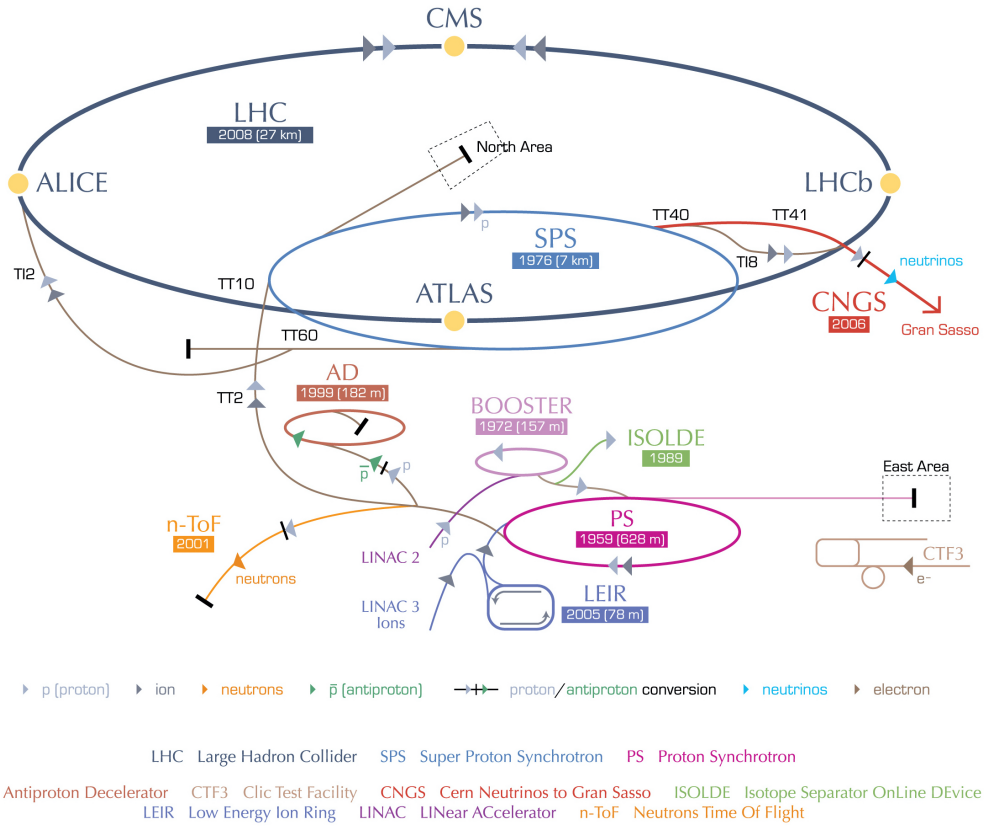

Figure 3.4: The accelerator complex at CERN, which includes several linear and synchrotron accelerators to boost the protons to travel up to 99.9999991% the speed of light.[66]

Chapter 4

The ATLAS Detector

The general-purpose detector used for this analysis is ATLAS: A Toroidal LHC ApparatuS (ATLAS) and is depicted in Figure 4.1. The ATLAS detector weighs about 7,000 tonnes (about the same as the Eiffel Tower), measures 44 m in length (almost the length of an Olympic-size swimming pool) and 25 m in height (approximately 6 stories tall). It measures the momentum and energy of neutral and electrically charged particles passing through its multiple layers.

Each layer of the detector– the inner detector, calorimeters, and muon spectrometer– is optimized to detect certain types of particles as shown in Figure 4.2. Each detector layer must also be designed with different considerations for the granularity, radiation hardness, momentum resolution, and sensor size needed for the measurement. Leptons and photons are well-measured in the region $|\eta| < 2.5$ with the detector, while jets and missing transverse energy are reconstructed from energy deposits in the full range of calorimeter $|\eta| < 4.9$. Various detector components are developed, tested, and assembled

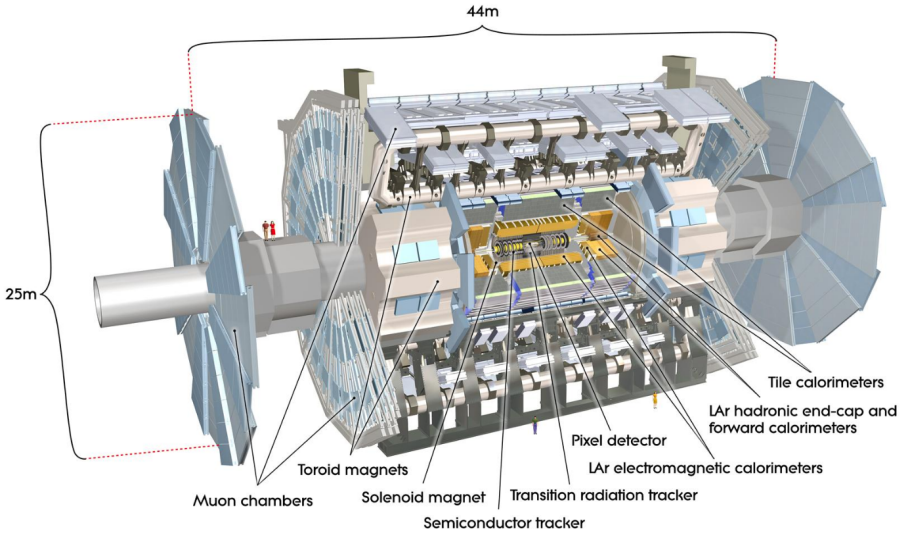

Figure 4.1: The ATLAS Detector measures 44 m in length and 25 m in diameter. Its main components are the inner detector (containing the pixel detector, semiconductor tracker, and transition radiation tracker), calorimeters, and muon spectrometer.[67]

by ATLAS member institutes around the world before they are all assembled together at LHC Point 1, where they make up the largest physics experimental apparatus ever built.

The ATLAS Detector uses a right-handed coordinate system, with the interaction point defining the origin of the coordinate system. The positive x-axis points from the interaction point towards the center of the LHC, while the y-axis points upwards. The $x-y$ plane coordinates are used in defining the transverse momentum p_T, transverse energy E_T, and missing transverse energy E_T^{miss}. The pseudorapidity is defined as $\eta = -\ln[\tan(\frac{\theta}{2})]$, where θ is the angle relative to the beam axis: $\eta = 0$ at an angle perpendicular to the beam axis, while $\eta = \infty$ parallel to the beam axis, depicted in Figure 4.3. η is used in the ATLAS experiment because it is nearly Lorentz invariant

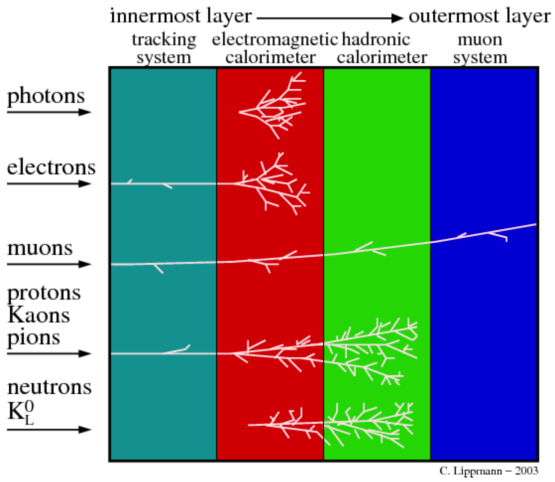

Figure 4.2: Each layer of the detector is designed to detect and track different types of particles.[68]

under boosts along the beam axis. The z-axis points along the beam axis with the positive direction in the counterclockwise direction when viewed from above, ϕ is the azimuthal angle around the beam axis, and pseudorapidity η is related to the polar angle relative to the positive z-beam axis. The metric distance ΔR between two 3-vectors is defined as $\Delta R = \sqrt{\Delta\eta^2 + \Delta\phi^2}$.[69]

4.1 Inner Detector

The inner detector (ID) is the part of the ATLAS detector closest to the beam line, and is made up of barrel and endcap regions. Its purpose is to measure the direction, momentum, and charge of electrically charged particles in coordination with a 2 T magnetic field from the superconducting solenoidal magnet that surrounds the inner detector. The ID's three main components, from closest to the beamline outwards, are the pixel detector, Semiconductor Tracker (SCT), and Transition Radiation Tracker

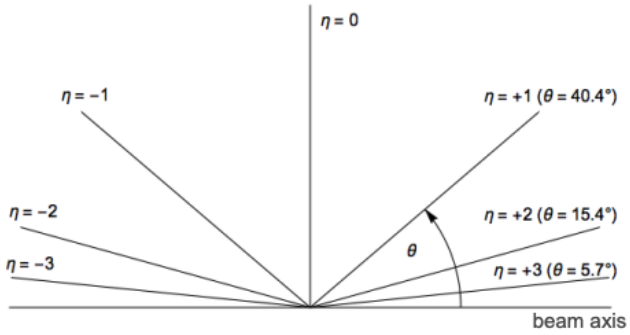

Figure 4.3: Pseudorapidity coordinates used in the ATLAS experiment are defined relative to the beam axis, with $\eta = 0$ perpendicular to the beam axis and $\eta = \infty$ parallel to the beam axis.[70]

(TRT) as shown in Figures 4.4 and 4.5. These three components of the inner detector have different trade-offs in terms of measurement resolution, number of readout channels, radiation damage, and abilities to track different types of particles. The pixel region has the best resolution, but that also necessitates more channels and more readout electronics. This is advantageous close to the beam line because there is a dense concentration of particle hits on the detector in this small-radius region. At larger radii, particles hitting the detector are more spread out so silicon strips are used in order to use fewer channels. The outer-most layer of the inner tracker is the TRT, which tracks charged particles and identifies electrons through their transition radiation.

4.1.1 Pixels

The first part of the ATLAS detector that particles pass through after colliding is the Pixel detector, which is located only 3.3 cm from the beamline.[73] Due to the high density of charged particles passing through this region close to the beamline, high precision of 10 μm in more than 92 million pixels corresponding to 92 million electronic

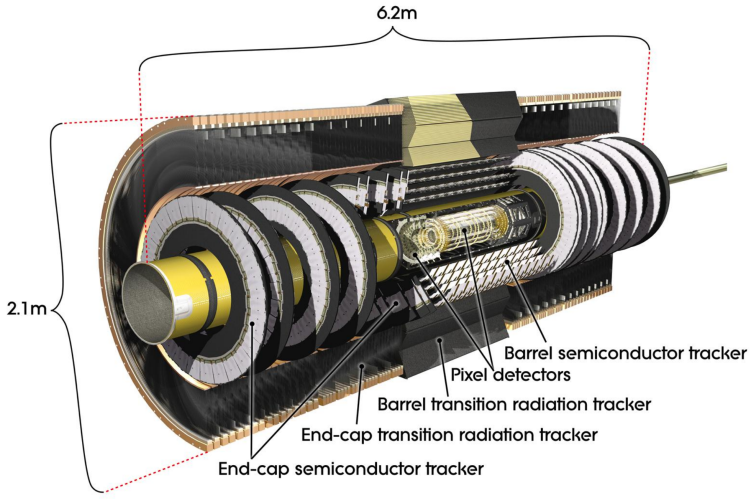

Figure 4.4: The ATLAS Inner Detector includes the barrel and end-cap regions of the pixel detector, semiconductor tracker (SCT), and transition radiation tracker (TRT).[71]

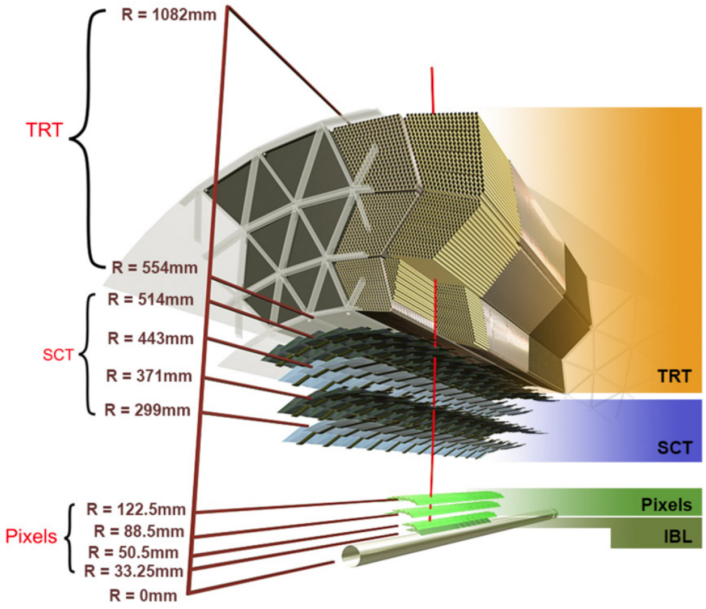

Figure 4.5: A view of the ATLAS Inner Detector cross section, showing the IBL, Pixel, SCT, and TRT layers at various radii.[72]

readout channels is needed to reconstruct events. The Pixel Detector enables four-layer measurements of charged particle tracks in the barrel and three-layer measurements in each endcap, with 50 x 400 μm^2 pixels. A 2 T solenoidal magnetic field surrounds the Pixel Detector for the purpose of bending charged particles in a range of $|\eta| < 2.5$ and reconstructing primary and secondary vertices from momentum and charge measurements.[74]

The Pixel Detector includes the Insertable B-Layer (IBL), which was installed in 2014 and is the inner-most layer with pixels 50 x 250 μm^2 in size. The IBL was designed to withstand high radiation up to a fluence of 2.5×10^{15} MeV $n_{eq} cm^{-2}$ and high occupancy, to preserve or better the performance of ATLAS achieved during Run 1 even after radiation damage to the B-Layer.[75] It takes advantage of 3D sensors and Complementary Metal-Oxide Semiconductor (CMOS) 130 nm technology for the first time in high energy physics.[76] The largest difference with 3D sensors is the electrode geometry compared to traditional planar sensors, which utilizes electrodes etched into the detector surface in a configuration of n and p-type columns instead of in a planar electrode layout on the detector surface.[76] This 3D sensor configuration lowers the depletion voltage with electrodes closer together, and reduces the charge carriers' drift distance and charge collection time, creating a more radiation-hard sensor.[76]

4.1.2 SCT

The Semiconductor Tracker (SCT) consists of 4,088 silicon strip sensor modules and over 6 million readout channels that are divided among four layers of silicon-strip

sensors in the barrel and nine disks in each of the two endcaps.[77] The SCT measures transverse momentum of charged particles at radial distances $299 < r < 560$ mm.[77] Rectangular $p^+ - on - n$ silicon sensors with a pitch of 80 μm make up the barrel modules, and are read out with custom-designed ASICs. Endcap modules are trapezoidal in shape with similar dimensions to those in the barrel.

The SCT operates at 0° C, and registers a "hit" if the binary threshold around 1 fC is surpassed.[77] Particle tracks can be reconstructed from four space-points in the SCT, and can be measured with a precision of 25 μm.[73] With its proximity to the beamline, the SCT was designed to operate despite effects from radiation damage.

Some of the Run 2 upgrades implemented for the SCT include additional Read Out Drivers (ROD), more aggressive data compression, automatic recovery mechanisms for modules and RODs, improved cooling, and reduced calibration time.[77] In addition, Single Event Upset (SEU) mitigation was implemented to globally reconfigure the front-end ASICs every 90 minutes to make sure the registers are correct. During Run 2, the SCT faced radiation damage due to much higher than expected pile-up (60 versus 23 interactions per bunch crossing). Despite the radiation damage, 99% of modules were still alive at the end of the run, leaving only 1% disabled. As a result of the radiation damage, the high voltage was increased from 150V to 200-250V.[77]

4.1.3 TRT

The Transition Radiation Tracker (TRT) is the outer-most layer of the Inner Detector (ID), and is the only part of the ID composed of gas-filled straw tubes instead

of silicon. 300,000 straw tubes 4 mm in diameter are maintained at a -1.5 kV voltage. Each tube contains a grounded 30 μm gold-plated tungsten wire through the center, so each tube acts as a proportional counter and can detect charged particles moving through. 50,000 straw tubes make up the barrel region, while 250,000 straw tubes are in each endcap, giving the TRT the ability to measure tracks with a precision of 0.17 mm.[73]

The TRT's role is to track and identify electrons: Electrons traveling at relativistic speeds may emit a transition radiation photon as they traverse a material boundary (polymer fibers in the barrel or foils in the endcaps), which ionizes the gas in the tube and creates an electric signal that drifts towards the wire. The signal is amplified and readout by the front-end electronics into 24 time bins and is required to pass a 300 eV threshold.[78] Although transition radiation can be emitted by other highly relativistic charged particles, electrons are targeted because the transition radiation photon is created at a frequency which Xe (expensive gas used during Run 1) and Ar (cheaper gas used during Run 2, similar tracking ability to Xe[79]) gas are sensitive to and because the transition radiation effect depends on $\gamma = E/m$ which is highest for electrons.[78] Since the electrons' readout signals are higher, a 6 keV high threshold is used to help distinguish electrons from other charged particles.[78]

The TRT operates at room temperature, which requires some insulation from the SCT operating at 0° C.

4.2 Calorimeters

4.2.1 Electromagnetic Calorimeters

The Electromagnetic Calorimeter is a sampling calorimeter, composed of alternating absorption and active layers. It measures the energy of electrons and photons, identifies position and direction of photons, and is the first layer to measure hadronic showers in the barrel ($|\eta| < 1.475$) and end cap regions ($1.375 < |\eta| < 3.2$). The LAr hadronic endcap (shown in Figure 4.6) is essential for measuring forward jets. The Liquid Argon (LAr) active material detects electrons and photons, and alternates between layers of lead absorbers so that the radiation length is shortened to about 22 radiation lengths and the cryostat can be constructed at a reasonable size. Energy losses that occur in the material upstream of the EM calorimeters are corrected using a thin LAr presampler layer for the region $|\eta| < 1.8$.[80] LAr is an attractive material for the calorimeter because it is intrinsically radiation resistant.

The LAr calorimeter cells are rectangularly shaped in the first layer (the cells in the other layers are square), with the longer dimension in the ϕ direction, as shown in Figure 4.7. This enables good η resolution in the first layer of strips so that prompt photons are distinguishable from those that decayed from π^0's. The pair of converted photons are spread by the magnetic field, so the rejection power in the azimuthal direction is obscured. This is also advantageous because the fake photons can be recorded as originating from the same event, and because resolution of the shower position and direction measurements are improved.[43] Arranging the LAr calorimeter in an accordion

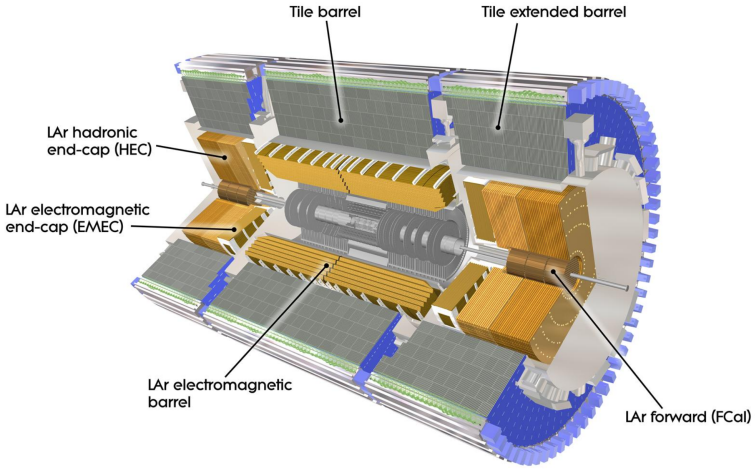

Figure 4.6: The ATLAS Calorimeters include the LAr electromagnetic calorimeters and the hadronic tile calorimeter (TileCal). The LAr hadronic calorimeters are located in the ATLAS detector barrel and endcaps, while the TileCal is only in the ATLAS detector barrel and extended barrel.[80]

design, visible on the right side of the cut-out in Figure 4.7, helps to avoid dead spaces where particles might pass through a crack.

4.2.2 Hadronic Tile Calorimeter

The Hadronic Tile Calorimeter (TileCal) is located outside the LAr Calorimeter, and is important for making precise measurements of hadrons, jets, τ particles, and missing transverse energy. It is made up of alternating layers of scintillating plastic as active medium with iron plates as absorbers. The TileCal covers the central region of the ATLAS detector and has a fixed central barrel and two moveable extended barrels. The tiles are 3 mm thick, and a $4.7:1$ iron-to-scintillator ratio allows both a good sampling frequency and a compact calorimeter size, with a 20.7 cm nuclear interaction length.[82] The total tile calorimeter depth is 7.4λ at $\eta = 0$.[82]

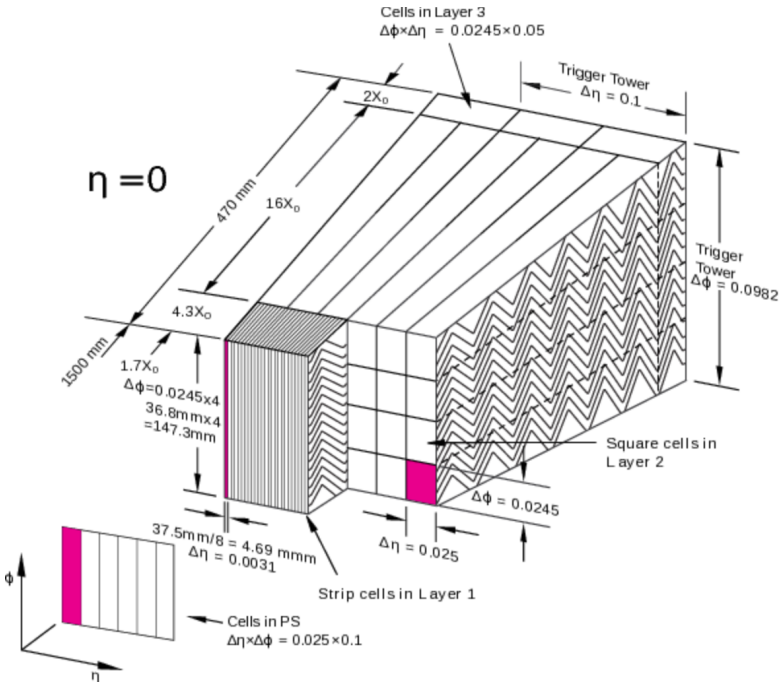

Figure 4.7: The ATLAS LAr Calorimeter Cell geometry. The cell dimensions in the first layer are rectangular for better η resolution. The accordion geometry design avoids gaps in the detector and is visible on the right side of the cut-out.[81]

Scintillation light produced in each cell tile is read out with wavelength shifting fibers that are coupled to two photomultiplier tubes (PMTs).[82] Every 25 ns, electronic signals from a total of 10,000 PMTs are measured and digitized. The non-uniform behavior of the tile response and the requirement to minimize fiber length are two challenges of the TileCal.

4.3 Muon Spectrometer

The Muon Spectrometer (MS) identifies and measures momenta and position of muons, and is situated in the field of three large superconducting air-core toroids. The cylindrical detector covers a large rapidity range up to $|\eta| < 2.7$, and has a diameter of 22 m and length of 44 m.[83] The MS was specially designed to measure high transverse momentum muons with good resolution.[84] Muon triggering occurs in the MS up to $|\eta| = 2.4$, and high precision drift and multiwire proportional chambers allow for precise tracking with 50 μm resolution in the Muon Spectrometer.

The Muon Spectrometer's main components are the Thin Gap Chambers (TGC), Resistive Plate Chambers (RPC), Monitored Drift Tubes (MDT), and Cathode Strip Chambers (CSC). The TGC contain 440,000 channels and are used for L1 muon triggering and measuring the $r - \phi$ non-bending coordinate of muons in the endcaps. The RPC are also used for triggering, but measure the $r - \phi$ non-bending coordinate in the barrel region of the detector with 380,000 channels. Two layers of RPC supply the low-p_T threshold, while a third outer layer contributes to the trigger for the high-p_T

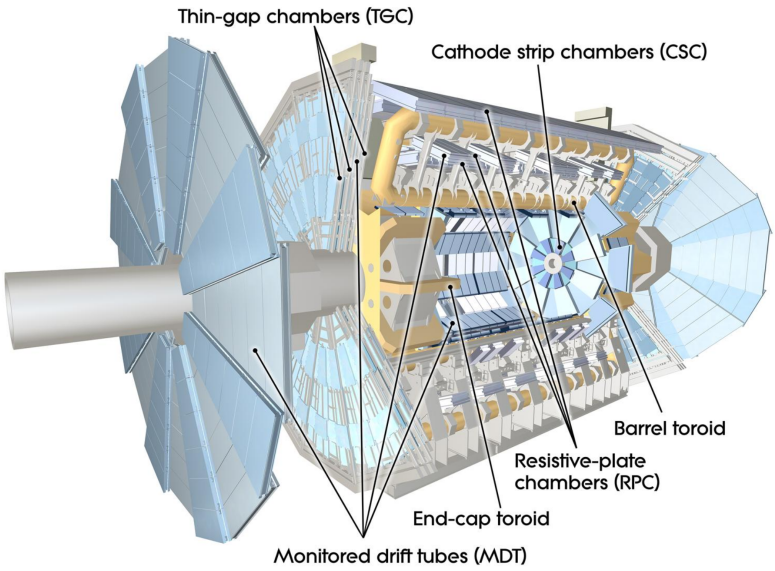

Figure 4.8: The ATLAS Muon Spectrometer measures muon momentum. Its main components are the Thin Gap Chambers, Monitored Drift Tubes, Cathode Strip Chambers, and Resistive Plate Chambers.[87]

threshold. As shown in Figure 4.9, the muon trigger searches for coincident hits on multiple layers (stations) of the the TGC and RPC that are possibly from muons with a primary vertex at the origin.[85]

The MDT are composed of drift chambers of 350,000 aluminum tubes filled with gas (93% Ar + 7% CO_2) that precisely measure the muon momentum and $r - z$ bending coordinate of tracks.[84] During Run 2, the average single-hit spatial resolution was measured to be 81.7 ± 2.2 μm, which directly affects the ability of the MS to measure muon momentum.[86] The CSC are multi-wire proportional chambers with segmented cathodes, and have excellent spatial resolution of 60 μm in the $r - z$ bending plane and high counting rate capabilities.[84]

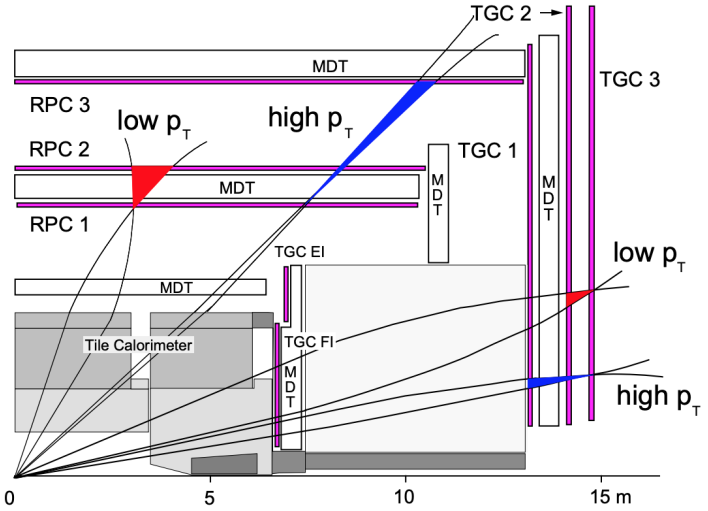

Figure 4.9: A cross section of the ATLAS Muon Spectrometer showing the chambers used for triggering on low-p_T and high-p_T muons. A coincidence of hits in the RPC layers is required in the barrel region for triggering, while a coincidence of hits in the TGC layers is required in the endcap region for triggering.[85]

4.4 Magnet System

The force on a charge is given in classical electromagnetism by the magnetic force $\mathbf{F} = q(\mathbf{v} \times \mathbf{B})$, where q is the charge of the particle, $\mathbf{v}$ is the velocity, and $\mathbf{B}$ is the magnetic field strength. This is the same force that acts on the charged particles moving through the magnetic fields generated by solenoidal and toroidal magnets in the ATLAS detector, shown in Figure 4.10. These magnetic fields are essential for bending charged particles so that their momentum and charge can be measured. The magnetic field strength is increased by operating the magnet systems at $-268°$ C.[88]

In addition to inspiration for the ATLAS name, the toroidal magnets are important for creating the 3.5 T·m magnetic field necessary for measuring muon momentum.

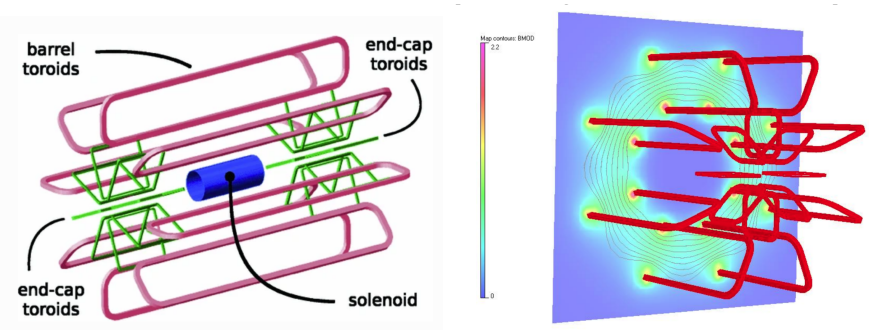

Figure 4.10: ATLAS toroidal and solenoidal magnets (left) and the resulting magnetic field in the endcap toroid region (right).[89, 90]

The 25.3 m long, 830 tonne central toroid that surrounds the experiment is the world's largest toroidal magnet. It is made up of 8 coils and has 56 km of superconducting wire. In addition, 16 coils make up two toroidal magnets 10.7 m in diameter at the ends of the experiment to create a magnetic field to detect particles escaping along the beam pipe.[88]

The solenoidal magnet encases the ATLAS Inner Detector, and provides a magnetic field of 2 T that bends charged particles for the purpose of measuring momentum. It is 5.6 m long, 2.56 m in diameter, and weighs more than 5 tonnes. Potential interactions are minimized between the magnet and particles of interest through the use of 9 km of niobium-titanium wires (a super conducting material with a high critical magnetic field and high critical supercurrent density) that are embedded into aluminum ribbons.[88]

4.5 Data Acquisition and Triggers

The ATLAS detector is monitored from the Point 1 ATLAS Control Room at CERN. The combined collision cross section exceeds more than 60 million megabytes per

second, so it is necessary to quickly reduce the amount of collision data saved for offline analysis. To achieve this, a two-level trigger system is used: the Level 1 (L1) hardware Trigger and High-Level software Trigger (HLT).

The L1 Trigger uses custom-built hardware to select events with distinguishing characteristics, and save up to 100,000 events per second for the HLT. A decision to keep or reject the event is made < 2.5 μs after it occurs, reducing data from a rate of 40×10^6 events each second to 100,000 events each second.[91] It is divided into the L1Calo and L1Muon subsystems, for triggering on inputs from the corresponding calorimeter and detectors. Kinematic cuts, frequently based on angular distance or particle pair invariant mass, are also made with the L1 topological trigger (L1Topo). After passing through the L1 Trigger which has coarse inputs, the software-based HLT is used to further reduce data and match offline selection more closely.

The HLT is a large farm of CPUs that refines the analysis of hardware L1 trigger. The HLT examines the whole event in selected layers of the detector, or looks at data in smaller regions of the detector. It uses various particle identification and pile-up rejection algorithms, and keeps about 1,000 events each second for offline analysis. As the LHC operates at increasingly higher energies, the trigger system plays a larger role in reducing the large number of pile-up events.

4.5.1 Detector Control System

The ATLAS Detector is controlled and monitored by the Detector Control System (DCS) in the Point 1 ATLAS Control room using WinCC OA, a software used

for industrial systems. The DCS allows monitoring of all of the ATLAS subdetectors and equipment, utilizing over 100 server machines. The DCS alerts the control room operators to any warnings or errors, points them to the section of the detector (or hardware communicating with that part of the detector) that may need attention, and archives any issues. This makes error handling easier to recognize and address. Properties of the detector and hardware that are monitored with the DCS include current, voltage, temperature, and power. Example DCS screens are shown in Figures 4.11 and 4.12. The DCS enables experts to recover problems or reset systems remotely in some cases, instead of going underground to do so.

One component of the DCS is the Final State Machine (FSM), which is the tree-like hierarchical structure that monitors states and statuses of each of the detector components and subdetectors of the experiment, all the way down to even a single channel of a piece of equipment working in conjunction with the detector. If there are problems with the "child" nodes, the states and statuses of "parent" nodes will be alerted.

4.6 High Luminosity Large Hadron Collider

Starting in 2026, the LHC will be upgraded to operate during Run 4 at a rate of 8 billion collisions per second, with $< \mu >$=200 collisions per bunch. ATLAS will need to determine the primary vertex for all these close collisions, despite this huge increase in pile-up. The current ATLAS detector will not be able to keep up with the

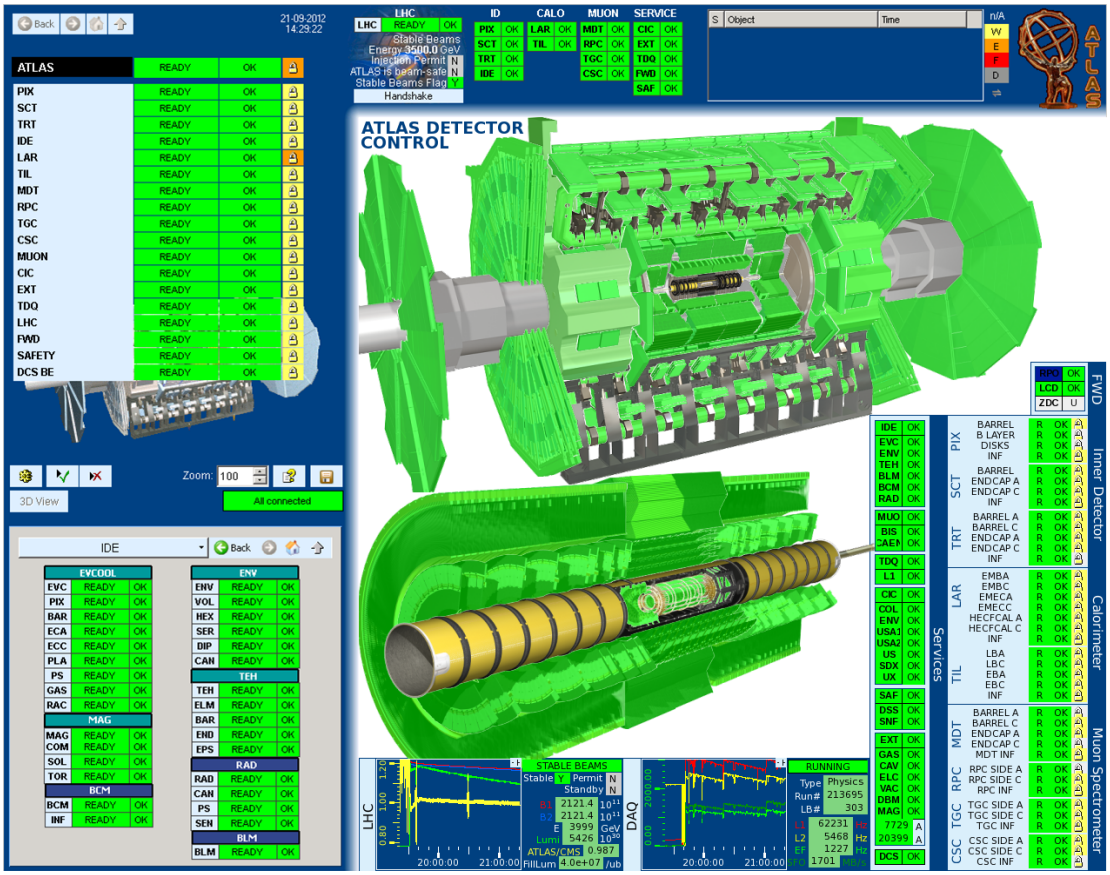

Figure 4.11: An example of an ATLAS DCS screen. This top-level screen shows each of the detector components, and clicking on any of them would bring up a screen showing additional details for that part of the detector. Lots of green means it is operating well! Warnings, errors, and fatal errors would appear in yellow, orange, and red, respectively.[92]

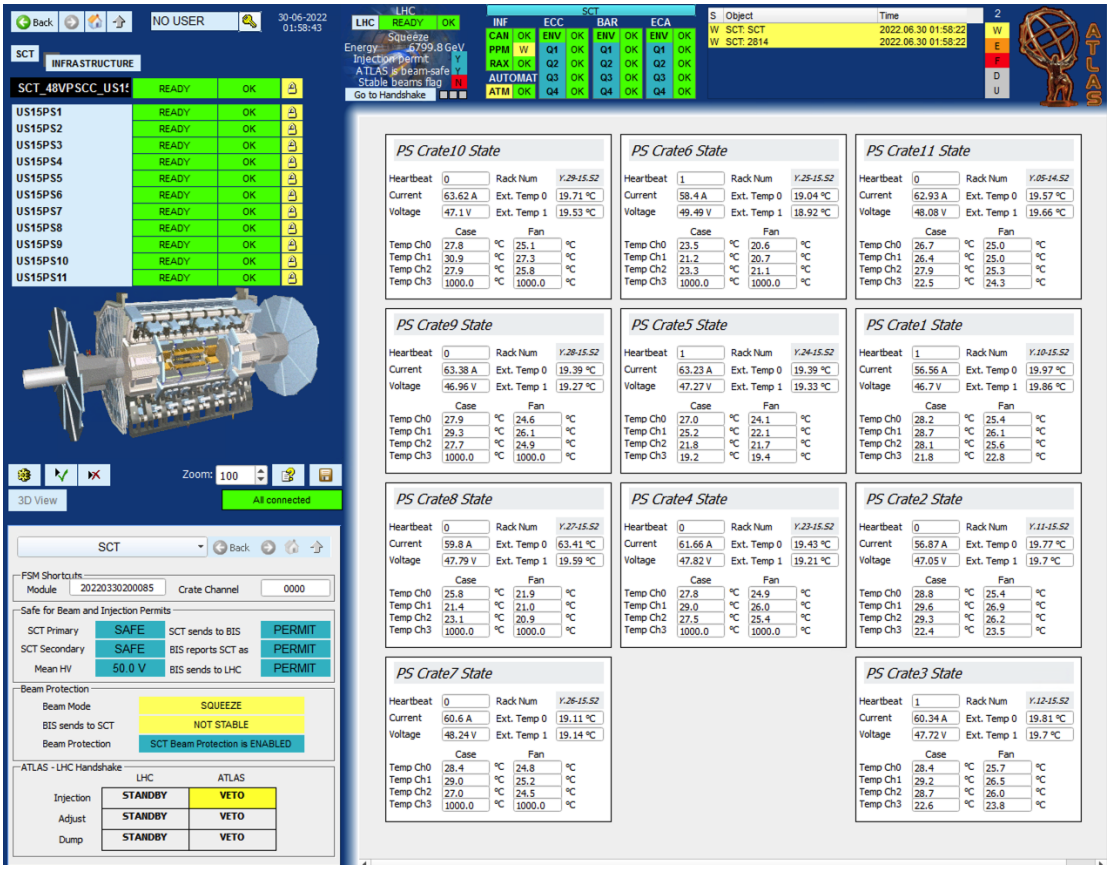

Figure 4.12: An example of an ATLAS DCS screen, in this case for monitoring the 11 crates of the SCT 48 Volt Power Source in US15.

collision rate expected for the pile-up that will be seen at the HL-LHC. The current ID is already operating at close to its bandwidth limit with the current pile-up.[93] Both the ID and LHC magnets will come to the end of their lifetimes at the end of Run 3, as a result of radiation damage. To keep up with the high increased data rates and enable high-performance tracking at the LHC, a new all-silicon Inner Tracker (ITk) will replace the ID.

In addition, adding timing as a fourth dimension for tracking will greatly mitigate the effects of pile-up. Improving the timing resolution of the silicon detectors will allow seemingly random particle hits that are close in space but separated by time to be resolved as unique particle tracks, so that a primary vertex for each event is more identifiable, especially in the forward region.[94]

4.6.1 High Granularity Timing Detector

The High Granularity Timing Detector (HGTD) will be added for the HL-LHC upgrade to enable grouping particle hits by time in order to reconstruct events.[94] It will be located at a position at $z = \pm 3.5$ m from the interaction region, outside the silicon tracking system and in front of the endcap cryostats as shown in Figure 4.13. It will consist of two layers on each side of ATLAS, and cover a radius from 120 mm to 640 mm and region $2.4 < |\eta| < 4.0$. With the increased collision rate of the HL-LHC, fast timing will be an essential degree of added data to improve pile-up jet rejection and forward object reconstruction, luminosity measurements for precision physics, and missing transverse energy measurements. Particularly, jet and lepton reconstruction will

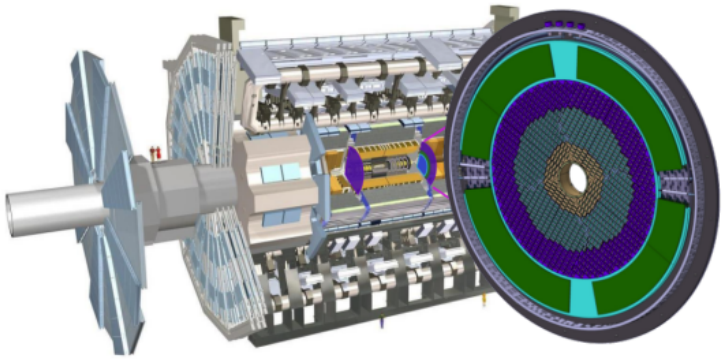

Figure 4.13: The High-Granularity Timing Detector will be inserted in the ATLAS detector between the silicon tracking system and endcap cryostats during the upgrade for the HL-LHC.[94]

improve.

The HGTD will make use of Low Gain Avalanche Detectors (LGADs), an example of which is depicted in Figure 4.14a. LGADs are like ordinary n-on-p silicon detectors, but have an additional highly doped p-layer under the n^+ electrode.[95] LGADs have a low internal gain close to 20, allowing improved signal-to-noise ratio, a higher slew rate, and thinner sensors. They are useful in ATLAS because they have a time resolution faster than 30 ps and a high rate capability. Good position resolution is also a characteristic of LGADs due to the finely pixelated sensors. 15x15 arrays are surrounded by a guard ring to help ground the charges, as shown in Figure 4.14b, and will be used for the ATLAS HGTD.[94] 25x25 arrays will be used in the final design for the HGTD to cover a larger area while maintaining good position resolution. The breakdown voltage of each pixel in the array can be quickly checked for quality control purposes using a probe card and readout system custom-built at UC Santa Cruz and University of

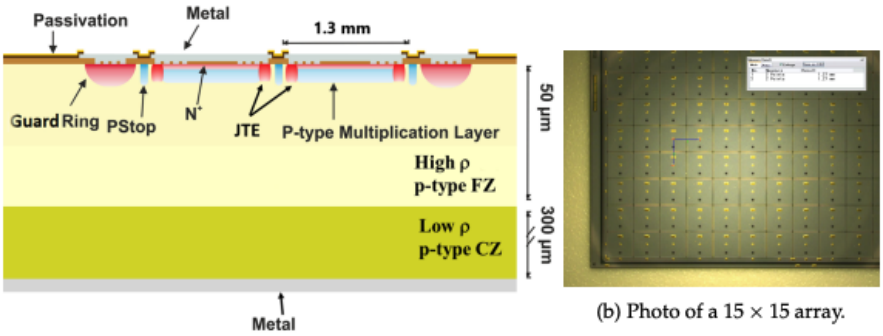

Figure 4.14: (a) A LGAD cross section shows the different components of an n-on-p silicon sensor with an additional highly doped p-layer under the N^+ electrode, along with the guard ring and metal pads (b) photo of a 15x15 LGAD array.[94]

Science and Technology China. Five manufacturers currently make LGADs for ATLAS–

Hamamatsu Photonics (HPK), Centro Nacional de Microelectronica (CNM), Fondazione

Bruno Kessler (FBK), Brookhaven National Lab, and Micron Semiconductors.[96]

Part III

VBF $H(b\bar{b}) + \gamma$ Analysis

As described in Sections 1.6.2 and 2.3, the VBF $H(b\bar{b}) + \gamma$ signature is an interesting production mode that is yet to be observed experimentally. Its benefits include its dominant $H + \gamma$ cross section and WW fusion measurement. It also boasts a clean experimental signature from triggering on a high-energy photon and destructive interference of the QCD background diagrams. This channel provides the best opportunity to measure $H + \gamma$ production, and the dibosons involved are a good test of electroweak physics.

This channel was previously studied using the full datasets from Runs 1 and 2.[97] Using 132 fb^{-1} of Run 2 pp collision data at $\sqrt{s} = 13$ TeV collected with the ATLAS detector, the previously published measurement reported an excess of 1.3σ Higgs signal over background observed in data compared to 1.0σ expected.[97] Combined with the VBF all-hadronic channel which excludes the photon, an excess of 2.7σ was observed compared to an expected value of 2.9σ.[98].

The Run 2 Legacy Analysis for the VBF Higgs + photon channel presented here further refines the analysis strategy. The overall analysis strategy compares data and Monte Carlo samples (Chapter 5), reconstructs and selects physics objects that target the VBF $H(b\bar{b}) + \gamma$ signatures (Chapter 6), trains a neural network on MC to distinguish between signal and background events based on kinematic variable inputs (Chapter 7), models signal and background (Chapter 8), and fits to the neural network output MC template with considerations of theory and statistical uncertainties to extract a measurement of the Higgs boson signal (Chapter 9). Extending and updating background Monte Carlo samples, training a dense neural network instead of a boosted decision tree,

and optimizing binned-liklihood signal and background model fitting techniques are new strategies used in this legacy analysis.

Chapter 5

Data Samples and Monte Carlo

5.1 Data Samples

LHC pp collision data at a center-of-mass energy of 13 TeV was collected with the ATLAS detector during the full Run 2 campaign from 2015-2018. 132 fb^{-1} of data are used in this analysis, which is slightly less than the full 139 fb^{-1} used in most Run 2 analyses. This is because the VBF analysis triggers were not available at the beginning of the 2015 and 2016 runs, which reduced the integrated luminosity in the run corresponding to 0.8 fb^{-1}. In addition, using Good Run Lists (GRLs) that were specific to b-jets rejected events for outdated and invalid beamspots when an online b-tagging algorithm was included in the trigger, further reducing the integrated luminosity by 6.2 fb^{-1}.

Slightly different triggers to target the VBF $H + \gamma$ signal were used during each data-taking campaign. The triggers for each dataset and corresponding luminosity

are summarized in Table 5.1. Other available unprescaled VBF+photon triggers during Run 2 are described in Appendix A.

Dataset	Trigger chain	Integrated luminosity
data15 F3 - J data16 A - F	HLT_g25_medium_L1EM22VHI_4j35_0eta490_invm700	$2.53\,\text{fb}^{-1}$ $14.96\,\text{fb}^{-1}$
data16 G - L	HLT_g25_medium_L1EM22VHI_j35_0eta490_bmv2c2077_split_3j35_0eta490_invm700	$13.24\,\text{fb}^{-1}$
data17 data18	HLT_g25_medium_L1EM22VHI_j35_0eta490_bmv2c1077_split_3j35_0eta490_invm700	$43.53\,\text{fb}^{-1}$ $57.70\,\text{fb}^{-1}$

Table 5.1: Summary of triggers used for selecting the data samples in different data-taking periods in this analysis. The total integrated luminosity in the good run lists for these triggers is $132\,\text{fb}^{-1}$.

The 0-btag trigger HLT_g25_medium_L1EM22VHI_4j35_0eta490_invm700 was used early on in Run 2 for datasets taken in 2015 and 2016 through Period F. It requires an isolated EM object with $E_T > 22$ GeV as the Level-1 (L1) seed. In the HLT, the 0-btag trigger requires at least one central photon as well as four jets with $E_T > 35$ GeV and $|\eta| < 4.9$. In the HLT, the photon E_T cut is increased slightly to 25 GeV and photons must pass the "medium" identification criteria. The event must also contain a pair of jets with a large invariant mass of at least 700 GeV. The largest dijet mass for an event is calculated from all possible jet pairs in the event, including jets with $E_T < 35$.

Since 2016 Period G, the minimum largest dijet mass requirement of the 0-btag trigger was increased to 1000 GeV due to the increase in the trigger rate as the instantaneous luminosity went up. This minimum largest dijet mass requirement was too tight for our signal phase space, so we switched to the 1-btag trigger HLT_g25_medium_L1EM22VHI _j35_0eta490_bmv2c2077 _split_3j35_0eta490_invm700, which only requires a 700 GeV cut on the largest dijet mass. The 1-btag trigger still requires at least one central photon plus four jets with $E_T > 35$ GeV and $|\eta| < 4.9$, but

at least one of those jets must be b-tagged online with the MV2c20 at 77% working point to reduce the trigger rate. These b-tagging options are described in Section 6.3.

Figure 5.1 shows the Medium photon trigger HLT_g25_medium_L1EM20VH efficiency as a function of the offline photon transverse energy.[99] The efficiency steeply drops when photon E_T is below 30 GeV, motivating the 30 GeV minimum cut for photons described later in this analysis.

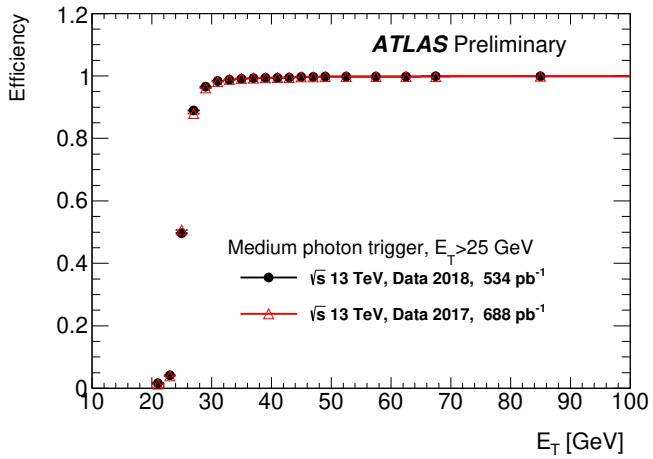

Figure 5.1: The Medium photon trigger HLT_g25_medium_L1EM20VH efficiency as a function of the offline photon transverse energy. The efficiencies were measured on events triggered by either a loose and lower E_T HLT trigger or by a L1-only trigger from 2017 and 2018 data.[99] Trigger efficiency sharply drops for photons with E_T less than 30 GeV.

Figures 5.2 and 5.3 show the trigger efficiencies measured from data and Higgs signal MC for various data-taking periods. Overall, data and MC efficiencies agree within uncertainty. The trigger efficiency drops sharply for m_{JJ} below 800 GeV, motivating the requirement for events with m_{JJ} greater than 800 GeV described later in the event selection. Above 800 GeV, the small differences between data and MC trigger efficiencies

are due to the inefficiency of the b-jet trigger in data and will be corrected with the jet-level scale factor (SF) from the ATLAS b-jet trigger group.[56]

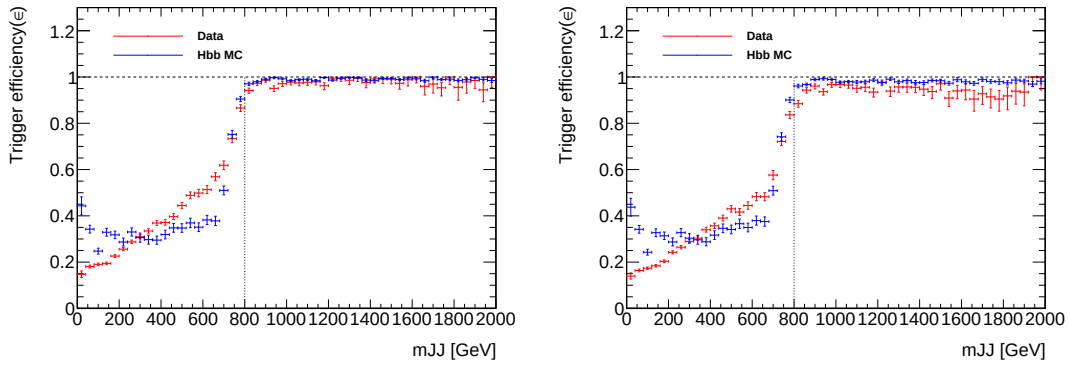

(a) 0 b-jet trigger 2015-2016

(b) 1 b-jet trigger 2015-2016

Figure 5.2: The trigger efficiency as a function of offline m_{JJ} for (a) VBF 0 b-jet trigger used in 2015 and 2016 (before Period G) and (b) VBF 1 b-jet trigger used in 2016 (starting with period G). The difference between data and MC trigger efficiency is measured by the b-jet trigger group and is corrected in the analysis as a jet-level scale factor.[56]

The following Good Runs Lists (GRLs) are used in this analysis:

- physics_25ns_21.0.19.xml
- data16_13TeV.periodAllYear_DetStatus-v89-pro21-01_DQDefects-00-02-04_PHYS_StandardGRL_All_Good_25ns_BjetHLT.xml
- data17_13TeV.periodAllYear_DetStatus-v99-pro22-01_Unknown_PHYS_StandardGRL_All_Good_25ns_BjetHLT_Normal2017.xml
- data18_13TeV.periodAllYear_DetStatus-v102-pro22-04_PHYS_StandardGRL_All_Good_25ns_BjetHLT.xml

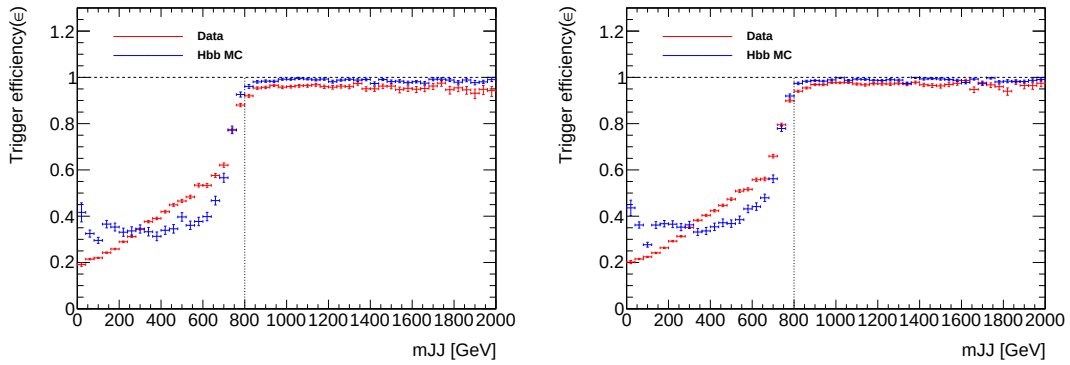

(a) 1 b-jet trigger 2017

(b) 1 b-jet trigger 2018

Figure 5.3: The trigger efficiency as a function of offline m_{JJ} for (a) VBF 1 b-jet trigger used in 2017 and (b) VBF 1 b-jet trigger used in 2018. The difference between data and MC trigger efficiency is measured by the b-jet trigger group and is corrected in the analysis as a jet-level scale factor.[56]

5.2 Monte Carlo Samples

MadGraph 5 is used to calculate matrix-elements and produce parton-level Monte Carlo (MC) events because the other generators that are more commonly used in ATLAS (Sherpa, VBFNLO) do not have the VBF $H+\gamma$ process at this time.[100–102]

The MadGraph 5 process syntax for each of the samples is summarized in Table 5.2. Detailed explanations of the process syntax can be found in Appendix C. For the NLO and LO processes respectively, the `loop-sm_no_b_mass` and `no_b_mass` restriction is used for compatibility with the 5-flavor PDF scheme.

Table 5.3 summarizes the generator, cross section, filter efficiency, and number of generated events for all MC samples considered in this analysis. The filter efficiency is not equal to one when MadGraph cannot select a specific final state as defined by the process such as in Table 5.2, so events that do not pass all the cut requirements are

generated. Applying a generator filter cuts events that fail the criteria. Only events that meet the cut requirements are passed to the MC production detector simulation and reconstruction steps, which are computationally expensive.[103] This means that events passing all the cut criteria are generated more efficiently.

Sample	Type	Process	Model
HbbjjaSM125	NLO Signal	p p > h a j j [QCD]	loop_sm-no_b_mass
ZbbjjaEWK	NLO Background	p p > z a j j QCD=0 [QCD]	loop_sm-no_b_mass
ZbbjjaQCD	LO Background	p p > z a j j QED=2 QCD=10, z > b b~	sm-no_b_mass
NonResbbjja	LO Background	p p > b b j j a $ z h	sm-no_b_mass
NonResccjja	LO Background	p p > c c j j a $ z h	sm-no_b_mass

Table 5.2: Summary of MadGraph 5 processes for NLO signal and LO background samples. The $HbbjjaSM125$ and $ZbbjjaEWK$ NLO samples do not include the decay to b-quarks in the MadGraph 5 process because the decay occurs after generation in the showering and using MadSpin, respectively. The LO samples include b-quarks directly in the generation.

Sample	Generator	x-sec	Filter efficiency	Total generated events
HbbjjaSM125	aMC@NLO+Herwig 7	32.3 fb	1	13.8M
ggH+photon	Powheg +Pythia	28.301 pb	0.046	1.8M
ttH (all-hadronic)	Powheg +Pythia 8	238.55 fb	1	10M
ttH (semi-leptonic)	Powheg +Pythia 8	523.330 fb	0.43869	10M
ZbbjjaEWK	aMC@NLO+Herwig 7	74.7 fb	1	10.2M
ZbbjjaQCD	MadGraph 5+Pythia 8	2.70 pb	1	0.739M
NonResbbjja	MadGraph 5+Pythia 8	674.9 pb	0.3649843	305.9M
NonResccjja	MadGraph 5+Pythia 8	1700 pb	0.3830862	50.94M

Table 5.3: Generator-reported cross sections for the MC samples used in this analysis, and the available statistics at generator level. The full container names can be found in Appendix B.

5.2.1 Signal sample

Signal $H(\to b\bar{b})$ Monte Carlo events are generated at next-to-leading-order (NLO) with MadGraph 5 v2.6.2, with the `PDF4LHC15_nlo_mc_pdfas` parton distribution function (PDF), and are interfaced to Herwig 7 for the parton shower and hadronization.

Parameter	Description	Value
parton_shower	Parton showering event generator	HERWIGPP
pdlabel	Use MG5 internal PDFs or LHAPDF interface	lhapdf
lhaid	LHAPDF PDF set ID	90000
maxjetflavor	Max. quark flavor number for applying cuts	5
ptj	Min. jet p_T	15.0
etaj	Max. jet η	-1.0
ptgmin	Min. photon p_T	19.0
epsgamma	ϵ_γ parameter of Frixione Isolation [104]	1.0
R0gamma	Radius of isolation cone of Frixione Isolation [104]	0.4
xn	n parameter of Frixione Isolation [104]	1
isoEM	Isolate photons from EM energy (photons)	True
etagamma	Max photon $\|\eta\|$	3.0

Table 5.4: NLO list of event generation parameters for the $H\gamma jj$ and EWK $Z\gamma jj$ that are different from the MadGraph 5 default values.

The PS/hadronization tune and UE/MPI tune are set to the Herwig 7 default values of `H7-PS-MMHT2014LO` and `H7-UE-MMHT`, respectively. Herwig 7 is used to avoid strange 3rd jet distributions in the VBF topology that are added when showering with Pythia 8. Details from these studies can be found in Appendix D. Herwig 7 is used to force Higgs bosons to decay to a pair of b-quarks.

The model `loop_sm-no_b_mass` was used for the 5-flavor PDF scheme at NLO. We use the default run card with modifications to the parameters listed in Table 5.4 at NLO.

The Frixione Isolation parameters `R0gamma`, `xn`, and `epsgamma` characterize the isolation phase-space between photons and jets, and together define photon isolation independent from contributions from parton-to-photon fragmentation.[104] Frixione defines:

$$\chi(\delta) = E_\gamma \epsilon_\gamma \left(\frac{1 - \cos\delta}{1 - \cos\delta_0} \right)^n \tag{5.1}$$

These photon isolation parameters, though arbitrarily assigned values by Frixione, are essential to defining the Higgs plus photon fiducial phase space–this is evident from a large change in cross section as photon isolation parameters are varied, changing the specified phase spaces.[104] The Higgs plus photon fiducial phase space is defined in this analysis to match the MadGraph 5 default values of `epsgamma`= 1.0, `R0gamma` = 0.4, and `xn`= 1.[104]

100,000 generator-level events were created using MadGraph 5 to determine the contributions of various production modes to the $H\gamma jj$ signal composition. At generator-level, VBF events make up $92.3 \pm 0.7\%$ of events produced. Most VBF events are produced via WW fusion because of the additional diagram where the photon radiates off of one of the fusing vector bosons. ZZ fusion is less common due to destructive interference between diagrams with the photon radiating off of the incoming and outgoing quarks, similar to the destructive interference that occurs for background QCD $b\bar{b}\gamma jj$. Although the analysis targets VBF $H + \gamma$ processes, the production cross sections from these generator-level studies suggest that $8.8 \pm 0.2\%$ of events are actually VH+γ. Table 5.5 below summarizes the signal composition study. Uncertainties on the cross sections make the total contribution sum to very close to 100%.

Contributions from the ggF process are also estimated with a MC simulated sample. Instead of producing a dedicated ggF $H + \gamma$ sample with MadGraph 5, a

photon-filtered sample using inclusive POWHEG ggF samples is produced to describe the $H+\gamma$ component. Due to Furry's theorem, the ggF $H+\gamma$ process with a photon emitted from the fermion loop is forbidden.[105] The photons appearing in ggF events are mainly from the non-prompt processes. Taking the offline selections into consideration, the filter is designed to require at least one photon with $p_{\mathrm{T}} > 25\,\mathrm{GeV}$ and within $|\eta| = 2.5$, corresponding to a filter efficiency around 4.6%.

Contributions from the $t\bar{t}H$ process are described with MC simulated samples produced using POWHEG interfaced with PYTHIA for parton showering. Both fully hadronic and semi-leptonic decay modes of top quarks are considered and no filter is applied.

Process		Syntax	Cross section	Percentage
VBFγ + VHγ		p p > h a j j [QCD]@0	55.6 fb	100 %
VHγ	WH	p p > w+ > h a j j [QCD]@0, p p > w− > h a j j [QCD]@0	(2.71 ± 0.06) fb	(4.9 ± 0.2)%
	ZH	p p > z > h a j j@0	(2.16 ± 0.03) fb	(3.90 ± 0.05)%
VBF Hγ	WW fusion	p p > h a j j $$ z w+ w- /z [QCD]@0	(49.0 ± 0.4) fb	(88.1 ± 0.7)%
	ZZ fusion	p p > h a j j $$ z w+ w- /w+ [QCD]@0	(2.36 ± 0.01) fb	(4.20 ± 0.02)%

Table 5.5: Generator-reported cross section at next-to-leading order for each sub-process in the radiative photon production.

Published cross sections are not available for the processes considered here, so the $H\gamma jj$ MADGRAPH 5-reported values are used. These are shown in Table 5.3. For the signal process, an independent cross section calculation was performed using VBFNLO for validation. The VBF-only differential cross section is 51.3 fb for VBFNLO and 51.3 fb for MADGRAPH 5. The VBF + VH cross section of 55.6 fb reported by MADGRAPH 5 is weighted by 92.3%, which is the VBF-only contribution as shown in Table 5.5. The signal process implementation in VBFNLO already excludes the VH

contribution. Comparison of the MadGraph 5 and VBFNLO differential cross sections in the $m_{jj} > 800$ GeV fiducial region is shown in Figure 5.4 as a function of the invariant mass of the quarks not coming from the Higgs decay (VBF jets). Overall, there is good agreement between the MadGraph 5 and VBFNLO calculations.

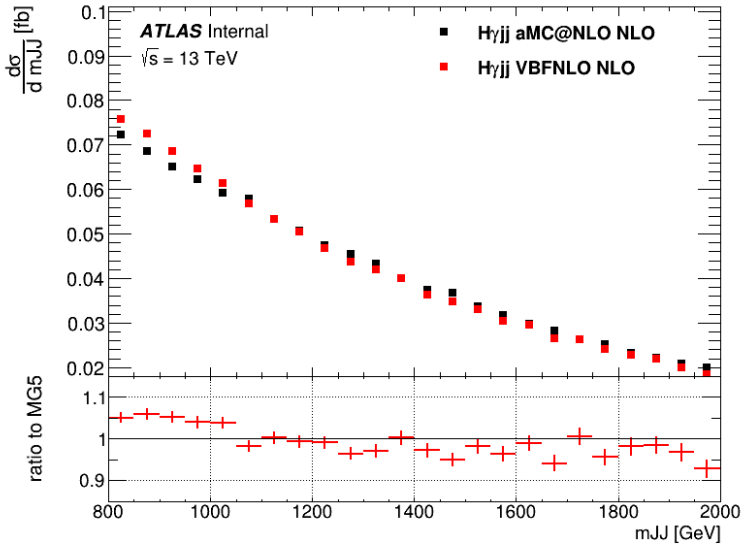

Figure 5.4: Truth-level differential cross section for the signal process as a function of the invariant mass of the VBF jets in the fiducial region.

5.2.2 Background Samples

Using the same MadGraph 5 +Herwig 7 PDFs and parameters as were used to generate signal $H\gamma jj$ NLO Monte Carlo events described above, electroweak $Z\gamma jj$ background Monte Carlo events are generated at NLO with MadGraph 5 v2.9.5 and showered with Herwig v7.1.6. This older version of Herwig 7 was used to avoid Sudakov Factor PDFVeto warnings present in the newest Herwig v7.2. MadSpin is used in this generation to more accurately and efficiently calculate the heavy resonance

Parameter	Description	Value
cut_decays	Apply kinematic cuts on decay products?	F
pdlabel	Use MG5 internal PDFs or LHAPDF interface	lhapdf
lhaid	LHAPDF PDF set ID	93300
maxjetflavor	Max. quark flavor number for applying cuts	5
ptj	Min. jet p_{T}	15.0
ptb	Min. b-jet p_{T}	15.0
pta	Min. photon p_{T}	20.0
etaj	Max. jet η	-1.0
etaa	Max. photon η	3.0
drjj	Min. $\Delta R(jj)$	0.2
drbb	Min. $\Delta R(bb)$	0.2
drbj	Min. $\Delta R(bj)$	0.2
drab	Min. $\Delta R(\gamma b)$	0.2
draj	Min. $\Delta R(\gamma j)$	0.2

Table 5.6: List of event generation parameters used for generating non-resonant LO backgrounds QCD $b\bar{b}\gamma jj$ and $c\bar{c}\gamma jj$.

decay of the Z boson to b-quarks. No QCD couplings are allowed for this electroweak process.

Non-resonant QCD events dominate the background for this analysis. At least two b-jets (c-jets), two additional jets, and a photon make up this $b\bar{b}\gamma jj$ ($c\bar{c}\gamma jj$) background. The QCD $b\bar{b}\gamma jj$ and QCD $c\bar{c}\gamma jj$ samples are generated at LO using MadGraph 5 v2.9.9 and showered using Pythia 8 with AthGeneration 21.6.98. These samples suffer from a low efficiency in the selection phase space, so a 500 GeV m_{JJ} filter is applied. Both of these samples use the PDF set `PDF4LHC21_40_pdfas`. The QCD $b\bar{b}\gamma jj$ sample size increased to 305.9 million events in order to reduce statistical uncertainty, which had a large effect in the previous Run 2 analysis.[97] The QCD $c\bar{c}\gamma jj$ sample is new in the legacy analysis since the fitting strategy now uses a MC template.

The background QCD $Z\gamma jj$ sample was generated at LO using MadGraph 5

Parameter	Description	Value
cut_decays	Apply kinematic cuts on decay products?	F
pdlabel	Use MG5 internal PDFs or LHAPDF interface	lhapdf
lhaid	LHAPDF PDF set ID	90500
maxjetflavor	Max. quark flavor number for applying cuts	5
ptj	Min. jet p_{T}	15.0
ptb	Min. bjet p_{T}	15.0
pta	Min. photon p_{T}	19.0
etaj	Max. jet η	-1.0
etaa	Max. photon η	3.0
drjj	Min. $\Delta R(jj)$	0.2
drbb	Min. $\Delta R(bb)$	0.2
drbj	Min. $\Delta R(bj)$	0.2
drab	Min. $\Delta R(\gamma b)$	0.2
draj	Min. $\Delta R(\gamma j)$	0.2

Table 5.7: List of event generation parameters used for generating LO background QCD $Z\gamma jj$.

v2.3.3 and showered using Pythia 8.

5.2.3 MC Campaigns

The MC samples are produced in three MC campaigns with the mean number of interactions per branch crossing (μ) configured to correspond with the data taking periods 2015-2016, 2017 and 2018. The mean number of interactions per bunch crossing was lowest in 2015, and peaked in 2017. Figure 5.5 shows the μ distribution for data and MC.

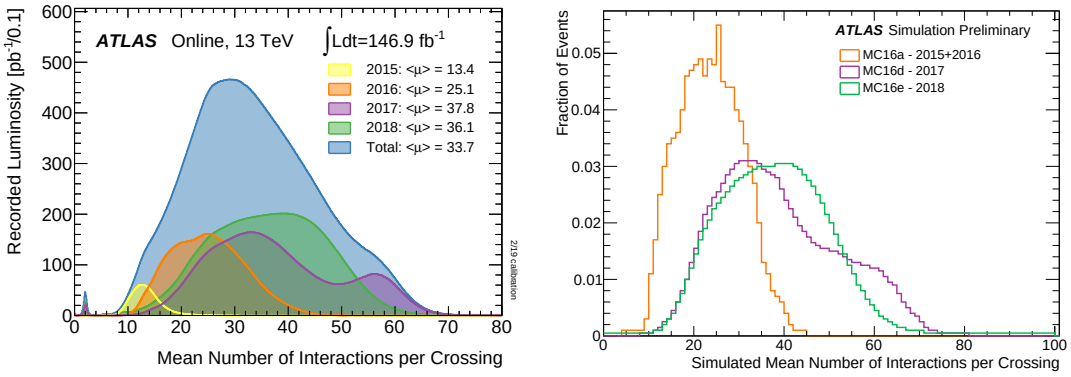

(a) (b)

Figure 5.5: (a) The mean μ distribution during each data taking period from 2015-2018. (b) The mean μ distribution configured for each MC campaign.

Chapter 6

Object Reconstruction and Event Selection

6.1 Physics Object Reconstruction and Selection

This analysis searches for a final state that includes a high-energy photon, two VBF jets, and two b-jets that decayed from the Higgs boson. Cuts on transverse momentum, η, and isolation requirements on these objects target the VBF Higgs plus photon final state.

Although there are no leptons in the final state signal for this analysis, muons and electrons are vetoed for consistency with other Higgs analyses to leave the possibility of including this analysis in future Higgs combination analyses.

Object [%]	p_{T}	$\lvert\eta\rvert$	ID	Isolation
VBF jets	$> 40\,\mathrm{GeV}$	< 4.5		
b-jets	> 40 GeV	< 2.5	DL1r@77% fixed cut WP	
photon	> 30 GeV	$\lvert\eta\rvert < 1.37$ or $1.52 < \lvert\eta\rvert < 2.37$	tight IsEM	FixedCutTightCaloOnly
electron	> 25 GeV	$\lvert\eta\rvert < 2.47$	Tight LLH	FixedCutTight
muon	> 25 GeV	$\lvert\eta\rvert < 1.37$ or $\lvert\eta\rvert < 2.47$	Loose ID	FixedCutTrackOnly

Table 6.1: Object selection requirements for VBF jets, b-jets, photons, and leptons.

6.2 Jets

All four jets for each event in this analysis are required to have $p_T > 40$ GeV due to trigger requirements. The standard recommendation anti-k_t jet clustering algorithm with jet radius R=0.4 is used.[106] The anti-k_t jet clustering algorithm is suggested because it does not modify the shape of the jet when clustering softer jets, and treats all hard jets as circular with a defined radius that may clip parts of nearby clusters from soft jets.[106]

The "Particle flow" jet collection `AntiKt4EMPFlowJets_BTagging201903` was used in the xAOD for this analysis, replacing the older jet collection `AntiKt4EMTopoJets` which used only energy deposits left in the calorimeter to reconstruct jets.[107] Particle flow jets, on the other hand, match energy topo-clusters with the tracks and primary vertex left in both the inner detector and calorimeter, resulting in improved resolution and pile-up stability.[107] Topo-clusters group together the cells where energy is deposited into the EM and hadronic calorimeters by jets, beginning with a "seed" cell that has more than four times the expected noise of the cell and looking at adjacent cells that have at least two times the expected noise. Simulation-based corrections and in-situ techniques are used to calibrate jet energy scale (JES) and jet energy resolution (JER).[108] This

Working Point	JVT Cut	Jet requirements
JVT tight (Default)	> 0.5	($\|\eta\| < 2.4$, $20 < p_{\mathrm{T}} < 60\,\mathrm{GeV}$)
fJVT loose (Default)	< 0.5	($2.5 < \|\eta\| < 4.5$, $20 < p_{\mathrm{T}} < 120\,\mathrm{GeV}$)

Table 6.2: JVT and fJVT working point used in this analysis follow R21 recommendations.[110]

will be further described in Section 9.2.2.

In order to suppress pileup jets, a likelihood-based discriminant called the Jet Vertex Tagger (JVT) is used.[109] The JVT uses tracking information, calculating the fraction of the total momentum of tracks in a jet that are from the primary vertex and keeping a stable hard-scatter jet efficiency independent of the number of vertices.[109] A minimum JVT threshold is set in order to reject pileup jets.

The JVT was validated using $Z \to \mu\mu +$ jets and $t\bar{t}$ data samples, and required jets in the range $20 < p_T < 60$ GeV with $|\eta| < 2.4$.[109, 110] Efficiencies between data and MC agree within 1-2%.[109] The default "tight" working point is used, with the jet requirements shown in Table 6.2.

The fJVT serves the same purpose as the JVT, but is used in the forward region for $2.5 < |\eta| < 4.5$. Jet shapes and topological jet correlations in pile-up interactions are considered for the fJVT, because there is limited track and vertex information in the forward region.[111] For the fJVT, we use the default "loose" setting with a threshold $fJVT < 0.5$ for jets in the range $20 < p_T < 120$ GeV with $2.5 < |\eta| < 4.5$.

To identify jets containing particles originating from heavy-flavor quarks, anti-k_t jet flavor tagging is done on truth-level MC samples. New tagging algorithms optimized in Run 2 utilize recurrent and deep neural networks, resulting in significant improvements

compared to previous jet-flavor identification strategies.[112] The probability of tagging a signal jet is denoted ϵ, while the likelihood of mistakenly identifying a background jet is defined as $1/\epsilon$ and is known as the mis-tagging rate.[112] The flavor tagging efficiencies are shown in Table 6.3 and are obtained from studies on a SM $t\bar{t}$ MC sample.[112]

name	DL1r cut value	b-tag efficiency [%]	c-tag efficiency [%]	l-tag efficiency [%]
FixedCutBEff_77	2.195	78.19	18.35	0.56

Table 6.3: b-tagging, c-tagging, and l-tagging working points used in this analysis, obtained from studies on a SM $t\bar{t}$ MC sample. Efficiencies are reported for the range 20-300 GeV.[113]

6.3 b-tagging

In this $H \to (b\bar{b})$ analysis, the two b-tagged jets are used to reconstruct the Higgs boson in signal events. Thus, correctly identifying the b-tagged jets is essential in order to identify the the signal events. A 77% working point was used for this analysis, corresponding to 77% b-tagging inclusive efficiency in a $t\bar{t}$ sample.[113] This working point choice was constrained by the trigger, as described in Section 5.1.

This legacy analysis replaced the previous MV2c10 b-tagging algorithm with the newest DL1r algorithm, which uses a deep-learning neural network to determine the probability that a jet is a b-jet versus a c or light-jet.[114] The input features that are used take advantage of b-jets' characteristic track impact parameters and reconstructed track vertices in the inner detector.[114] Updating both the PFlowJets and DL1r b-tagging improves the $Z\gamma jj$ mass peak resolution by $(3.2 \pm 0.7)\%$ when using a Breit-Wigner fit, as shown in Appendix E.1.

To calibrate b-jet energies we use the standard jet energy scale calibration, as well as with flavor-specific corrections to improve jet scale and resolution energy measurements.[115] This is an additional constant systematic uncertainty due to different behavior of b-jets compared to light-quarks and gluons in various simulated samples.[116]

Direct tagging versus truth tagging methods are compared, showing only minor shape differences in m_{BB} and $dRBB$ (angular separation between the two leading p_T b-jets) in Appendix E.2. Direct tagging is a binary sorting system that identifies a jet as a b-jet and gives the event an event weight of 1, or identifies a jet as not a b-jet and gives the event a weight of 0, discarding the event. Although direct tagging is more reliable, truth tagging strategies allow for higher statistics. For truth tagging, instead of discarding events that have jets that do not seem "b-jet like," a MC event weight is given a value between 0 and 1 so that events with less b-like jets do not count as much towards the final results. The event weight is based on the number of b-jets, tagging efficiencies, and scale factors. The b-tagging efficiency map used for truth tagging is identical to that used for direct tagging. In this analysis, truth tagging is used for background QCD $b\bar{b}\gamma jj$ and QCD $c\bar{c}\gamma jj$ MC samples to increase statistics, while direct tagging is used for signal $H\gamma jj$ events and other backgrounds.

6.4 Photons

A high-energy photon is also part of the final-state signature, so this analysis adheres to the standard e/γ group recommendations for selecting photons. Photons are

reconstructed offline with dynamic clusters (superclusters) that can vary in radius in order to measure energy from photons emitted during bremsstrahlung or from electron conversions.[117] The algorithm selects clusters of energy deposited into adjacent EM and hadronic calorimeter cells, and then matches them to tracks from the ID, also correcting for bremsstrahlung effects.[117] Position and energy-calibrated superclusters are then matched to tracks and a photon conversion vertex.[117]

Both converted and unconverted photons are included in this analysis. Converted photons are those that produce an electron-positron pair after interacting with the detector material upstream of the calorimeters.[118] Converted photons have a larger opening angle of the electron-positron pair in the magnetic field than that of unconverted photons, but an intrinsic ambiguity still exists in reconstructing an electromagnetic object as an electron or photon.[117]

Photons must have a minimum transverse energy of 30 GeV in this analysis. Photon identification is a cut-based selection according to variables related to shower shape. "Tight" selection is used to make the final photon identification cuts ("medium" and "loose" labels are used for trigger algorithms), and helps pick out prompt photons rather than fake photons. Prompt photons are from hard-scattering events or from fragmentation of a parton, so they are targeted in the analysis. Fake photons, on the other hand, come from any source that reconstructs a photon. This could include jets or decaying hadrons that are reconstructed as photons.[118]

In addition, photon isolation requirements are implemented to reduce contributions of hadronic background, such as jets faking prompt photons. Raw calorimeter

isolation sums the p_T of clusters with a cone $\Delta R = 0.4$ surrounding the photon, and track isolation sums the p_T of tracks surrounding a variable cone size around the photon.[117] In this analysis, the `FixedCutTightCaloOnly` photon isolation working point defined by the fully corrected calorimeter isolation $E_T^{cone40} < 0.022 \times E_T + 2.45$ GeV was followed.[117]

6.5 Electrons and Muons

Electrons are identified from variable-size clusters of energy deposits (superclusters) in the calorimeter that match with at least one track.[117] Electron candidates must satisfy $E_T > 25\,\text{GeV}$, $|\eta| < 2.47$, and the "tight" identification criteria based on tracks and calorimeter deposits in order to separate prompt isolated electrons from hadronic jet energy deposits.[119] The track-based isolation requirement depends on electron p_T and tracks surrounding the electron-associated track within a variable cone size up to $\Delta R = 0.2$, while the calorimeter-based isolation criterion requires the sum of transverse energies of clusters unassociated with an electron candidate within a cone of $\Delta R = 0.2$ around the electron track to be smaller than 3.5 GeV.

Muons are reconstructed by combining the inner detector and muon spectrometer measurements up to $|\eta| = 2.5$.[120] Muon candidates must have $p_T > 25$ GeV and satisfy the "loose" muon identification criteria.[120] The sum of transverse momenta of tracks within a cone of $\Delta R = 0.2$ around the muon track, excluding the muon candidate, must be < 1.25 GeV for the muon candidate to pass the isolation requirements.

Events containing electrons or muons with $p_{\mathrm{T}} > 25$ GeV are vetoed. This is to avoid overlap with other $H(b\bar{b})$ channels, such as WH and ZH, in anticipation of including this channel in a Higgs combination analysis.

6.6 Overlap Removal

Overlap removal follows the ATLAS overlap removal tool guidelines and is performed to prevent double counting of photons, leptons, and jets.[121] Overlap removal is done after kinematic cuts to objects, in the following order: First, any jet within $\Delta R = 0.2$ of an electron is removed, and then any remaining electrons within $\Delta R = 0.4$ of a jet are removed. If a jet has fewer than three tracks associated with it within $\Delta R = 0.2$ of a muon, it is removed. Any remaining muons found within $\Delta R = 0.4$ of a jet are removed. Next, any photon identified within $\Delta R = 0.4$ of an electron or muon is removed. Lastly, all jets that are in the region $\Delta R < 0.4$ of a photon with a minimum transverse momentum of 30 GeV are removed.

6.7 Producing Derived Datasets

The derivation framework performs skimming (removing entire events), thinning (removing entire objects from an event, but leaving the rest of the object), slimming (removing info from object, but leaving the rest of the object), and augmentation (adding auxiliary data) from the full dataset. The derivation HIGG5D3 is used to select events from data and MC for VBF all-hadronic, VBF+γ, and single photons.[122]

HIGG5D3 is a specific derivation of a DxAOD file, which is made from the output of AOD (reconstruction) files or from EVNT (event generation) files, and the variables contained in this file format can be read directly in ROOT.[123] HIGG5D3 files contain containers of reconstructed objects and variables, including analysis-level AntiKt4 jets, flavor tagging, photons, and a record of truth particles.

6.8 Multivariate Analysis Event Selection

Pre-selection cuts are made to select MC and data events of interest from the HIGG5D3 DxAOD files. Signal events are required to pass the trigger requirements listed in Section 5.1 and overlap removal requirements listed in Section 6.6. Signal events must also have two b-tagged jets, two additional VBF jets with a high invariant mass, and a high-energy photon all passing the cuts in Table 6.4. Two jets with a high invariant mass are a signature of VBF signal events, since the VBF jets are the remnants of the two incoming quarks that collided head-on, and which were only slightly deflected when they radiated a W boson or Z boson. The other two Higgs production channels, ggF and VH, are both suppressed in our event selection because they do not pass such a large $m_{JJ} > 800$ GeV cut requirement. The $p_T(b\bar{b})$ cut requires that the vector sum of the pair of b-quarks has a transverse momentum greater than 60 GeV. Data events must also pass the Good Run List (GRL) listed in Section 5.1. Cutflows show the effect of each cut on the number of remaining events, and are presented in Appendix E.3.

The full list of trigger algorithm and offline event selection requirements, before

the event-level DNN classification, is summarized in Table 6.4.

Trigger	L1	≥ 1 photon with $E_{\mathrm{T}} > 22\,\mathrm{GeV}$
	HLT	≥ 1 photon with $E_{\mathrm{T}} > 25\,\mathrm{GeV}$ ≥ 4 anti-k_t jets (or ≥ 3 jets and ≥ 1 b-jet) with $E_{\mathrm{T}} > 35\,\mathrm{GeV}$ and $\lvert\eta\rvert < 4.9$ $m_{jj} > 700\,\mathrm{GeV}$
Offline		≥ 1 photon with $E_{\mathrm{T}} > 30\,\mathrm{GeV}$ and $\lvert\eta\rvert < 1.37$ or $1.52 < \lvert\eta\rvert < 2.37$ ≥ 2 b-jets with $p_{\mathrm{T}} > 40\,\mathrm{GeV}$ and $\lvert\eta\rvert < 2.5$ ≥ 2 additional jets with $p_{\mathrm{T}} > 40\,\mathrm{GeV}$ and $\lvert\eta\rvert < 4.5$ $m_{jj} > 800\,\mathrm{GeV}$ $p_{\mathrm{T}}(b\bar{b}) > 60\,\mathrm{GeV}$ No electrons with $p_{\mathrm{T}} > 25\,\mathrm{GeV}$ or muons with $p_{\mathrm{T}} > 27\,\mathrm{GeV}$

Table 6.4: Trigger and offline event selection criteria for the $H(\rightarrow b\bar{b})jj + \gamma$ signature. L1 and HLT refer to the first-level trigger and the high-level trigger, respectively. The p_{T} and $|\eta|$ offline jet requirements are used to match trigger selections and b-tagging requirements.

6.9 Data versus Monte Carlo Comparison

After choosing events based on the event selection criteria, differences in kinematic distributions between signal $H\gamma jj$ versus background QCD $b\bar{b}\gamma jj$ and $c\bar{c}\gamma jj$ help identify signal and background events. The 9 kinematic variables chosen are described below, while the reasons for choosing these variables in particular are explained in Section 7.2:

1. m_{bb}: The invariant mass of two leading b-jets–m_{bb} is peaked at the Higgs mass for signal $H\gamma jj$ and is a flatter, falling distribution for the QCD background
2. $p_{\mathrm{T}}^{\mathrm{balance}}$: transverse momentum balance for selected final state objects–$p_{\mathrm{T}}^{\mathrm{balance}}$ is higher for QCD $b\bar{b}\gamma jj$ because the jets are not as far forward as VBF jets

$$p_{\mathrm{T}}^{\mathrm{balance}} = \frac{|\vec{p_{\mathrm{T}}}^{b1} + \vec{p_{\mathrm{T}}}^{b2} + \vec{p_{\mathrm{T}}}^{j1} + \vec{p_{\mathrm{T}}}^{j2} + \vec{p_{\mathrm{T}}}^{\gamma}|}{p_{\mathrm{T}}^{b1} + p_{\mathrm{T}}^{b2} + p_{\mathrm{T}}^{j1} + p_{\mathrm{T}}^{j2} + p_{\mathrm{T}}^{\gamma}} \tag{6.1}$$

3. (z^*_{j3}): The Zeppenfeld variable, defined as the centrality of the third jet relative to the first and second jet[124]

$$z^*_{j3} = \frac{\left| y_{j3} - \frac{y_{j1}+y_{j2}}{2} \right|}{|y_{j1} - y_{j2}|} \tag{6.2}$$

   z_{j3} is lower for background QCD $b\bar{b}\gamma jj$ because the 3rd jet is more likely to be from gluon emissions

4. nJets: The total number of resolved jets in the event–nJets is greater for the background QCD $b\bar{b}\gamma jj$ sample because of QCD gluon emissions

5. $\Delta\eta(j,j)$: η difference between two VBF jets–$\Delta\eta(j,j)$ is slightly higher for the signal because the VBF jets have large separation

6. $mindRBPh$: The minimum angular distance between one of the b-jets and the photon–$mindRBPh$ is slightly lower for the QCD $b\bar{b}\gamma jj$ sample because photons can radiate off the b-jets

7. m_{jj}: the invariant mass of two VBF jets–high m_{jj} is a signature for VBF processes because the VBF jets are the remnants of the pair of incoming quarks that only slightly deflected when they radiated a W or Z boson

8. $\Delta\eta(b,b)$: η difference between two b-jets–$\Delta\eta(b,b)$ is lower for the signal $H\gamma jj$ because the b-quarks are close to each other as they decay from the Higgs boson

9. $etaJ5$: η of a 5th jet (2 b-jets, 2 VBF jets, plus this extra 5th jet. Also called the 3rd jet in z_{j3} because it is the third non b-tagged jet)–The absolute value of etaJ5 is lower for background QCD $b\bar{b}\gamma jj$ because the 5th jet is more likely to be from gluon emissions

Data and Monte Carlo kinematic distributions agree relatively well, as shown in Figure 6.1. However, discrepancies exist between data and MC especially for $nJets$, $mindRBPh$, $dEtaJJ$, and mBB, as was the case for the previous Full Run 2 Analysis. Although the source of the discrepancies was investigated, nothing specific was identified as the cause.

To improve data to MC agreement, reweighting is performed on the Monte Carlo kinematic variables. To perform reweighting, the ratio of QCD $b\bar{b}\gamma jj + c\bar{c}\gamma jj$ MC

to data for each variable is taken in each bin in the m_{BB} sidebands and then a function is fit to that MC/data ratio plot as shown in Figure 6.2. The function is then applied to the MC in order to scale points to better match data. Only the two QCD backgrounds are used to reweight the MC because together they make up more than 99.5% of the MC background, as shown in Table 9.3. This procedure is applied to $nJets$, $mindRBPh$, $dEtaJJ$, and mBB, in that order. Subsequent variables include the reweighting effects from the previous variable, and affect the other kinematic distributions as shown in Figure 6.3. The reweighting functions are:

- nJets: $4.66422583 - 1.40117372x + 0.16286083x^2 - 0.00571402x^3$
- mindRBPh: $0.19278366 + 0.99099218x - 0.32211585x^2 + 0.03152718x^3$
- dEtaJJ: $0.861711461 + 2.95481808e^{-21243.1601x-(1.06962181e+09)x^2}$
- mBB: $0.89769523 + 1.75470347e^{-40.07675357x+0.09381659}$

The effects of kinematic reweighting on DNN output will be discussed further in Chapter 9.1.5.

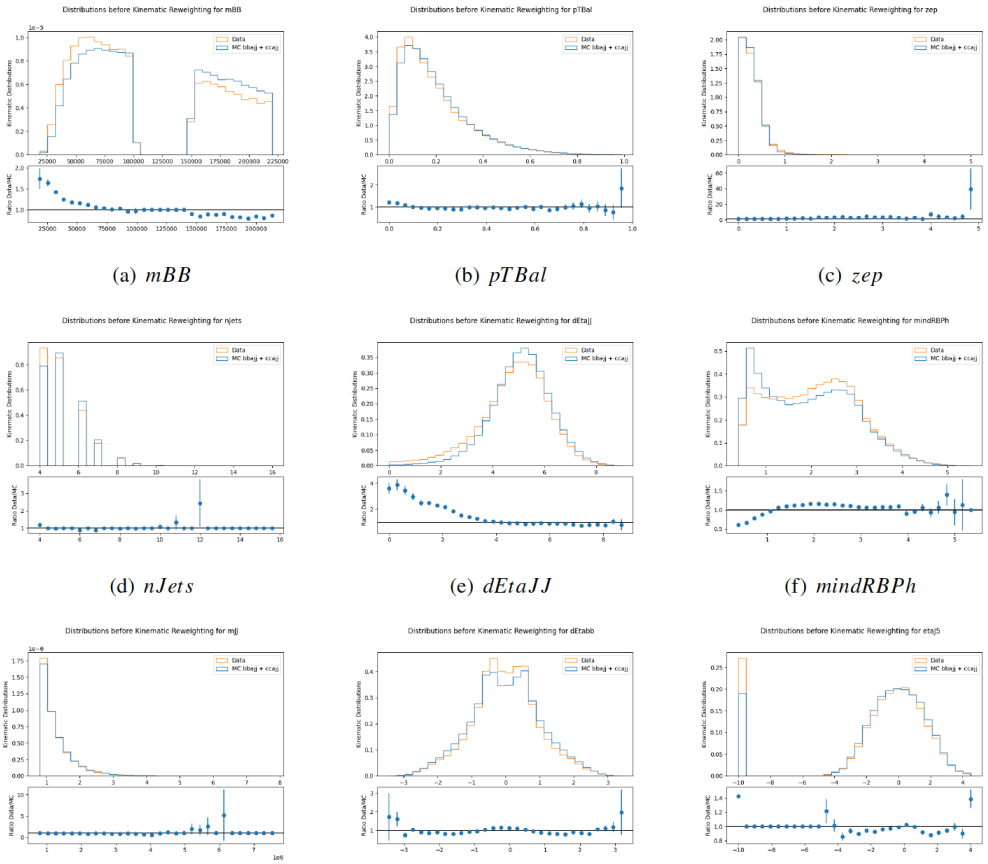

(a) *mBB* (b) *pTBal* (c) *zep*

(d) *nJets* (e) *dEtaJJ* (f) *mindRBPh*

(g) *mJJ* (h) *dEtabb* (i) *etaJ5*

Figure 6.1: Monte Carlo versus data comparison for all kinematic variable inputs to the DNN. *nJets*, *mindRBPh*, *dEtaJJ*, and *mBB* were chosen for reweighting because MC and data are visible in these distributions, and they have strong correlations with other variables that show some discrepancies, such as *dEtabb* and *pTBal*.

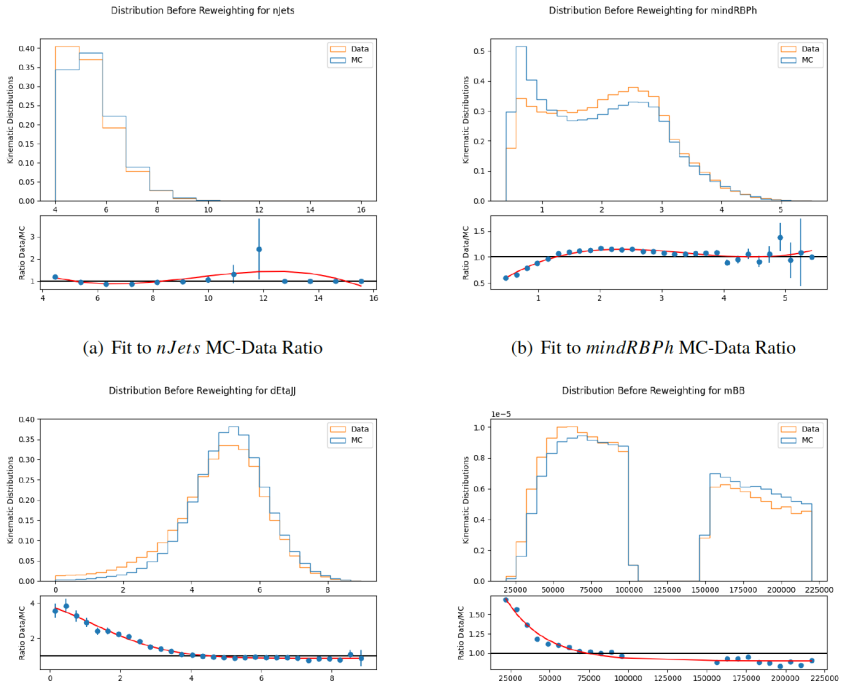

(a) Fit to $nJets$ MC-Data Ratio

(b) Fit to $mindRBPh$ MC-Data Ratio

(c) Fit to $dEtaJJ$ MC-Data Ratio

(d) Fit to mBB MC-Data Ratio

Figure 6.2: Fits of Analytic Functions to ratio plots of kinematic distributions between data and Monte Carlo $b\bar{b}\gamma jj + c\bar{c}\gamma jj$. These analytic functions are applied to reweight Monte Carlo $b\bar{b}\gamma jj + c\bar{c}\gamma jj$ in all regions for better Data-MC Agreement.

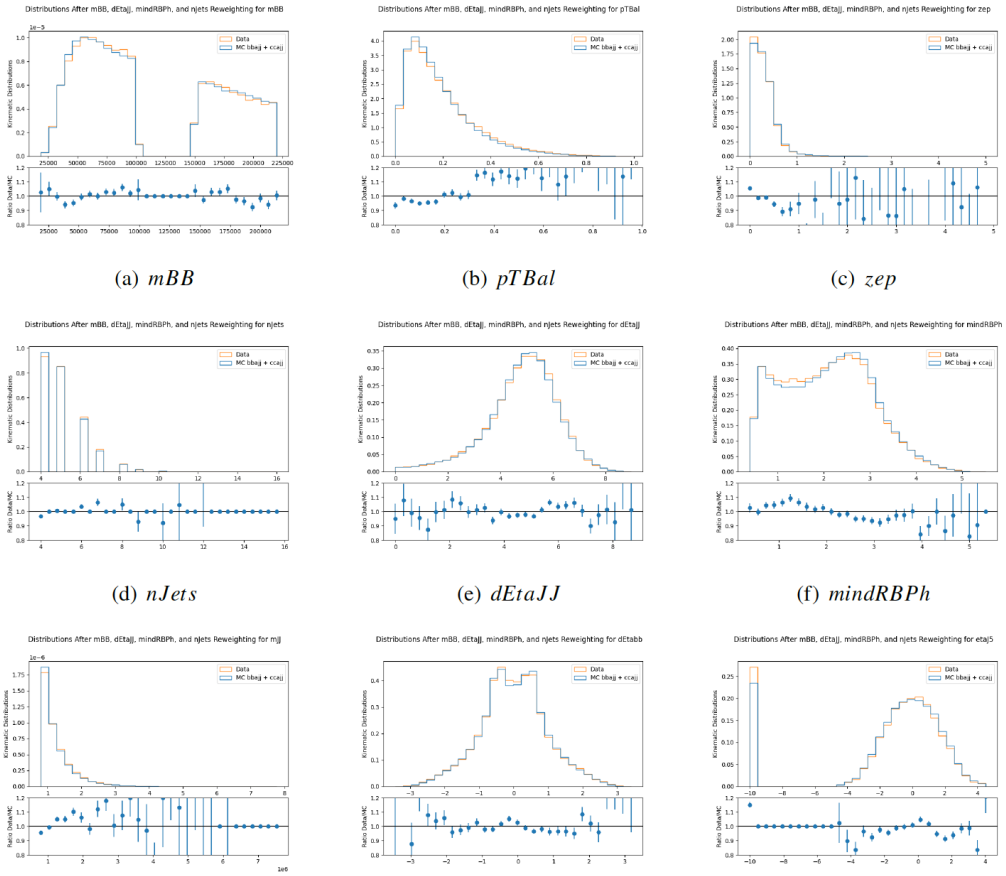

(a) mBB (b) $pTBal$ (c) zep

(d) $nJets$ (e) $dEtaJJ$ (f) $mindRBPh$

(g) mJJ (h) $dEtabb$ (i) $etaJ5$

Figure 6.3: Monte Carlo kinematic variables after kinematic reweighting to better match data. The variables shown are those that are input into the MVA. The reweighting variables were $nJets$, $mindRBPh$, $dEtaJJ$, and mBB.

Chapter 7

Multivariate Analysis

7.1 Dense Neural Network Training and Optimization

A dense neural network (DNN) replaces the Boosted Decision Tree (BDT) used in the previous Full Run 2 analysis because preliminary studies showed improvement in signal significance using a DNN. The Keras high-level API of TensorFlow is used to train the neural network to distinguish between MC signal $H\gamma jj$ and background non-resonant QCD $b\bar{b}\gamma jj$ events.[125, 126] 71% (380,996) of events are used for training the model. 9% (50,000) of events are used for validation to unbiasedly tune the hyperparameters while avoiding directly affecting the DNN model. The remaining 20% (107,749) of the MC sample is used for testing and evaluating the model. The background QCD $b\bar{b}\gamma jj$ training input sample is limited to 250,000 events, which is about half of the total number of events used for training. Signal and background training samples that are close in size lead to better separation between signal and background in the DNN output, and

prevents overtraining of the background QCD $b\bar{b}\gamma jj$ sample relative to the signal $H\gamma jj$ sample.

A 'sparse_categorical_crossentropy' loss function is minimized in the training to compare the label and prediction output values. The 'sparse_categorical_crossentropy' loss function saves memory space and gives the most-likely classification labels as integers, rather than the "one-hot" array representation used by 'categorical_crossentropy.' Cross-entropy loss models punish the model based on the confidence of predictions.The network is trained with supervised learning to give an output score between 0 and 1, evaluating each event on how signal-like (1) or background-like (0) it is. Event weights are applied after training to the DNN output score.

Hyperparameters of the training, such as the number of hidden layers, number of training epochs, and number of neurons per layer, are optimized by re-running the training with varied parameters and ranking the training performances using a number counting significance estimate. For events with only four jets, the Zeppenfeld variable $zj3$ and $etaJ5$ are undefined, so a random value from the corresponding kinematic distribution of 5+ jet events was chosen. Choosing random values for the non-existent 5th jet in 4-jet events maintains the overall $zj3$ and $etaJ5$ kinematic distributions in order use the event while minimizing altering the DNN training.

The selected DNN hyperparameters from this optimization process are summarized in Table 7.1. Training ends when Δ"val_loss"< 0.001 for 5 epochs in order to avoid overtraining. This also speeds up the training so that it only takes about 5 minutes using a single GPU. The loss curve as a function of epoch shown in Figure 7.1 decreases

Hyperparameter	Value for Neural Net Training
Number of Hidden Layers	11
Number of Neurons per Layer in Bulk	256
Activation Function in Bulk	Rectified Linear Unit
Hidden Layer Activation Function	Softsign
Activation Function in Output Layer	SoftMax
Number of Neurons in Output Layer	1
Loss Function	sparse_categorical_crossentropy
Number of Training Epochs	Until Δ"val_loss" < 0.001 for 5 epochs
Batch Size	256
Learning Rate	$1e-3$

Table 7.1: Training Parameters for the deep neural network classifier.

consistently and flattens out at higher epochs, showing that the model is training until adding additional epochs does not significantly decrease the loss any further. Figure 7.2 also shows that the efficiency for identifying signal events (signal efficiency) is high at high NN scores and the rate for rejecting background events (background rejection) is high at low NN scores, as is desirable.

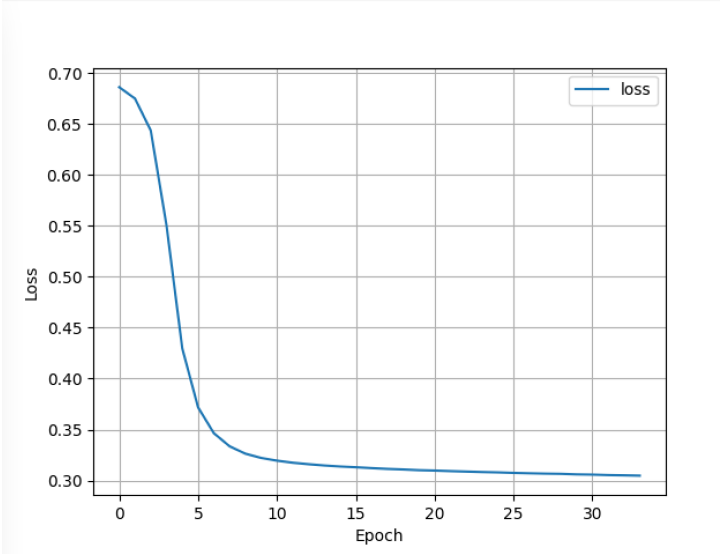

Figure 7.1: The loss curve as a function of epochs shows that the DNN is trained well until adding additional epochs does not significantly decrease the loss any further.

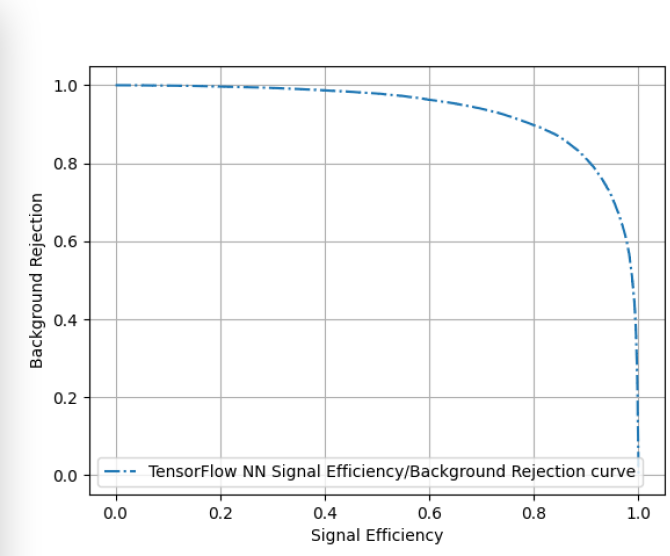

Figure 7.2: The signal efficiency is high at high NN scores and background rejection is high at low NN scores.

The output from the DNN training and testing is plotted in Figure 7.3. There is good separation between signal (S) and background (B), and also good agreement between the testing (dots) and training (solid histogram) samples, showing that the model is not overtrained.

7.2 Input Variables

Using the signal VBF $H\gamma jj$ and background QCD $b\bar{b}\gamma jj$ MC samples in the phase spaces described in Table 7.2, input variables for the DNN are optimized by checking the total number counting significance estimate after each variable is added one at a time. The significance estimate is calculated by binning the neural net output score distribution into 20 equal bins, computing the number of signal events divided by the square root of the number of background events ($S/\sqrt{B}$) in each bin, and summing

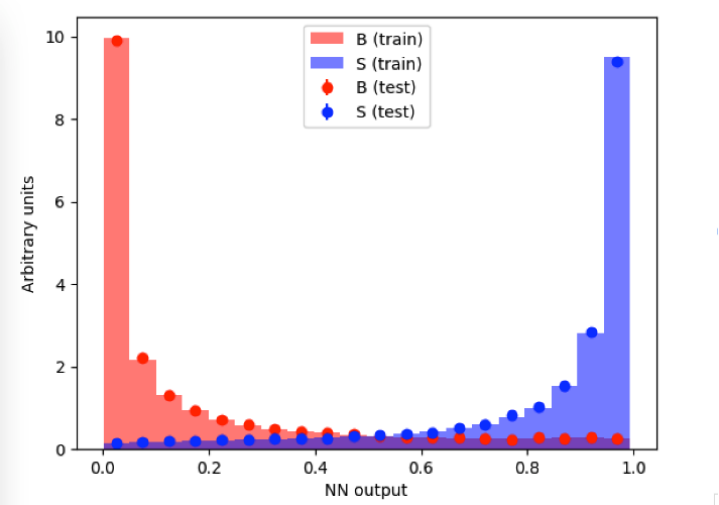

Figure 7.3: DNN output scores for training and test samples show good separation between signal (S) and background (B).

the significance results in each bin in quadrature.

The variable with the highest significance in a 1-input NN is chosen first, and then each remaining variable is added individually to check which additional variable increases the significance the most as the second variable. This loop process then continues to choose the third, fourth, etc. variable that increases the significance the most. Once adding a new variable fails to increase the total significance, the optimization is stopped.

Nearly 30 kinematic variables are tested. The 9 kinematic variables chosen after optimizing, in order from most to least powerful, are as follows (Definitions of each variable are in Section 6.9):

1. m_{bb}
2. $p_{\mathrm{T}}^{\mathrm{balance}}$

Variable Name	Phase Space Used in Training
mBB	mBB $\leq$ 220 GeV
pTBal	$0 \leq$ pTBal ≤ 1
zep	zep > 0
nJets	nJets ≥ 4
dEtaJJ	$0 <$ dEtaJJ < 9
mindRBPh	$0.4 \leq$ mindRBPh < 6
mJJ	mJJ $\geq$ 800 GeV
dEtabb	-3.5 $\leq$ dEtabb $\leq$ 3.5
etaJ5	-4.5 $\leq$ etaJ5 $\leq$ 4.5

Table 7.2: Phase spaces of variables used as input features to the Dense Neural Net classifier.

3. z^*_{j3}
4. $nJets$
5. $\Delta\eta(j,j)$
6. $mindRBPh$
7. m_{jj}
8. $\Delta\eta(b,b)$
9. $etaJ5$

The significance after adding each of the 9 optimized variables is shown in Figure 7.4.

After training, validating, and testing the DNN model with the signal and QCD $b\bar{b}\gamma jj$ background MC samples, the DNN is used to evaluate the other background MC samples and data. This will be described in Chapter 8.

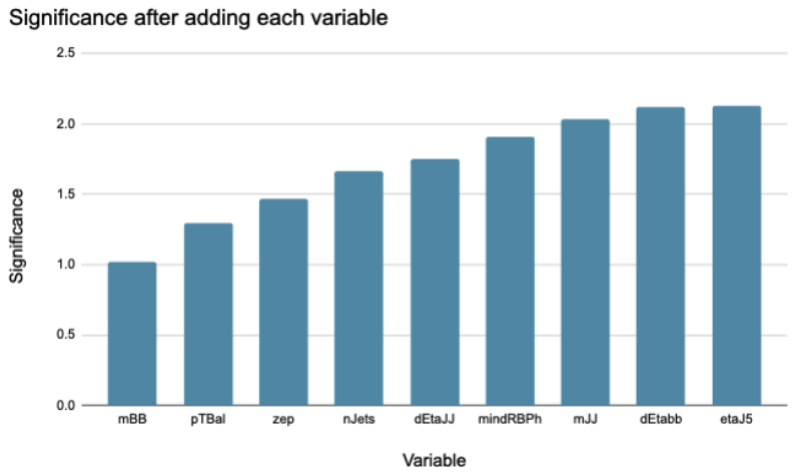

Figure 7.4: The calculated significance after adding each variable to the DNN, until adding more variables no longer increases the significance.

Chapter 8

Signal and Background Modeling

8.1 Fitting Strategy

The previous Full Run 2 analysis extracted the Higgs signal contribution in a fit to m_{bb} data, but changing the strategy to fit to DNN output significantly improves the signal significance calculation in this legacy analysis.[97] The DNN output is fit with a binned template profile likelihood using the `TRExFitter` framework.[127] The signal and control region definitions are based on m_{bb}. The signal region includes the Higgs mass window $100 < m_{bb} < 150$ GeV and accounts for about 80% of the signal. A control region using the m_{bb} sidebands (50-100 GeV and 150-220 GeV) is used to extract a background normalization in the fit. Events with m_{bb} below 50 GeV and above 220 GeV are excluded because they are unlikely to be from a Higgs boson decay and including those regions decreases the estimated signal significance.

Background QCD $b\bar{b}\gamma jj$ and signal $H\gamma jj$ templates are taken from Monte

Carlo due to higher available statistics compared to data. About 300 million QCD $b\bar{b}\gamma jj$ background MC events are generated, which is about 28 times the data statistics available in 132 fb^{-1}. Use of this large MC sample greatly reduces statistical uncertainty in the background template.

8.2 Background Sources

Although the dominant background is QCD $b\bar{b}\gamma jj$, the fit templates include several background sources. Events contributing to the final signal region have at least four jets, with at least two jets b-tagged with the 77% tagging working point selection, and a photon in the final state. The main backgrounds are categorized into two groups depending on whether the process has heavy resonances. Cross sections for these backgrounds are shown in Table 5.3.

Resonant background

- $Z + \gamma$+jets: A non-negligible number of EWK $Z \to b\bar{b}$ events contribute to the final signal region and mimic the Higgs boson signal in all ways except for the invariant mass. This background forms a peak in the signal region m_{bb} distribution at $m_{bb} \approx m_Z$. In addition to $Z \to b\bar{b}$, events from $Z \to c\bar{c}$ and $Z \to$ light-quarks can also contribute to the signal region due to b-tagging misidentification, though these contributions are small because of a high rejection rate for c and light-jets using the DL1r tagger with 77% WP.[113] QCD $Z \to b\bar{b}$ events do not contribute to the final signal region because they do not cause a peak in m_{bb}. Both EWK and

QCD $Z \to b\bar{b}$ samples are evaluated using the DNN and included in the final fit.

- $W+\gamma$+jets: Events from $W+\gamma$+jets with $W \to q\bar{q}$ contribute to the signal region due to b-jet misidentification. The contribution is expected to be small because of the following estimates:
  - $BR(W \to cl) \sim 30\%$, $\epsilon_{\text{tag}}(c) \sim 18.35\%$, $\epsilon_{\text{tag}}(l) \sim 1\%$ for 77% b-tagging efficiency WP with DL1r tagger.[113]
  - $BR(Z \to b\bar{b}) \sim 15\%$, $\epsilon_{\text{tag}}(b) \sim 78.19\%$.[41, 113]
  - The ratio between $W+\gamma$ and $Z+\gamma$ contributions are calculated as:

$$\frac{N(W+\gamma)}{N(Z+\gamma)} = \frac{BR(W \to cl) \times \epsilon_{\text{tag}}(c) \times \epsilon_{\text{tag}}(l) \times \sigma(W+\gamma)}{BR(Z \to b\bar{b}) \times \epsilon_{\text{tag}}(b) \times \epsilon_{\text{tag}}(b) \times \sigma(Z+\gamma)} = 0.0034 \times \frac{\sigma(W+\gamma)}{\sigma(Z+\gamma)} \tag{8.1}$$

  - By considering the cross section ratio, $\frac{\sigma(W+\gamma)}{\sigma(Z+\gamma)}$, which is roughly 3 for electroweak production, the contribution from the $W+\gamma$ process is found to be only about 1.0% of that from $Z+\gamma$, so it is ignored in this analysis.

Non-resonant background

- QCD multi-jet production with b-quarks in association with a photon: This is the main background source with a large production cross section of 674.9 pb even in a restricted phase space. It accounts for about 79.6% of the total background. Generated MC samples with full detector simulation are used for event selection optimization, kinematic reweighting, training the DNN, and templates.

- QCD multi-jet production with c-quarks in association with a photon: The contribution from QCD multi-jet production from c-quarks in association with a photon is about 19.9% of the total background. Kinematics are similar to those of the $b\bar{b}\gamma jj$, but the m_{cc} distribution is shifted slightly higher and ΔR between the photon and leading flavor-tagged jet distributions are slightly lower because the photon is more likely to radiate off the c-jets due to the charge. Differences in the kinematic distributions can be seen in Appendix F. A new $c\bar{c}\gamma jj$ MC sample was generated for this legacy analysis as described in Section 5.2.2. It is used for kinematic reweighting and evaluating on the DNN, and is included in the final fit.

- QCD multi-jet production with light-quarks in association with a photon: Although the 2.7×10^4 pb cross section of light-jets is large, the contribution from light-jets is very small because of the high rejection rate from the b-tagger. The QCD light-jet contribution is estimated with the following considerations:

  - $\epsilon_{\text{tag}}(l) < 1\%$, for 77% b-tagging efficiency WP with DL1r tagger for jets with transverse momentum from 20-300 GeV.[113]
  - $\epsilon_{\text{tag}}(b) \sim 78.19\%$ for jets in the same momentum range.[113]
  - The ratio between $b\bar{b} + \gamma + jets$ and $l\bar{l} + \gamma + jets$ contributions is calculated as:

$$\frac{N(l\bar{l}\gamma jj)}{N(b\bar{b}\gamma jj)} = \frac{\epsilon_{\text{tag}}(l) \times \epsilon_{\text{tag}}(l) \times \sigma(l\bar{l}\gamma jj)}{\epsilon_{\text{tag}}(b) \times \epsilon_{\text{tag}}(b) \times \sigma(b\bar{b}\gamma jj)} = 0.00016 \times \frac{\sigma(l\bar{l}\gamma jj)}{\sigma(b\bar{b}\gamma jj)} \tag{8.2}$$

Therefore, the non-resonant QCD $l\bar{l}\gamma jj$ process contributes $< 0.5\%$ and MC is not produced for this contribution.

- $t\bar{t}H + \gamma$, $tH + \gamma$, and ggH processes: The cross sections for these processes are very small compared to other backgrounds. $t\bar{t}H$ and ggH MC samples are considered in the fit but have minimal effects.

- $b\bar{b}\gamma j$: The cross section is 897.3 pb, but this process is accounted for in the QCD $b\bar{b}\gamma jj$ matrix element of MadGraph 5 so a separate MC sample is not produced for this contribution.

- $b\bar{b}jj$: Only an estimated 5-10% of jets fake photons, so a separate MC sample is not produced for this contribution.[128]

Only the QCD $b\bar{b}\gamma jj$ MC sample is used for training the DNN. Along with the QCD $b\bar{b}\gamma jj$ MC sample, the QCD $c\bar{c}\gamma jj$, $Z\gamma jj$, $t\bar{t}H$, and ggH MC samples are evaluated with the DNN and are included in the final fits.

8.3 MC Validation

We start by checking the control region for the MC DNN output outside the signal m_{bb} window region in order to check how well our MC matches the data in a background-rich region without much contribution from our Higgs boson signal. Validating the m_{bb} sideband region first helps ensure that we do not create a biased VBF $H + \gamma$ model in the region where we expect to find a majority of Higgs bosons. The DNN

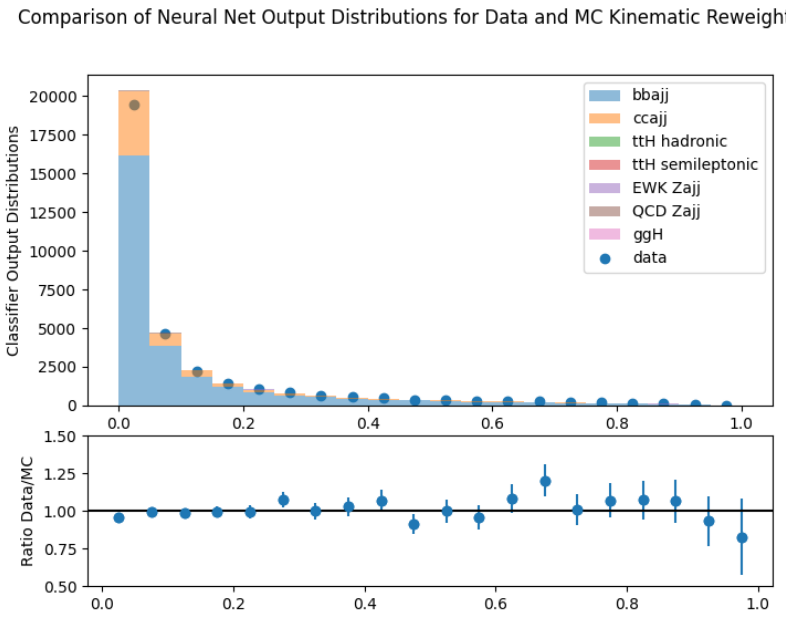

Figure 8.1: MC versus data comparison of the NN output in the m_{bb} sideband region.

output after evaluation on data and all background MC samples in the m_{bb} sideband regions is presented in Figure 8.1. MC and data show agreement within uncertainties. This excellent agreement between data and MC in the sideband m_{bb} region suggests that the MC template is well-modeled and reliable in the VBF Higgs phase space.

An additional ABCD method check is done to confirm that MC agrees with data. This check is done as validation only, and is neither used for fitting nor does it lead to additional uncertainties. This ABCD method check aims to compare the m_{bb} window MC with predicted data in the m_{bb} signal region. This is done by transferring the sideband data to validate the m_{bb} window signal region MC, using the ABCD method with the sideband and window regions defined in Section 8.1. Since the ratio A/C = B/D, then $A = \frac{B}{D}C$ as shown in Figure 8.2.

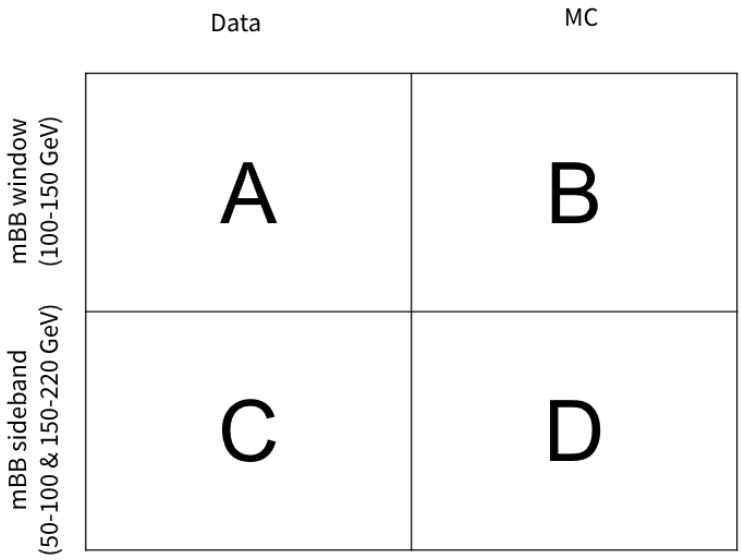

Figure 8.2: The ABCD method regions used to transfer the sideband data to validate the m_{bb} window MC.

Only the dominant backgrounds, represented by the QCD $b\bar{b}\gamma jj$ and $c\bar{c}\gamma jj$ MC samples, are considered here. They comprise more than 99.5% of the total background. First, the DNN output for the MC in the m_{bb} window signal region is compared with that of the m_{bb} sideband region, and a MC-to-MC transfer function is extracted by fitting the points from the ratio of the two regions in each bin as shown in Figure 8.3.

Next, the transfer function extracted from Figure 8.3 is applied to the data in the m_{bb} sideband control region, as shown in Figure 8.4. It is evident that the transferred m_{bb} sideband control region data matches the m_{bb} window signal region MC within uncertainties. This is expected since the data m_{bb} window region (A) should be equivalent to the MC window region over the MC sideband region (B/D) multiplied by the data sideband region (C), and MC and data should match in the m_{bb} window signal

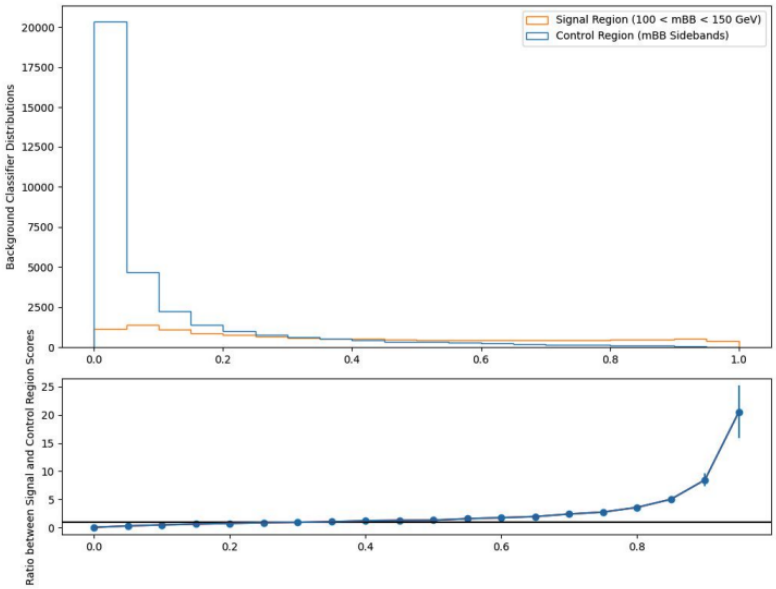

Figure 8.3: The DNN output for the m_{bb} signal region versus DNN output for m_{bb} sidebands for $b\bar{b}\gamma jj$ and $c\bar{c}\gamma jj$ MC. The transfer function is taken from the ratio plot on the bottom.

region. Since these validation checks show that MC template reliably models the data in the VBF Higgs phase space, no additional non-closure uncertainty is necessary.

8.4 Fitting to DNN Output

A binned profile maximum likelihood fit of the DNN output score MC template is used in this analysis, with 20 signal region bins and 20 control region bins. A binned strategy is pursued because the DNN output score shape does not have an anticipated functional form. The binned likelihood approach is based on Poisson statistics and depends on the sum product of the signal yield N_S, background yield N_B, and observed yields in each bin n_i according to:

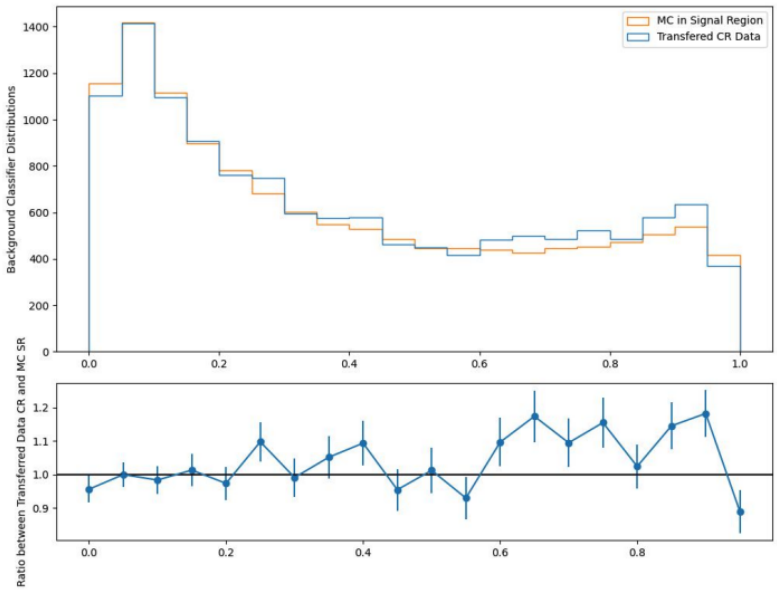

Figure 8.4: The transferred m_{bb} sideband control region data are used to estimate the data m_{bb} signal region distribution. The result matches the MC m_{bb} signal region within uncertainties as expected.

$$L(N_S, N_B; \{n_i\}_{i=1...n_{bins}}) = \prod_{i=1}^{n_{bins}} e^{-N_S s_i + N_B b_i} \frac{(N_S s_i + N_B b_i)^{n_i}}{n_i!}$$

where s_i is the fraction of signal in each bin and b_i is the fraction of background in each bin.[129] The single parameter of interest (POI) for this analysis is the signal strength μ_H, which describes the measured $H\gamma jj$ signal cross section relative to SM-predicted cross section. The POI μ_H is set to maximize the likelihood by minimizing the negative log likelihood $-2\log(L)$. Systematic uncertainties in the likelihood are included with

the profile likelihood approach and constrain nuisance parameters (NPs). Relevant theoretical and experimental systematic uncertainties for this analysis will be discussed in Chapter 9.

The likelihood including systematics is:

$$L(\mu, \theta; data) = L_{\text{measurement}}(\mu, \theta, data)C(\theta) \tag{8.4}$$

where μ is the POI, θ is the systematics NP, $L_{\text{measurement}}$ is the measurement likelihood, and $C(\theta)$ is the NP external constraint term.[129]

The signal and control regions are based on the m_{bb} sidebands and window defined in Section 8.1, and they are analyzed simultaneously to model any correlations between the two regions. The sideband control region is needed for background normalization in the fit in this analysis. The maximum likelihood signal strength μ_H at 95% confidence-level is expected to be consistent with 1 if the data are consistent with the SM Higgs hypothesis.

Chapter 9

Statistical Interpretation and Results

9.1 Theory Systematic Uncertainties

9.1.1 Theory Systematic from the H$\rightarrow b\bar{b}$ Branching Ratio

The H$\rightarrow b\bar{b}$ branching ratio and its uncertainty is provided by the LHC Higgs Cross section working group for the SM Higgs near 125 GeV, as shown in Table 9.1.[44] The branching ratio is calculated from the full set of partial widths, and both theoretical uncertainties and parametric (experimental input) uncertainties are included in the calculations.[44] An overall uncertainty of 1.3% on the signal cross section is considered in the analysis.

9.1.2 Theory Systematic due to QCD Scale Choice

Uncertainties on the QCD $b\bar{b}\gamma jj$ and $c\bar{c}\gamma jj$ background shape based on the choice of μ_R (Renormalization scale) and μ_F (Factorization scale) are evaluated by

m_H	BR	THU(%)		PU(m_q)(%)		PU(α_s)(%)	
125.09 GeV	0.5809	+0.65	-0.65	+0.72	-0.74	+0.77	-0.79

Table 9.1: Uncertainties on the branching ratio for the H→ $b\bar{b}$ decay provided by the LHC Higgs Cross section working group.[44]. Theoretical uncertainties (THU) originate from missing higher orders in the calculations. Parametric uncertainties (PU) account for the experimental errors on SM input parameters related to quark masses (m_q)and the strong coupling constant (α_s).

varying each parameter independently by scales of 0.5, 1.0, and 2.0. These variations were stored during MadGraph 5 event generation and were evaluated using the 7-point scale variation as suggested by the PMG recommendations.[130] According to this envelope method, we eliminate the two off-diagonal variations ({μ_R, μ_F}×{0.5, 2.0}, {2.0, 0.5}) and take the highest variation among ({μ_R, μ_F}×{0.5, 0.5}, {1.0, 0.5}, {0.5, 1.0}, {1.0, 1.0}, {1.0, 2.0}, {2.0, 1.0}, {2.0, 2.0}) as our QCD scale uncertainty.

Each systematic variation is evaluated using the DNN that was trained with the QCD $b\bar{b}\gamma jj$ and $c\bar{c}\gamma jj$ MC samples. The μ_R and μ_F systematics have a small impact on the background shape, contributing $< 1\%$ uncertainty on the signal significance. The effect from μ_R and μ_F variations on DNN output are shown in Figure 9.1.

9.1.3 Theory Systematic due to PDF and α_s Choice

Uncertainties due to the choice of PDF+α_s are evaluated by the event generator using PDF reweighting [131]. On-the-fly weights are stored during event generation with MadGraph 5 for 43 error members of the PDF set `PDF4LHC21_40_pdfas`.[132] Member 0 is the nominal, while members 1-40 are PDF variations $\alpha_s(m_Z^2) = 0.118$ and members 41-42 are α_s variations for $\alpha_s(m_Z^2) = 0.117$ and $\alpha_s(m_Z^2) = 0.119$, respectively.

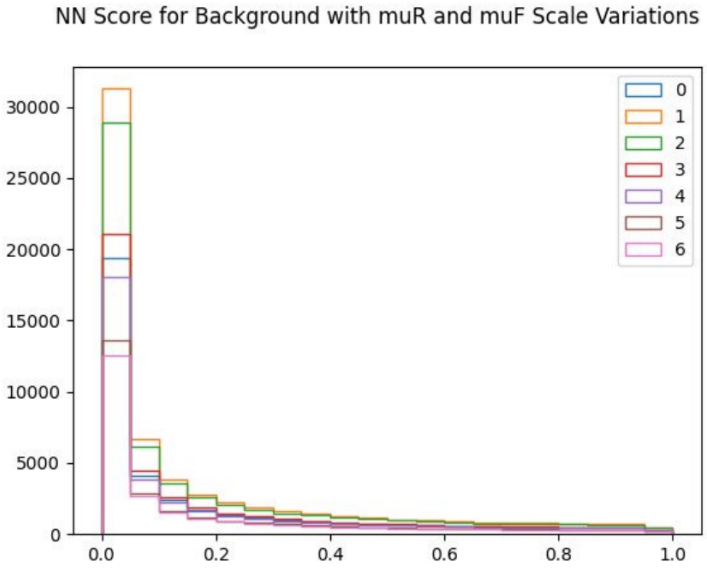

Figure 9.1: The μ_R and μ_F variations on DNN output of the QCD $b\bar{b}\gamma jj$ MC sample in the control and signal regions. The 7 variations are from varying each parameter independently by scales of 0.5, 1.0, and 2.0 and removing the off-diagonal 0.5 and 2.0 combinations.

HardScaleFactor	Acceptance
0.5	2.79%
1.0 (no scaling)	2.81%
2.0	2.88%

Table 9.2: Acceptance as HardScaleFactor is varied. Comparing the Hard Scale Factors of 0.5 and 2.0 from 300,000 generated events, the relative acceptance uncertainty is 3.1%.

Each systematic variation is evaluated using the DNN that was trained with the QCD $b\bar{b}\gamma jj$ and $c\bar{c}\gamma jj$ MC samples. The uncertainty on the signal cross section is 2.2% while the uncertainty on the signal significance is about 1% considering PDF, α_s, and μ_R/μ_F uncertainties.

9.1.4 Parton Shower Theory Systematic

The signal next-to-leading-order MC samples in this analysis use the Herwig 7 defaults of `H7-PS-MMHT2014LO` for the parton shower tune, and `H7-UE-MMHT` for the underlying event tune. Following the Physics Modeling Group recommendations, the theory uncertainties on the parton shower are studied within a single shower program by varying the "HardScaleFactor." This changes the maximum allowed transverse momentum for shower emissions to $p_{\mathrm{T_{new}}}^{\mathrm{max}} = x \times p_{\mathrm{T_{new}}}^{\mathrm{max}}$, where x is the Hard Scale Factor. The Hard Scale Factors used in this analysis were $x = 0.5$ and $x = 2.0$. For both HardScaleFactors, the acceptances are calculated and are shown in Table 9.2, which are used to calculate a relative signal acceptance uncertainty of 3.1%. This small uncertainty is not included in the final fits.

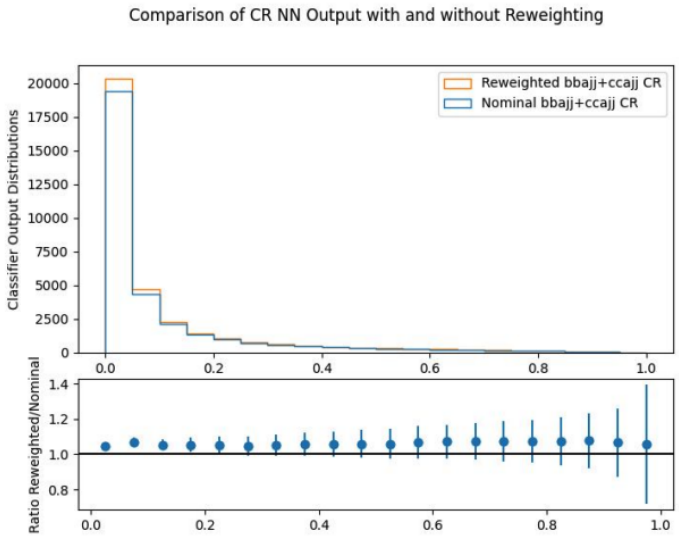

Figure 9.2: The nominal DNN output (blue) is affected by reweighting $b\bar{b}\gamma jj$ and $c\bar{c}\gamma jj$ MC input variables with the MC-to-data ratio plots. The DNN output after kinematically reweighting input variables is shown in orange, and is in agreement with the nominal distribution within a constant factor on the order of a few percent.

9.1.5 Kinematic Reweighting Uncertainty

Kinematic reweighting on DNN input variables has minor effects on the DNN output shape. As shown in Figure 9.2, the nominal DNN output in the control region for $b\bar{b}\gamma jj$ and $c\bar{c}\gamma jj$ is affected by reweighting of the kinematic input variables $b\bar{b}\gamma jj + c\bar{c}\gamma jj$ MC-to-data ratio plot. The DNN output from reweighted kinematic input variables agrees with the nominal DNN output distribution within a constant factor on the order of a few percent.

The uncertainty from reweighting is derived by comparing the difference between two possible reweighting functions. Comparing to no reweighting at all would be an overestimate of the reweighting uncertainty, so it is only shown for qualitative comparison

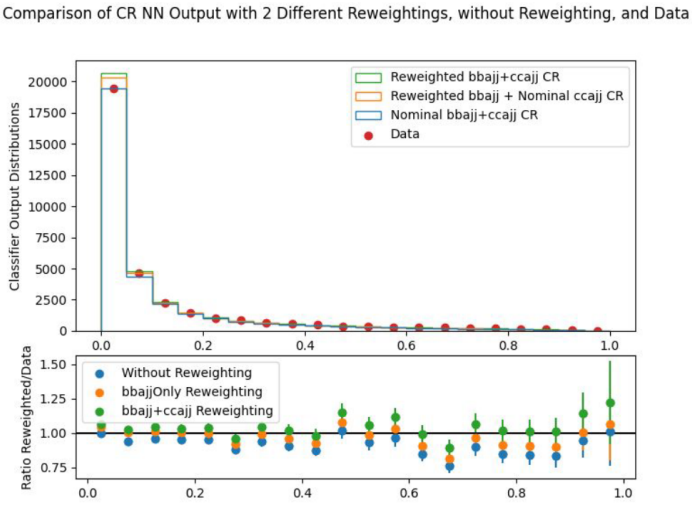

Figure 9.3: The uncertainty due to kinematic reweighting shown for the QCD $b\bar{b}\gamma jj + c\bar{c}\gamma jj$ versus QCD $b\bar{b}\gamma jj$-only DNN output in the sideband control region. The nominal DNN output (blue) without any reweighting and data (red dots) are also shown.

in Figure 9.2. The reweighted combined QCD $b\bar{b}\gamma jj + c\bar{c}\gamma jj$ (green) reweighting function is used for fitting in this analysis. The uncertainty is calculated from reweighting only QCD $b\bar{b}\gamma jj$ and combining it with the nominal $c\bar{c}\gamma jj$ distribution, shown in orange in Figure 9.3. Kinematic reweighting uncertainty has a 10% effect on the signal significance.

9.2 Experimental Systematic Uncertainties

9.2.1 Luminosity and Pileup Systematics

The Luminosity Working Group recommendations for the Full Run 2 final combined systematic due to luminosity uncertainty is 0.83%.[133, 134]. Luminosity calibrations were measured once per year during Run 2 data-taking, and different detectors measured relative comparisons of luminosity.[134] MC is reweighted relative

to data based on the distribution of the pileup mu for the luminosity during each data-taking period in a process known as "Pileup Reweighting" (PRW). The systematics due to pile-up reweighting (`PRW_DATASF`) are estimated by varying the nominal data scale factor of 1.0/1.03 to 1.0/1.0 or 1.0/1.06 to get the up and down variations, respectively, consistent with the Analysis Software Group recommendations.[135]

9.2.2 Jet Systematics

Jet-related uncertainties come primarily from the jet energy scale (JES) and jet energy resolution (JER). JES uncertainties correct data to match MC that is calibrated to truth-scale.[136] The JES "Category Reduction" configuration is implemented, which encompasses about 30 nuisance parameters (NP). For JER, 13 NPs are used as part of the "FullJER" configuration. These configurations follow the current recommendations of the JetEtMiss group for typical precision results and are compatible for combinations with other analyses.[137] Increasing the number of NPs from the previous Full Run 2 analysis, which used 8 NPs in the "SimpleJER" configuration, improves confidence in the results.

The `JetUncertaintiesTool` implements JES systematics, which are based on calibrations relative to well-understood objects. These include in-situ eta calibration with the di-jet (calibrates the forward jet scale relative to central jets), $Z + jet$ balance (calibrates the jet scale relative to a Z), $\gamma + jet$ balance (calibrates the jet scale relative to a γ, and multi-jet balance (calibrates the jet scale relative to previously recoiled system of calibrated jets). Pileup uncertainties, flavor-related uncertainties, and punch-through

uncertainties are also considered. MC non-closure uncertainty is not considered for full simulation samples.

The JER uncertainties are implemented with the `JERSmearingTool`. JER uncertainties arise from differences in data versus MC, evaluation of noise terms from random cones in zero-bias data, and asymmetric dijet p_T balance.[137] Gaussian jet smearing is used to propagate JER uncertainties.[136] If $\sigma_{NP} > 0$, the MC is smeared, but if $\sigma < 0$ the data is smeared.

We estimate that JER and JES combined uncertainties have a 15.6% contribution on the signal significance.

9.2.3 Flavor Tagging Systematics

Uncertainties from b-jet tagging are evaluated using the event-weight systematics by varying the scale factors. A scale factor is imported from the flavor tagging group's CDI (Calibration Data Interface) file `2020-21-13TeV-MC16-CDI-2021-04-16_v1` with the `BTaggingEfficiencyTool` for each of the two b-jets required by the event selection.[138] The CDI file efficiency maps are derived from $t\bar{t}$ MC samples.[138] The scale factor is defined as the ratio of the b-tagging efficiency in data over the b-tagging efficiency of a reference MC. The scale factor from each of the b-tagged jets are then multiplied together, and that product is the event weight that corrects the MC tagging rate to match that of data.[138] The b-tagging efficiency uncertainty is estimated to be small, so it is neglected in the final fit.

9.2.4 Photon Efficiency Uncertainty

The photon identification efficiency is measured with pp collision data from 2015-2016 at $\sqrt{s} = 13$ TeV for converted and unconverted isolated photons, and contributes 0.5% to 5% depending on photon p_T and $|\eta|$.[139] Photon identification efficiency increases at higher E_T. "Tight" photons are identified using radiative Z boson decays of $Z \to ll\gamma$, electron extrapolation of $Z \to ee$, or inclusive photons from the single-photon triggers.[139]

Data is used to measure the likelihood of mistakenly reconstructing an electron as a photon, and this rate is only a few percent in the central region.[139] The likelihood is higher in the forward regions, and reaches an upper limit of 10-20% for converted photons.[139]

The `PhotonEfficiencyCorrectionTool` provided by the e/gamma group is applied on MC to match the efficiency measured in data. The systematic variation `PH_EFF_ID_Uncertainty` is used.

9.2.5 EM Scale and Resolution Systematics

The e/gamma group recommendations for the electron and photon energy scale and resolution systematic uncertainties are used.[140] A multivariate regression algorithm optimizes the electron and photon energy resolution using the showers in the EM calorimeter. The energy scale is calibrated using for a $Z \to ee$ data sample, and is verified with radiative Z boson decays.[141] The full model energy calibration includes considerations of more than 60 systematic variations. However, the photon energy scale

and resolution systematic uncertainties are not dominant systematic sources so this analysis is very weakly sensitive to the energy scale and resolution. These uncertainties are not included in the fit.

9.3 Statistical Uncertainties

MC statistical uncertainty is greatly reduced in this legacy analysis compared to the previous Full Run 2 Analysis, due to the new/extended 300 million event QCD $b\bar{b}\gamma jj$ described in Chapter 5.2. The MC statistical uncertainty is reduced to $\sigma(\mu_H) = 0.05$.

The data statistical uncertainty remains a challenge in this legacy analysis, contributing $\sigma(\mu_H) = 0.78$. This is due to the small cross section of the $H+\gamma$ production at $\sqrt{s} = 13$ TeV and the trigger constraints.

9.4 Fit Results for Higgs Boson Production

The DNN output from data is fit and superimposed with the MC template including signal $H\gamma jj$ and all backgrounds using `TRExFitter`. The fits to data with the MC in the control and signal regions are shown in Figure 9.4 for 20 equal bins. The background QCD $b\bar{b}\gamma jj$ is visible in yellow, the background QCD $c\bar{c}\gamma jj$ is visible in blue, and the $H\gamma jj$ signal is visible in red (especially in the three highest bins). Other backgrounds mentioned in Section 8.2 are included in the fit, but have such small contributions that they are not visible in the plot. There is a slight excess of MC events in the second-to-last bin, but otherwise the data/MC agreement for NN scores above 0.8

agree within uncertainties.

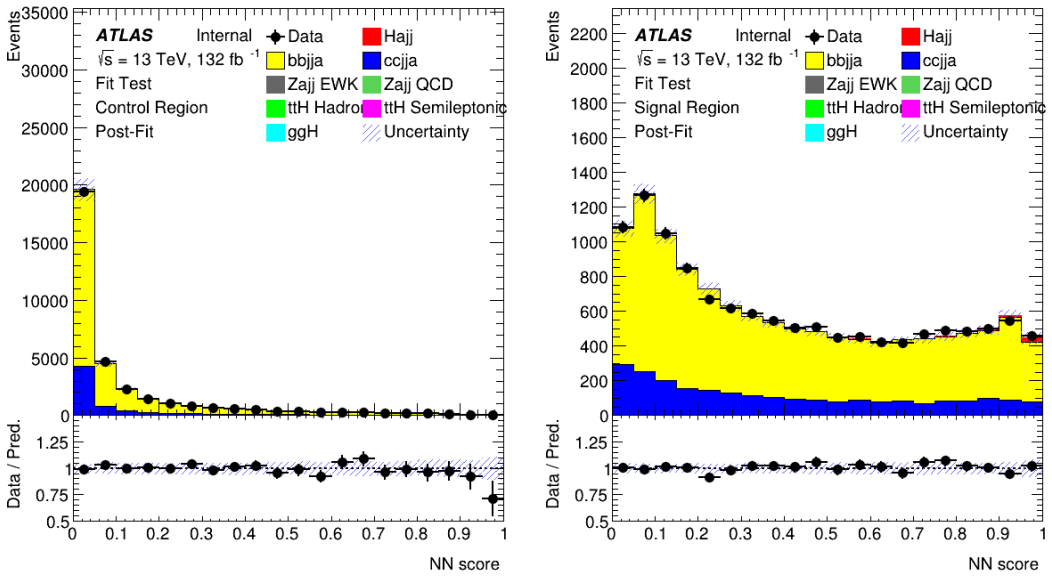

(a) Control Region

(b) Signal Region

Figure 9.4: Fit results in the (a) m_{bb} sideband control region and (b) window signal region using 20 equal bins. Although $b\bar{b}\gamma jj$ (yellow) and $c\bar{c}\gamma jj$ (blue) events dominate, signal $H\gamma jj$ (red) events are particularly visible in the three highest bins. There is a slight excess of MC events in the second-to-last bin, but otherwise the data/MC agreement for NN scores above 0.8 agree within uncertainties.

Post-fit yields are shown in Table 9.3. Like the post-fit plots shown in Figure 9.4, they show that the QCD $b\bar{b}\gamma jj$ and $c\bar{c}\gamma jj$ contributions dominate in both the signal and control regions. These backgrounds are suppressed in the signal region while the $H\gamma jj$ signal has a larger contribution in the signal region than the control region, as intended.

The m_{bb} window signal region fit is used to extract the Higgs boson signal strength μ_H with all uncertainties combined. The observed inclusive signal strength μ_H is 0.9 ± 0.9. The dominant uncertainty is the data statistical uncertainty, as was the

Sample	Signal Region	Control Region
$H\gamma jj$	57.7 ± 45.3	12.8 ± 10.1
$b\bar{b}\gamma jj$	10111.3 ± 156.5	28408 ± 471.3
$c\bar{c}\gamma jj$	2372.8 ± 14.2	6693.9 ± 37.3
$Z\gamma jj$ QCD	24.16 ± 0.1	97.2 ± 0.5
$Z\gamma jj$ EWK	12.36 ± 0.08	65.6 ± 0.4
ttH Semi-leptonic	2.41 ± 0.02	4.07 ± 0.02
ttH Hadronic	1.64 ± 0.01	2.81 ± 0.02
ggH	0.618 ± 0.004	0.181 ± 0.001
Total	12583.1 ± 168.2	35284.6 ± 483.9
Data	12349	33486

Table 9.3: Post-fit yields in the signal and control regions for signal and background samples considered.

case in the previous Full Run 2 Analysis.[97] Kinematic reweighting uncertainty is a new systematic uncertainty included in this legacy analysis, and has a non-negligible effect on the signal significance uncertainty. The total uncertainty is reduced compared to the previous Full Run 2 analysis, however, primarily because of a decrease in the MC statistical uncertainty and fit to DNN output instead of m_{bb}. A summary of theory, experimental, and statistical systematic effects on the signal strength are shown in Table 9.4. Each uncertainty source is added in quadrature to calculate the total uncertainty.

After considering all of the theory, experimental, and statistical systematic effects, the observed significance of the Higgs boson signal relative to the background is 0.98σ, compared to 1.02σ expected. This result is consistent with the previous Full Run 2 result and the SM expectations.[97]

Source of uncertainty on background	$\sigma(\mu_H)$
Statistical	
Data statistical	0.78
MC statistical	0.05
Systematic	
Luminosity	0.02
Kinematic reweighting	0.09
Jet + Egamma + Muon + pileup	0.03
Theoretical	0.01
Total	0.86

Table 9.4: Effects of the statistical, theoretical, and experimental uncertainties on the signal strength. Data statistical uncertainty is the single largest contribution to the uncertainty.

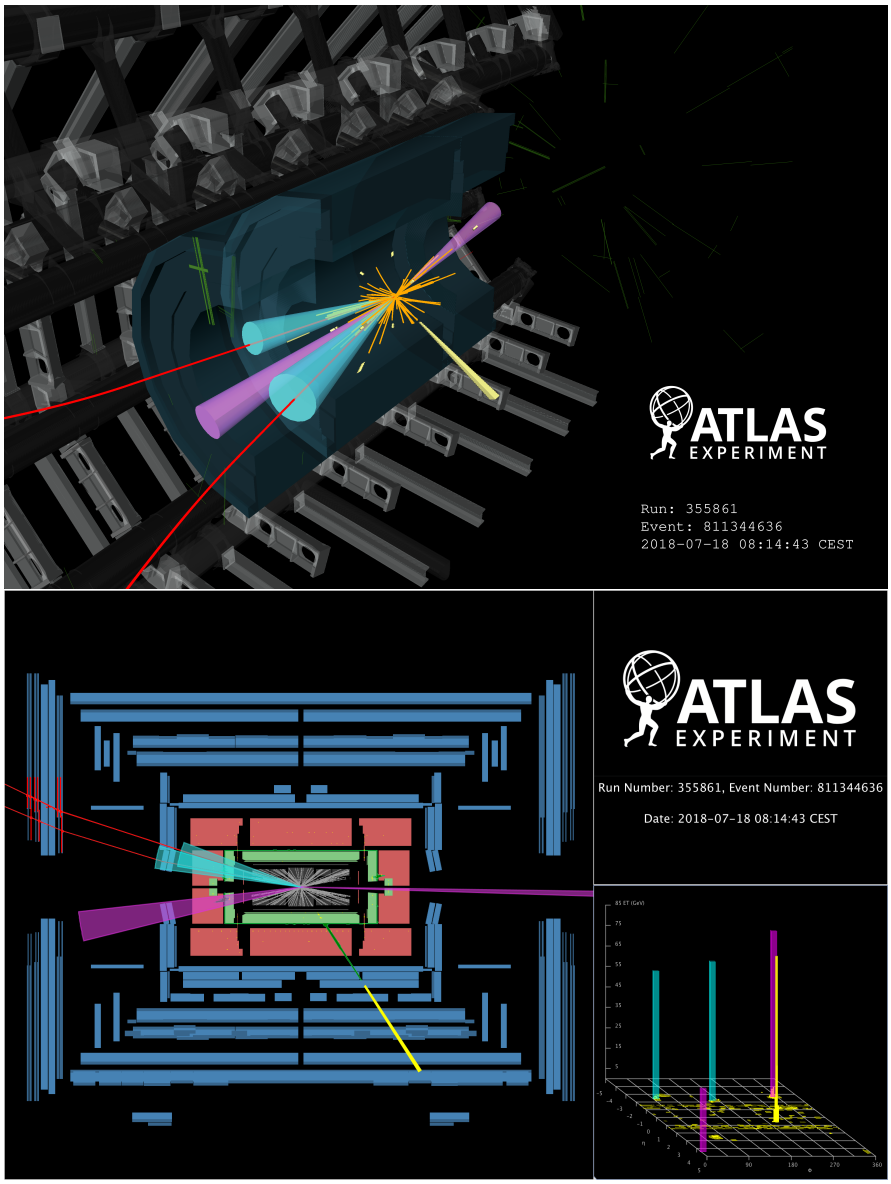

Figure 9.5: Event display of a candidate Higgs boson produced in the VBF $H(\to b\bar{b}) + \gamma$ signature during Run 355861. Event 811344636 shows two b-jets from a Higgs boson candidate with an invariant mass of 120 GeV and a pseudorapidity of $\eta = -2.2$ in cyan. The two VBF jets with an invariant mass of 1006 GeV are shown in purple. The photon with a transverse momentum of 81 GeV is represented as a yellow energy histogram. Two muons are shown as red tracks from the b-jets.

Chapter 10

Conclusion

This legacy analysis searches for a SM Higgs boson produced via vector boson fusion in association with a high-energy photon using the 132 fb^{-1} of Run 2 data collected with the ATLAS detector. This VBF $H(\to b\bar{b}) + \gamma$ analysis trains a DNN to separate signal and background events, and the DNN output is fit with a binned-likelihood fit to extract the Higgs boson signal production strength. We measure a Higgs boson signal strength relative to SM predictions of $\mu_H = 0.9 \pm 0.9$, corresponding with an observed signal significance of 0.98σ, compared to 1.02σ expected.

This VBF $H(\to b\bar{b}) + \gamma$ legacy analysis updates Monte Carlo samples separating signal and background events with a DNN, and uses a binned fit to DNN output strategy. The statistical uncertainty from Monte Carlo was greatly reduced thanks to generation of larger background QCD samples. Data statistics are still limited and contribute significantly to μ_H uncertainty.

10.1 The Future for VBF $H(b\bar{b}) + \gamma$

Run 3 and the future HL-LHC runs will offer several opportunities for improvement in VBF $H(b\bar{b}) + \gamma$ analysis. During Run 3, additional VBF triggers, such as the L1Topo VBF+$b\bar{b}$ trigger, will help select for VBF events specifically. The increase in data will also greatly reduce data statistical uncertainty, which is a large limitation in the current analysis.

During the HL-LHC runs, the HGTD forward timing detectors will provide an opportunity to take advantage of reduced pileup. In addition, selection of VBF jets is expected to improve with more data available at high-p_T.[142]

Bibliography

[1] J. Thomson. "Cathode Rays." *Philosophical Magazine and Journal of Science* (1897).

[2] B. Ryden and B. M. Peterson. *Foundations of Astrophysics*. Addison Wesley, 2010.

[3] P. Gagnon. "The Standard Model" (2014). URL: https://www.quantumdiaries.org/2014/03/14/the-standard-model-a-beautiful-but-flawed-theory/.

[4] M. Gell-Mann. "A schematic model of baryons and mesons." *Physics Letters* 8.3 (1964), pp. 214–215. ISSN: 0031-9163. DOI: https://doi.org/10.1016/S0031-9163(64)92001-3. URL: https://www.sciencedirect.com/science/article/pii/S0031916364920013.

[5] G. Zweig. "An SU(3) model for strong interaction symmetry and its breaking. Version 2." *Developments in the Quark Theory of Hadrons. VOL. 1. 1964 - 1978.* Ed. by D. B. Lichtenberg and S. P. Rosen. Feb. 1964, pp. 22–101.

[6] P. W. Higgs. "Broken symmetries, massless particles and gauge fields." *Phys. Lett.* 12 (1964), pp. 132–133. DOI: 10.1016/0031-9163(64)91136-9.

[7] C. Csáki and P. Tanedo. "Beyond the Standard Model." *2013 European School of High-Energy Physics*. 2015, pp. 169–268. DOI: 10.5170/CERN-2015-004.169. arXiv: 1602.04228 [hep-ph].

[8] W. Pauli. "Über den Zusammenhang des Abschlusses der Elektronengruppen im Atom mit der Komplexstruktur der Spektren." *Zeitschrift für Physik* 31.1 (1925), pp. 765–783. DOI: 10.1007/BF02980631. URL: https://doi.org/10.1007/BF02980631.

[9] E. D. Bloom et al. "High-Energy Inelastic $e-p$ Scattering at 6° and 10°." *Phys. Rev. Lett.* 23 (16 Oct. 1969), pp. 930–934. DOI: 10.1103/PhysRevLett.23.930. URL: https://link.aps.org/doi/10.1103/PhysRevLett.23.930.

[10] S. Bose. "Plack's Law and Light Quantum Hypothesis" (1924).

[11] H. Yukawa. "On the Interaction of Elementary Particles." *Progress of Theoretical Physics Supplement* 1 (1955), pp. 1–10.

[12] C. M. Lattes et al. "Processes involving charged mesons." *Nature* 159.4047 (1947), pp. 694–697.

[13] UA1 Collaboration. "Experimental observation of isolated large transverse energy electrons with associated missing energy at $\sqrt{s} = 540$ GeV." *Physics Letters B* 122.1 (1983), pp. 103–116. ISSN: 0370-2693. DOI: https://doi.org/10.1016/0370-2693(83)91177-2. URL: https://www.sciencedirect.com/science/article/pii/0370269383911772.

[14] UA2 Collaboration. "Observation of single isolated electrons of high transverse momentum in events with missing transverse energy at the CERN pp collider." *Physics Letters B* 122.5 (1983), pp. 476–485. ISSN: 0370-2693. DOI: https://doi.org/10.1016/0370-2693(83)91605-2. URL: https://www.sciencedirect.com/science/article/pii/0370269383916052.

[15] UA2 Collaboration. "Evidence for $Z^0 \to e^+e^-$ at the CERN pp collider." *Physics Letters B* 129.1 (1983), pp. 130–140. ISSN: 0370-2693. DOI: https://doi.org/10.1016/0370-2693(83)90744-X. URL: https://www.sciencedirect.com/science/article/pii/037026938390744X.

[16] F. Englert and R. Brout. "Broken Symmetry and the Mass of Gauge Vector Mesons." *Phys. Rev. Lett.* 13 (9 Aug. 1964), pp. 321–323. DOI: 10.1103/PhysRevLett.13.321. URL: https://link.aps.org/doi/10.1103/PhysRevLett.13.321.

[17] P. W. Anderson. "Plasmons, Gauge Invariance, and Mass." *Phys. Rev.* 130 (1 Apr. 1963), pp. 439–442. DOI: 10.1103/PhysRev.130.439. URL: https://link.aps.org/doi/10.1103/PhysRev.130.439.

[18] G. S. Guralnik, C. R. Hagen, and T. W. B. Kibble. "Global Conservation Laws and Massless Particles." *Phys. Rev. Lett.* 13 (20 Nov. 1964), pp. 585–587. DOI: 10.1103/PhysRevLett.13.585. URL: https://link.aps.org/doi/10.1103/PhysRevLett.13.585.

[19] G. 't Hooft. "Renormalizable Lagrangians for Massive Yang-Mills Fields." *Nucl. Phys. B* 35 (1971). Ed. by J. C. Taylor, pp. 167–188. DOI: 10.1016/0550-3213(71)90139-8.

[20] R. B. et. al. "New Determination of the Fine Structure Constant and Test of the Quantum Electrodynamics." *Physical Review Letters* 106.8 (Feb. 2011).

[21] J. Ellis, M. K. Gaillard, and G. G. Ross. "Search for gluons in e^+e^- annihilation." *Nuclear Physics B* 111.2 (1976), pp. 253–271. ISSN: 0550-3213. DOI: https://doi.org/10.1016/0550-3213(76)90542-3. URL: https://www.sciencedirect.com/science/article/pii/0550321376905423.

[22] H. Fritzsch and M. Gell-Mann. "Current algebra: Quarks and what else?" *eConf* C720906V2 (1972). Ed. by J. D. Jackson and A. Roberts, pp. 135–165. arXiv: hep-ph/0208010.

[23] J. C. Maxwell. "A Dynamical Theory of the Electromagnetic Field." *Phil. Trans. R. Soc. Lond.* 155 (1865), pp. 459–512.

[24] S.-I. Tomonaga and J. R. Oppenheimer. "On Infinite Field Reactions in Quantum Field Theory." *Phys. Rev.* 74 (2 July 1948), pp. 224–225. DOI: 10.1103/PhysRev.74.224. URL: https://link.aps.org/doi/10.1103/PhysRev.74.224.

[25] R. P. Feynman. "Space-Time Approach to Quantum Electrodynamics." *Phys. Rev.* 76 (6 Sept. 1949), pp. 769–789. DOI: 10.1103/PhysRev.76.769. URL: https://link.aps.org/doi/10.1103/PhysRev.76.769.

[26] J. Schwinger. "On Quantum-Electrodynamics and the Magnetic Moment of the Electron." *Phys. Rev.* 73 (4 Feb. 1948), pp. 416–417. DOI: 10.1103/PhysRev.73.416. URL: https://link.aps.org/doi/10.1103/PhysRev.73.416.

[27] S. L. Glashow. "Partial Symmetries of Weak Interactions." *Nucl. Phys.* 22 (1961), pp. 579–588. DOI: 10.1016/0029-5582(61)90469-2.

[28] CDF Collaboration. "High-precision measurement of the W boson mass with the CDF II detector." *Science* 376.6589 (2022), pp. 170–176. DOI: 10.1126/science.abk1781. eprint: https://www.science.org/doi/pdf/10.1126/science.abk1781.

[29] S. L. Glashow. "The renormalizability of vector meson interactions." *Nuclear Physics* 10 (1959), pp. 107–117. ISSN: 0029-5582. DOI: https://doi.org/10.1016/0029-5582(59)90196-8. URL: https://www.sciencedirect.com/science/article/pii/0029558259901968.

[30] A. Salam and J. C. Ward. "Weak and electromagnetic interactions." *Il Nuovo Cimento (1955-1965)* 11.4 (1959), pp. 568–577. DOI: 10.1007/BF02726525. URL: https://doi.org/10.1007/BF02726525.

[31] S. Weinberg. "A Model of Leptons." *Phys. Rev. Lett.* 19 (21 Nov. 1967), pp. 1264–1266. DOI: 10.1103/PhysRevLett.19.1264. URL: https://link.aps.org/doi/10.1103/PhysRevLett.19.1264.

[32] Z. Bern et al. "Left-handed W bosons at the LHC." *Phys. Rev. D* 84 (3 Aug. 2011), p. 034008. DOI: 10.1103/PhysRevD.84.034008. URL: https://link.aps.org/doi/10.1103/PhysRevD.84.034008.

[33] SLD Collaboration. "High-Precision Measurement of the Left-Right Z Boson Cross-Section Asymmetry." *Phys. Rev. Lett.* 84 (26 June 2000), pp. 5945–5949. DOI: 10.1103/PhysRevLett.84.5945. URL: https://link.aps.org/doi/10.1103/PhysRevLett.84.5945.

[34] ATLAS Collaboration. "Measurement of the effective leptonic weak mixing angle using electron and muon pairs from Z-boson decay in the ATLAS experiment at $\sqrt{s} = 8$ TeV" (July 2018).

[35] E. Noether. "Invariante Variationsprobleme." *Nachr. v. d. Ges. d. Wiss. zu Göttingen* (1918).

[36] J. Goldstone, A. Salam, and S. Weinberg. "Broken Symmetries." *Phys. Rev.* 127 (3 Aug. 1962), pp. 965–970. DOI: 10.1103/PhysRev.127.965. URL: https://link.aps.org/doi/10.1103/PhysRev.127.965.

[37] M. Thomson. *Modern Particle Physics*. Cambridge University Press, 2013.

[38] S. M. Christensen. "Vacuum expectation value of the stress tensor in an arbitrary curved background: The covariant point-separation method." *Phys. Rev. D* 14 (10 Nov. 1976), pp. 2490–2501. DOI: 10.1103/PhysRevD.14.2490. URL: https://link.aps.org/doi/10.1103/PhysRevD.14.2490.

[39] F. Jegerlehner, M. Kalmykov, and B. Kniehl. "Self-consistence of the Standard Model via the renormalization group analysis." *Journal of Physics: Conference Series* 608 (Dec. 2014). DOI: 10.1088/1742-6596/608/1/012074.

[40] CMS Collaboration. "Limits on the Higgs boson lifetime and width from its decay to four charged leptons." *Phys. Rev. D* 92 (7 Oct. 2015), p. 072010. DOI: 10.1103/PhysRevD.92.072010. URL: https://link.aps.org/doi/10.1103/PhysRevD.92.072010.

[41] P. Zyla and others (Particle Data Group). "Review of Particle Physics" (2013). URL: https://pdg.lbl.gov/2013/reviews/rpp2013-rev-higgs-boson.pdf.

[42] CMS Collaboration. "A measurement of the Higgs boson mass in the diphoton decay channel" (2019). URL: http://cms-results.web.cern.ch/cms-results/public-results/preliminary-results/HIG-19-004/index.html.

[43] ATLAS Collaboration. "Observation of a new particle in the search for the Standard Model Higgs boson with the ATLAS detector at the LHC." *Physics Letters B* 716.1 (2012), pp. 1–29. ISSN: 0370-2693. DOI: https://doi.org/10.1016/j.physletb.2012.08.020. URL: https://www.sciencedirect.com/science/article/pii/S037026931200857X.

[44] D. de Florian et al. "Handbook of LHC Higgs Cross Sections: 4. Deciphering the Nature of the Higgs Sector." 2/2017 (Oct. 2016). DOI: 10.23731/CYRM-2017-002. arXiv: 1610.07922 [hep-ph].

[45] E. Gabrielli et al. "Asking for an extra photon in Higgs production at the LHC and beyond." *JHEP* 07 (2016), p. 003. DOI: 10.1007/JHEP07(2016)003. arXiv: 1601.03635 [hep-ph].

[46] ATLAS Collaboration. "Evidence for the $H \to b\bar{b}$ decay with the ATLAS detector." *Journal of High Energy Physics* 2017.12 (2017), p. 24. DOI: 10.1007/JHEP12(2017)024. URL: https://doi.org/10.1007/JHEP12(2017)024.

[47] CMS Collaboration. "Observation of a New Boson at a Mass of 125 GeV with the CMS Experiment at the LHC." *Phys. Lett. B* 716 (2012), pp. 30–61. DOI: 10.1016/j.physletb.2012.08.021. arXiv: 1207.7235 [hep-ex].

[48] "The Nobel Prize in Physics 2013" (2013). URL: https://www.nobelprize.org/prizes/physics/2013/summary/.

[49] ATLAS Collaboration. "Combined measurements of Higgs boson production and decay using up to 139 fb^{-1} of proton-proton collision data at $\sqrt{s} = 13$ TeV collected with the ATLAS experiment" (2021). URL: https://inspirehep.net/literature/1968225.

[50] ATLAS Collaboration. "Measurement of the properties of Higgs boson production at $\sqrt{s} = 13$ TeV in the H $\to \gamma\gamma$ channel using 139 fb^{-1} of pp collision data with the ATLAS experiment." *40th International Conference on High Energy Physics (ICHEP), Prague, Czech Republic, 28 Jul - 6 Aug 2020* (2020). URL: https://atlas.web.cern.ch/Atlas/GROUPS/PHYSICS/CONFNOTES/ATLAS-CONF-2020-026/.

[51] ATLAS Collaboration. "Measurements of Higgs boson production cross-sections in the $H \to \tau^+\tau^-$ decay channel in pp collisions at $\sqrt{s} = 13$ TeV with the ATLAS detector." *JHEP* 08 (2022), p. 175. DOI: 10.1007/JHEP08(2022)175. arXiv: 2201.08269 [hep-ex].

[52] ATLAS Collaboration. "Constraints on Higgs boson production with large transverse momentum using $H \to b\bar{b}$ decays in the ATLAS detector." *Phys. Rev. D* 105.9 (2022), p. 092003. DOI: 10.1103/PhysRevD.105.092003. arXiv: 2111.08340 [hep-ex].

[53] ATLAS Collaboration. "A search for the dimuon decay of the Standard Model Higgs boson with the ATLAS detector." *Phys. Lett. B* 812 (2021). URL: https://atlas.web.cern.ch/Atlas/GROUPS/PHYSICS/PAPERS/HIGG-2019-14/.

[54] ATLAS Collaboration. "Direct constraint on the Higgs-charm coupling from a search for Higgs boson decays into charm quarks with the ATLAS detector." *Eur. Phys. J. C* 82 (2022), p. 717. DOI: 10.1140/epjc/s10052-022-10588-3. arXiv: 2201.11428 [hep-ex].

[55] A. Bazavov et al. "Up-, down-, strange-, charm-, and bottom-quark masses from four-flavor lattice QCD." *Phys. Rev. D* 98 (5 Sept. 2018), p. 054517. DOI: 10.1103/PhysRevD.98.054517. URL: https://link.aps.org/doi/10.1103/PhysRevD.98.054517.

[56] ATLAS Collaboration. "Search for Higgs Boson Production via Weak Boson Fusion in Association with a High-Energy Photon at $\sqrt{s} = 13$ TeV with the ATLAS

detector" (2020). URL: https://cds.cern.ch/record/2673667/files/ATL-COM-PHYS-2019-496.pdf?version=13.

[57] CERN Committee of Council. "Approval of the Large Hadron Collider and the Long-Term Scientific Programme of CERN." 1994. URL: http://cds.cern.ch/record/33284/files/CM-P00079714-e.pdf.

[58] ATLAS Collaboration. "Combined search for the Standard Model Higgs boson in pp collisions at $\sqrt{s}$=7 TeV with the ATLAS detector." *Phys. Rev. D* 86 (3 Aug. 2012), p. 032003. DOI: 10.1103/PhysRevD.86.032003. URL: https://link.aps.org/doi/10.1103/PhysRevD.86.032003.

[59] CERN. "Overall view of the LHC" (2014). URL: https://cds.cern.ch/record/1708849.

[60] L. Rossi. "Superconducting magnets for the LHC main lattice." *IEEE Trans. App. Supercond.* (2004). URL: https://cds.cern.ch/record/732330.

[61] H. Gray and B. Mansoulie. "The Higgs boson: the hunt, the discovery, the study and some future perspectives" (2018). URL: https://atlas.cern/updates/feature/higgs-boson.

[62] CERN. "Restarting the LHC: Why 13 Tev?" (2014). URL: https://home.cern/science/engineering/restarting-lhc-why-13-tev.

[63] B. Salvachua. "Overview of Proton-proton Physics During Run 2" (2019). URL: https://cds.cern.ch/record/2750272/files/1835544_7-14.pdf.

[64] CERN Courier. "Injecting new life into the LHC" (2017). URL: https://cerncourier.com/a/injecting-new-life-into-the-lhc/.

[65] CERN. "CERN's accelerator complex" (2023). URL: https://home.cern/science/accelerators/accelerator-complex.

[66] CERN. "The CERN accelerator complex" (2008). URL: https://cds.cern.ch/record/1260465.

[67] ATLAS Collaboration. "Computer generated image of the whole ATLAS detector" (2008). URL: https://cds.cern.ch/record/1095924.

[68] C. Lippmann. "Particle Identification" (2011). URL: http://cds.cern.ch/record/1323010/plots.

[69] ATLAS Collaboration. "The ATLAS Experiment at the CERN Large Hadron Collider." *Journal of Instrumentation* (2008). URL: https://iopscience.iop.org/article/10.1088/1748-0221/3/08/S08003/pdf.

[70] K. Reygers and J. Stachel. "QGP Physics - from Fixed Target to LHC" (2015). URL: https://www.physi.uni-heidelberg.de/~reygers/lectures/2015/qgp/qgp2015_02_kinematics.pdf.

[71] ATLAS Collaboration. "ATLAS Inner Detector" (2008). URL: https://mediastream.cern.ch/MediaArchive/Photo/Public/2008/0803014/0803014_01/0803014_01-A4-at-144-dpi.jpg.

[72] ATLAS Collaboration. "Experiment Briefing: Keeping the ATLAS Inner Detector in perfect alignment" (2020). URL: https://cds.cern.ch/record/2723878/files/IDbriefing_figure1.png?subformat=icon-1440.

[73] ATLAS Collaboration. "The Inner Detector" (2023). URL: https://atlas.cern/Discover/Detector/Inner-Detector.

[74] ATLAS Pixel Collaboration. "The Pixel Detector of the ATLAS Experiment for LHC Run-2" (2015). URL: https://cds.cern.ch/record/1985432/files/ATL-INDET-PROC-2015-001.pdf.

[75] A. La Rosa. "The ATLAS Insertable B-Layer: from construction to operation." *JINST* 11.12 (2016). Ed. by C. Gemme and L. Rossi, p. C12036. DOI: 10.1088/1748-0221/11/12/C12036. arXiv: 1610.01994 [physics.ins-det].

[76] D.-L. Pohl. "Overview of the ATLAS Insertable B-Layer (IBL) Project." *PoS* RD13 (2013), p. 012. DOI: 10.22323/1.189.0012.

[77] ATLAS Collaboration. "Operation and performance of the ATLAS semiconductor tracker in LHC Run 2." *JINST 17 (2022) P01013* (2021). URL: https://arxiv.org/pdf/2109.02591.pdf.

[78] A. Vogel. "ATLAS Transition Radiation Tracker (TRT): Straw Tube Gaseous Detectors at High Rates" (2013). URL: http://cds.cern.ch/record/1537991/files/ATL-INDET-PROC-2013-005.pdf?version=1.

[79] ATLAS Collaboration. "Performance of the ATLAS Transition Radiation Tracker in Run 1 of the LHC: tracker properties." *JINST* 12.05 (2017), P05002. DOI: 10.1088/1748-0221/12/05/P05002. arXiv: 1702.06473 [hep-ex].

[80] ATLAS Collaboration. "ATLAS Calorimeter" (2008). URL: https://mediaarchive.cern.ch/MediaArchive/Photo/Public/2008/0803015/0803015_01/0803015_01-A4-at-144-dpi.jpg.

[81] N. Nikiforou. "Performance of the ATLAS liquid argon calorimeter after three years of lhc operation and plans for a future upgrade" (2013), pp. 1–12. DOI: 10.1109/ANIMMA.2013.6728060.

[82] A. Henriques. "The ATLAS Tile Calorimeter" (2015). URL: https://cds.cern.ch/record/2004868/files/ATL-TILECAL-PROC-2015-002.pdf.

[83] L. Pontecorvo. "The ATLAS Muon Spectrometer." *EPJ* (2003). URL: https://cds.cern.ch/record/676896/files/sn-atlas-2003-030.pdf.

[84] S. Palestini. "The Muon Spectrometer of the ATLAS Experiment" (2002). URL: https://palesti2.web.cern.ch/Documents/SPsienaNote.pdf.

[85] W. Buttinger. "The ATLAS Level-1 Trigger System." *Journal of Physics: Conference Series* 396.1 (Dec. 2012), p. 012010. DOI: 10.1088/1742-6596/396/1/012010. URL: https://dx.doi.org/10.1088/1742-6596/396/1/012010.

[86] ATLAS Collaboration. "Resolution of the ATLAS muon spectrometer monitored drift tubes in LHC Run 2." *JINST* 14.P09011 (2019).

[87] ATLAS Collaboration. "ATLAS Muon Spectrometer" (2008). URL: https://mediaarchive.cern.ch/MediaArchive/Photo/Public/2008/0803017/0803017_01/0803017_01-A4-at-144-dpi.jpg.

[88] ATLAS Collaboration. "Magnet System" (2008). URL: https://atlas.cern/Discover/Detector/Magnet-System.

[89] J. J. Goodson. "Search for Supersymmetry in States with Large Missing Transverse Momentum and Three Leptons including a Z-Boson" (2012). URL: https://www.proquest.com/dissertations-theses/search-supersymmetry-states-with-large-missing/docview/1034736145/se-2?accountid=14523.

[90] C. Bourdar. "The B0 in a nutshell" (2019). URL: https://cbourdar.web.cern.ch/sites/default/files/2019-11/The%20B0%20in%20a%20nutshell.pdf.

[91] J. M. Berlingen. "Triggering in the ATLAS experiment." *Proceedings of Science* (2020). URL: https://cds.cern.ch/record/2742661/files/ATL-DAQ-PROC-2020-023.pdf.

[92] ATLAS Collaboration. "ATLAS DCS FSM" (2012). URL: https://twiki.cern.ch/twiki/pub/AtlasPublic/ApprovedPlotsDCS/ATLAS_DCS_FSM_plain.png.

[93] F. Klimpel. "Fast tracking for the HL-LHC ATLAS detector" (2020). URL: https://cds.cern.ch/record/2721751/files/ATL-PHYS-PROC-2020-044.pdf.

[94] ATLAS Collaboration. "A High-Granularity Timing Detector for the ATLAS Phase-II Upgrade" (2020). URL: https://cds.cern.ch/record/2719855?ln=en.

[95] H. F. W. Sadrozinski, A. Seiden, and N. Cartiglia. "4D tracking with ultra-fast silicon detectors." *Rept. Prog. Phys.* 81.2 (2018), p. 026101. DOI: 10.1088/1361-6633/aa94d3. arXiv: 1704.08666 [physics.ins-det].

[96] G. Giacomini et al. "Fabrication of Different LGAD-Based Devices at BNL." *2021 IEEE Nuclear Science Symposium and Medical Imaging Conference (NSS/MIC)*. 2021, pp. 1–4. DOI: 10.1109/NSS/MIC44867.2021.9875599.

[97] ATLAS Collaboration. "Search for Higgs boson production in association with a high-energy photon via vector-boson fusion with decay into bottom quark pairs at $\sqrt{s}$=13 TeV with the ATLAS detector." *JHEP* 03 (2021), p. 268. DOI: 10.1007/JHEP03(2021)268. arXiv: 2010.13651 [hep-ex].

[98] ATLAS Collaboration. "Measurements of Higgs bosons decaying to bottom quarks from vector boson fusion production with the ATLAS experiment at $\sqrt{s} = 13\,\text{TeV}$." *Eur. Phys. J. C* 81.6 (2021), p. 537. DOI: 10.1140/epjc/s10052-021-09192-8. arXiv: 2011.08280 [hep-ex].

[99] ATLAS Collaboration. "Electron and photon trigger efficiencies measured on early 2018 data for LHCC" (2018). URL: https://cds.cern.ch/record/2318523/files/ATL-COM-DAQ-2018-049.pdf?version=6.

[100] J. Alwall et al. "The automated computation of tree-level and next-to-leading order differential cross sections, and their matching to parton shower simulations." *JHEP* 07 (2014), p. 079. DOI: 10.1007/JHEP07(2014)079. arXiv: 1405.0301 [hep-ph].

[101] E. Bothmann et al. "Event Generation with Sherpa 2.2." *SciPost Phys.* 7.3 (2019), p. 034. DOI: 10.21468/SciPostPhys.7.3.034. arXiv: 1905.09127 [hep-ph].

[102] K. Arnold et al. "VBFNLO: A Parton Level Monte Carlo for Processes with Electroweak Bosons – Manual for Version 2.5.0" (Jan. 2011).

[103] ATLAS Analysis Software Group. "JobOption Filters" (2023). URL: https://atlassoftwaredocs.web.cern.ch/AnalysisSWTutorial/mc_filters/.

[104] S. Frixione. "Isolated photons in perturbative QCD." *Phys. Lett. B* 429 (1998), pp. 369–374. DOI: 10.1016/S0370-2693(98)00454-7. arXiv: hep-ph/9801442.

[105] W. Furry. "A Symmetry Theorem in the Positron Theory." *Phys. Rev.* 51 (1937), pp. 125–129. DOI: 10.1103/PhysRev.51.125.

[106] M. Cacciari et al. "The anti-k_t jet clustering algorithm." *JHEP* (2008). URL: https://iopscience.iop.org/article/10.1088/1126-6708/2008/04/063.

[107] ATLAS Collaboration. "Jet reconstruction and performance using particle flow with the ATLAS Detector." *Eur. Phys. J. C* 77.7 (2017), p. 466. DOI: 10.1140/epjc/s10052-017-5031-2. arXiv: 1703.10485 [hep-ex].

[108] ATLAS Collaboration. "Jet energy scale measurements and their systematic uncertainties in proton-proton collisions at $\sqrt{s}$ = 13 TeV with the ATLAS detector." *Phys. Rev. D* 96.7 (2017), p. 072002. DOI: 10.1103/PhysRevD.96.072002. arXiv: 1703.09665 [hep-ex].

[109] ATLAS Collaboration. *Tagging and suppression of pileup jets with the ATLAS detector*. ATLAS-CONF-2014-018. 2014. URL: https://cds.cern.ch/record/1700870.

[110] "Pileup Jet Recommendations" (2023). URL: https://twiki.cern.ch/twiki/bin/viewauth/AtlasProtected/PileupJetRecommendations.

[111] ATLAS Collaboration. "Identification and rejection of pile-up jets at high pseudorapidity with the ATLAS detector." *Eur. Phys. J. C* 77.9 (2017). [Erratum: Eur.Phys.J.C 77, 712 (2017)], p. 580. DOI: 10.1140/epjc/s10052-017-5081-5. arXiv: 1705.02211 [hep-ex].

[112] ATLAS Collaboration. "ATLAS flavour-tagging algorithms for the LHC Run 2 pp collision dataset." *EPJC* (2022). URL: https://arxiv.org/pdf/2211.16345.pdf.

[113] B. Liu. "Final Run2 FTAG Recommendations" (2023). URL: https://twiki.cern.ch/twiki/bin/view/Sandbox/BTaggingEfficienciesFinalRun2Rel21#77_WP.

[114] ATLAS Collaboration. "Search for new resonances in mass distributions of jet pairs using 139 fb^{-1} of pp collisions at $\sqrt{s}$= 13 TeV with the ATLAS detector." *Journal of High Energy Physics* 2020.3 (2020), p. 145. DOI: 10.1007/JHEP03(2020)145. URL: https://doi.org/10.1007/JHEP03(2020)145.

[115] ATLAS Collaboration. "Measurements of WH and ZH production in the $H \to b\bar{b}$ decay channel in pp collisions at 13 TeV with the ATLAS detector." *The European*

Physical Journal C 81.2 (2021), p. 178. DOI: 10.1140/epjc/s10052-020-08677-2. URL: https://doi.org/10.1140/epjc/s10052-020-08677-2.

[116] R. Bouquet. "Energy scale calibration of b-tagged jets with ATLAS Run 2 data using $t\bar{t}$ lepton+jets events" (2022). URL: https://cds.cern.ch/record/2808578/files/ATL-PHYS-PROC-2022-026.pdf.

[117] ATLAS Collaboration. "Electron and photon performance measurements with the ATLAS detector using the 2015–2017 LHC proton–proton collision data." *JINST* 14 (2019), P12006. DOI: 10.1088/1748-0221/14/12/P12006. arXiv: 1908.00005 [hep-ex].

[118] G. Gessner. "Photon identification with the ATLAS detector." *Proceedings of Science* (2017). URL: https://cds.cern.ch/record/2281395/files/ATL-PHYS-PROC-2017-105.pdf.

[119] ATLAS Collaboration. "Electron efficiency measurements with the ATLAS detector using 2012 LHC proton–proton collision data." *Eur. Phys. J. C* 77 (2017), p. 195. DOI: 10.1140/epjc/s10052-017-4756-2. arXiv: 1612.01456 [hep-ex].

[120] ATLAS Collaboration. "Muon reconstruction performance of the ATLAS detector in proton–proton collision data at $\sqrt{s} = 13\,\text{TeV}$." *Eur. Phys. J. C* 76 (2016), p. 292. DOI: 10.1140/epjc/s10052-016-4120-y. arXiv: 1603.05598 [hep-ex].

[121] "Overlap Removal" (2022). URL: https://twiki.cern.ch/twiki/bin/view/AtlasProtected/OverlapRemoval.

[122] "Derivation Framework Run 2" (2022). URL: https://twiki.cern.ch/twiki/bin/view/AtlasProtected/DerivationFrameworkRun2.

[123] R. Brun and F. Rademakers. "ROOT-An Object-Oriented Data Analysis Framework." *Nuclear Instruments and Methods in Physics* 389 (1997), pp. 81–86. URL: https://root.cern/manual/.

[124] D. Rainwater, R. Szalapski, and D. Zeppenfeld. "Probing color-singlet exchange in $Z+2$-jet events at the CERN LHC." *Phys. Rev. D* 54 (11 Dec. 1996), pp. 6680–6689. DOI: 10.1103/PhysRevD.54.6680. URL: https://link.aps.org/doi/10.1103/PhysRevD.54.6680.

[125] F. Chollet et al. "Keras" (2015).

[126] M. Abadi et al. "TensorFlow: Large-Scale Machine Learning on Heterogeneous Systems" (2015). URL: https://www.tensorflow.org/.

[127] "TRExFitter" (2022). URL: https://trexfitter-docs.web.cern.ch/trexfitter-docs/.

[128] ATLAS Collaboration. "Supporting Note for the ATLAS Vector Boson Fusion plus a photon and missing transverse momentum with 139 fb^{-1}" (2021). URL: https://cds.cern.ch/record/2717547/files/ATL-COM-PHYS-2020-317.pdf.

[129] N. Berger. "Lecture on ATLAS Statistical Lecture on ATLAS Statistical Analysis Methods." *6th International Conference on New Frontiers in Physics*. 2017. URL: https://cds.cern.ch/record/2285058/files/ATL-PHYS-SLIDE-2017-797.pdf.

[130] ATLAS Physics Modelling Group. "PMG Systematic Uncertainty Recipes: Scale Uncertainties" (2022). URL: https://twiki.cern.ch/twiki/bin/viewauth/AtlasProtected/PmgSystematicUncertaintyRecipes#Scale_uncertainties.

[131] A. Buckley et al. "LHAPDF6: parton density access in the LHC precision era." *The European Physical Journal C* 75.3 (2015), p. 132. DOI: 10.1140/epjc/s10052-015-3318-8. URL: https://doi.org/10.1140/epjc/s10052-015-3318-8.

[132] "LHAPDF sets" (2021). URL: https://lhapdfsets.web.cern.ch/current/PDF4LHC21_40_pdfas/PDF4LHC21_40_pdfas.info.

[133] ATLAS Luminosity Group. "Luminosity for Physics" (2023). URL: https://twiki.cern.ch/twiki/bin/viewauth/Atlas/LuminosityForPhysics.

[134] ATLAS Collaboration. "Luminosity determination in pp collisions at $\sqrt{s} = 13$ TeV using the ATLAS detector at the LHC" (June 2019).

[135] ATLAS Analysis Software Group. "Pileup Reweighting" (2022). URL: https://twiki.cern.ch/twiki/bin/view/AtlasProtected/ExtendedPileupReweighting.

[136] M. Swiatlowski. "FullJER is Your Friend" (2021). URL: https://indico.cern.ch/event/1051376/contributions/4420484/attachments/2270608/3856133/jer.pdf.

[137] ATLAS Jet Et Miss Group. "Jet Uncertainties Release 21 Summer 2018 Small R" (2018). URL: https://twiki.cern.ch/twiki/bin/viewauth/AtlasProtected/JetUncertaintiesRel21Summer2018SmallR.

[138] ATLAS Flavour Tagging Group. "Tagger Calibration Recommendations for Release 21" (2018). URL: https://twiki.cern.ch/twiki/bin/view/AtlasProtected/BTagCalib2017#Recommendation_October_2018.

[139] ATLAS Collaboration. "Measurement of the photon identification efficiencies with the ATLAS detector using LHC Run 2 data collected in 2015 and 2016." *Eur. Phys. J. C* 79.3 (2019), p. 205. DOI: 10.1140/epjc/s10052-019-6650-6. arXiv: 1810.05087 [hep-ex].

[140] ATLAS Electron Photon Group. "Electron and Photon Calibration for Run 2 (energy scale and resolution)" (2016). URL: https://twiki.cern.ch/twiki/bin/view/AtlasProtected/EGammaCalibrationRun2.

[141] ATLAS Collaboration. "Electron and photon performance measurements with the ATLAS detector using the 2015–2017 LHC proton-proton collision data." *JINST* 14.12 (2019), P12006. DOI: 10.1088/1748-0221/14/12/P12006. arXiv: 1908.00005 [hep-ex].

[142] A. Buckley et al. "A comparative study of Higgs boson production from vector-boson fusion." *JHEP* 11 (2021), p. 108. DOI: 10.1007/JHEP11(2021)108. arXiv: 2105.11399 [hep-ph].

[143] M. Shapiro and S. Todt. "Modelling of the vector boson scattering process $pp \to W^{\pm}W^{\pm}jj$ in Monte Carlo generators in ATLAS" (2018). URL: https://cds.cern.ch/record/2645279?.

Appendices

	Trigger chain	L1 seed	Available data range
0-btag	HLT_g25_medium_L1EM22VHI_4j35_0eta490_invm700	EM22VHI	data15 F3 - data16 F
	HLT_g25_medium_L1EM22VHI_4j35_0eta490_invm1000		data16 G - data18
1-btag	HLT_g25_medium_L1EM22VHI_j35_0eta490_bmv2c2077_3j35_0eta490_invm700	EM22VHI	data15 F3 - J
	HLT_g25_medium_L1EM22VHI_j35_0eta490_bmv2c2077_split_3j35_0eta490_invm700		data16
	HLT_g25_medium_L1EM22VHI_j35_0eta490_bmv2c1077_split_3j35_0eta490_invm700		data17 - data18
2-btag	HLT_g25_medium_L1EM22VHI_2j35_0eta490_bmv2c2077_2j35_0eta490	EM22VHI	data15 F3 - J
	HLT_g25_medium_L1EM22VHI_2j35_0eta490_bmv2c2077_split_2j35_0eta490		data16
	HLT_g25_medium_L1EM22VHI_2j35_0eta490_bmv2c1077_split_2j35_0eta490		data17 - data18
L1Topo	HLT_g20_tight_icaloloose_j15_gsc35_bmv2c1077_split_3j35_0eta490_invm500	EM18VHI	data17
	HLT_g20_tight_icaloloose_j35_bmv2c1077_split_3j35_0eta490_invm500	_MJJ-300	data18

Table .1: Unprescaled triggers targeting the VBF $H + \gamma$ signature during the full Run 2 data-taking period.

A Triggers Targeting VBF $H(b\bar{b}) + \gamma$ Signature

Various triggers were used during the Run 2 data taking periods to target the VBF H+photon signature.

B Sample List

B.1 AOD Samples

mc16a

- Z EWK bkg: mc16_13TeV.512002.aMCH7EG_PDF4LHC15_Zajj_EWK_NLO.recon.AOD.e8419_s3126_r9364
- Z QCD bkg: mc16_13TeV.344179.MGPy8EG_PDF4LHC15_A14NNPDF23LO_Zbbajj_QCD.merge.AOD.e5163_e5984_s3126_r9364_r9315
- bbjja bkg: mc16_13TeV.500561.MGPy8EG_PDF4LHC21_bbjja_QCD_LO.recon.AOD.e8482_s3126_r9364
- ccjja bkg: mc16_13TeV.508791.MGPy8EG_PDF4LHC21_ccjja_QCD_LO.recon.AOD.e8482_s3126_r9364
- ttH all-had bkg: mc16_13TeV.346343.PhPy8EG_A14NNPDF23_NNPDF30ME_ttH125_allhad.recon.AOD.e7148_a875_r9364
- ttH semi-lep bkg: mc16_13TeV.346344.PhPy8EG_A14NNPDF23_NNPDF30ME_ttH125_semilep.recon.AOD.e7148_a875_r9364
- ggH: mc16_13TeV.346302.PowhegPy8EG_NNLOPS_nnlo_30_ggH125_bb_EF_ph_20.merge.AOD.e7295_e5984_s3126_r9364_r9315
- NLO signal: mc16_13TeV.346485.aMcAtNloHerwig7EvtGen_PDF4LHC15_VBFHajj.merge.AOD.e7663_e5984_s3126_r9364_r9315

mc16d

- Z EWK bkg: mc16_13TeV.512002.aMCH7EG_PDF4LHC15_Zajj_EWK_NLO.recon.AOD.e8419_s3126_r10201
- Z QCD bkg: mc16_13TeV.344179.MGPy8EG_PDF4LHC15_A14NNPDF23LO_Zbbajj_QCD.merge.AOD.e5163_e5984_s3126_r10201_r10210
- bbjja bkg: mc16_13TeV.500561.MGPy8EG_PDF4LHC21_bbjja_QCD_LO.recon.AOD.e8482_s3126_r10201
- ccjja bkg: mc16_13TeV.508791.MGPy8EG_PDF4LHC21_ccjja_QCD_LO.recon.AOD.e8482_s3126_r10201

- ttH all-had bkg: mc16_13TeV.346343.PhPy8EG_A14NNPDF23_NNPDF30ME_ttH125_allhad.recon.AOD.e7148_a875_r10201
- ttH semi-lep bkg: mc16_13TeV.346344.PhPy8EG_A14NNPDF23_NNPDF30ME_ttH125_semilep.recon.AOD.e7148_a875_r10201
- ggH bkg : mc16_13TeV.346302.PowhegPy8EG_NNLOPS_nnlo_30_ggH125_bb_EF_ph_20.merge.AOD.e7295_e5984_s3126_r10201_r10210
- NLO signal: mc16_13TeV.346485.aMcAtNloHerwig7EvtGen_PDF4LHC15_VBFHajj.merge.AOD.e7663_e5984_s3126_r10201_r10210

mc16e

- Z EWK bkg: mc16_13TeV.512002.aMCH7EG_PDF4LHC15_Zajj_EWK_NLO.recon.AOD.e8419_s3126_r10724
- Z QCD bkg: mc16_13TeV.344179.MGPy8EG_PDF4LHC15_A14NNPDF23LO_Zbbajj_QCD.merge.AOD.e5163_e5984_s3126_r10724_r10726
- ttH all-had bkg: mc16_13TeV.346343.PhPy8EG_A14NNPDF23_NNPDF30ME_ttH125_allhad.recon.AOD.e7148_a875_r10724
- ttH semi-lep bkg: mc16_13TeV.346344.PhPy8EG_A14NNPDF23_NNPDF30ME_ttH125_semilep.recon.AOD.e7148_a875_r10724
- bbjja bkg: mc16_13TeV.500561.MGPy8EG_PDF4LHC21_bbjja_QCD_LO.recon.AOD.e8482_s3126_r10724
- ccjja bkg: mc16_13TeV.508791.MGPy8EG_PDF4LHC21_ccjja_QCD_LO.recon.AOD.e8482_s3126_r10724
- NLO signal: mc16_13TeV.346485.aMcAtNloHerwig7EvtGen_PDF4LHC15_VBFHajj.merge.AOD.e7663_e5984_s3126_r10724_r10726

B.2 DAOD Samples

mc16a

- NLO signal: mc16_13TeV.346485.aMcAtNloHerwig7EvtGen_PDF4LHC15_VBFHajj.deriv.DAOD_HIGG5D3.e7663_s3126_r9364_p4615
- bbjja bkg: mc16_13TeV.500561.MGPy8EG_PDF4LHC21_bbjja_QCD_LO.deriv.DAOD_HIGG5D3.e8482_s3126_r9364_p4615
- ccjja bkg: mc16_13TeV.508791.MGPy8EG_PDF4LHC21_ccjja_QCD_LO.deriv.DAOD_HIGG5D3.e8482_s3126_r9364_p4615
- Z EWK bkg: mc16_13TeV.512002.aMCH7EG_PDF4LHC15_Zajj_EWK_NLO.deriv.DAOD_HIGG5D3.e8419_s3126_r9364_p4615

mc16d

- NLO signal: mc16_13TeV.346485.aMcAtNloHerwig7EvtGen_PDF4LHC15_VBFHajj.deriv.DAOD_HIGG5D3.e7663_s3126_r10201_p4615
- bbjja bkg: mc16_13TeV.500561.MGPy8EG_PDF4LHC21_bbjja_QCD_LO.deriv.DAOD_HIGG5D3.e8482_s3126_r10201_p4615
- ccjja bkg: mc16_13TeV.508791.MGPy8EG_PDF4LHC21_ccjja_QCD_LO.deriv.DAOD_HIGG5D3.e8482_s3126_r10201_p4615
- Z EWK bkg: mc16_13TeV.512002.aMCH7EG_PDF4LHC15_Zajj_EWK_NLO.deriv.DAOD_HIGG5D3.e8419_s3126_r10201_p4615

mc16e

- NLO signal: mc16_13TeV.346485.aMcAtNloHerwig7EvtGen_PDF4LHC15_VBFHajj.deriv.DAOD_HIGG5D3.e7663_s3126_r10724_p4615
- bbjja bkg: mc16_13TeV.500561.MGPy8EG_PDF4LHC21_bbjja_QCD_LO.deriv.DAOD_HIGG5D3.e8482_s3126_r10724_p4615_r10724_p4615

- ccjja bkg: mc16_13TeV.508791.MGPy8EG_PDF4LHC21_ccjja_QCD_LO.deriv.DAOD_HIGG5D3.e8482_s3126_r10724_p4615

- Z EWK bkg: mc16_13TeV.512002.aMCH7EG_PDF4LHC15_Zajj_EWK_NLO.deriv.DAOD_HIGG5D3.e8419_s3126_r10724_p4615

C MadGraph Syntax

For each of the processes, the `p p >` notation indicates that a pair of protons are the initial state that generate the process to the right of the >. The Higgs boson, Z boson, b-jets, and c-jets are denoted with their standard letters, with the tilde marking anti-particles. The photon is `a` and jets are `j`. The `[QCD]` notation is used for NLO processes.

A maximum number of QCD or QED vertices allowed in the process is constrained by setting those values equal to an integer. For the ZbbjjaEWK sample, QCD=0 forces electroweak processes only by forbidding diagrams with any QCD vertices. For the ZbbjjaQCD sample, we limit QED=2 and QCD=10 so a maximum of 2 QED vertices involving photons and 10 QCD vertices are permitted in the Feynman diagrams. Higher orders would be smaller contributions and computationally expensive.

For the ZbbjjaQCD sample, the `p p > z a j j` process is an intermediate step since the `z > b b` notation indicates that the Z boson must decay to a pair of b-quarks in the final state.

The NonResbbjja and NonResccjja samples' $ notation excludes diagrams with a Z or Higgs boson from appearing in the s-channel, to avoid production of our VBF $H + \gamma$ signal or Zbbjja backgrounds.

D Signal Composition

D.1 Photons Radiating from b-quarks

Although photons radiating from b-jets would result in the same final state particles as our signal $H\gamma jj$ final state, we do not include this diagram in our analysis because the photon could not arise in MadGraph generation prior to $H \to b\bar{b}$ showering. The photon must exist in MadGraph 5 generation prior to showering with Herwig for our signal sample. Jet-photon isolation requirements would suppress the case where a photon exists in MadGraph generation and an additional photon radiates off a b-jet.

D.2 Pythia 8 LO and Herwig 7 NLO MC Comparison

Herwig 7 was used because of known strange third jet distributions using Pythia 8. In ATLAS $W^{\pm}W^{\pm}jj$ studies, the Zeppenfeld variable distribution varies greatly from that of all other generator/showering programs as shown by the dashed blue line in Figure .1. [143]. The MadGraph + Herwig 7 distribution is shown by the solid black line, and is much more consistent with other generators and showering programs, so we use that combination in the following studies for our own VBF analysis.

For our VBF $H + \gamma$ studies, Pythia 8 LO distributions were compared with Herwig 7 NLO distributions. Particularly of interest are the Pythia 8 LO and Herwig 7 NLO differences in the number of jets and p_T balance shown in Figure .2. The differences can be attributed to the Pythia 8 "dipole recoil" setting. The "dipole recoil" setting helps address the problem of too much hard and central radiation since only the

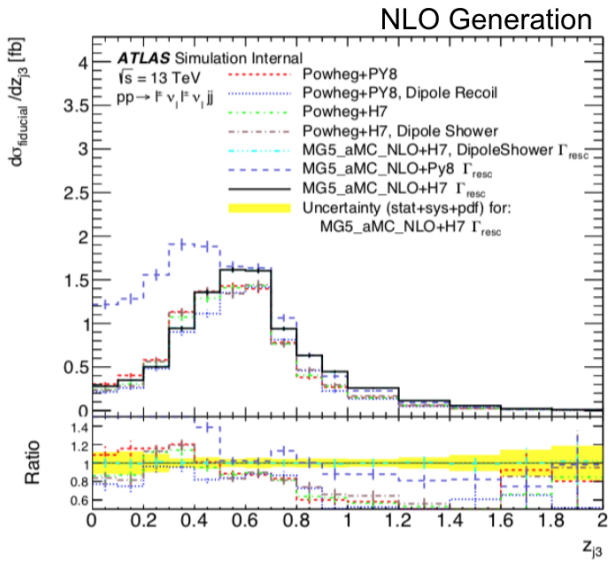

Figure .1: Third jet distributions using various generator and showering programs.[143]

final state parton recoils against the emission, and is expected to have better VBF jet modeling according to the LHCXSWG. Although the Zeppenfeld distributions have small differences, without the "dipole recoil" setting, the Pythia 8 LO sample distributions for p_T balance and number of jets differs dramatically from the Herwig 7 NLO sample distributions. With "dipole recoil", there is much better agreement between the Pythia 8 LO and Herwig 7 NLO distributions. For this reason, we use Herwig 7 for our MC sample.

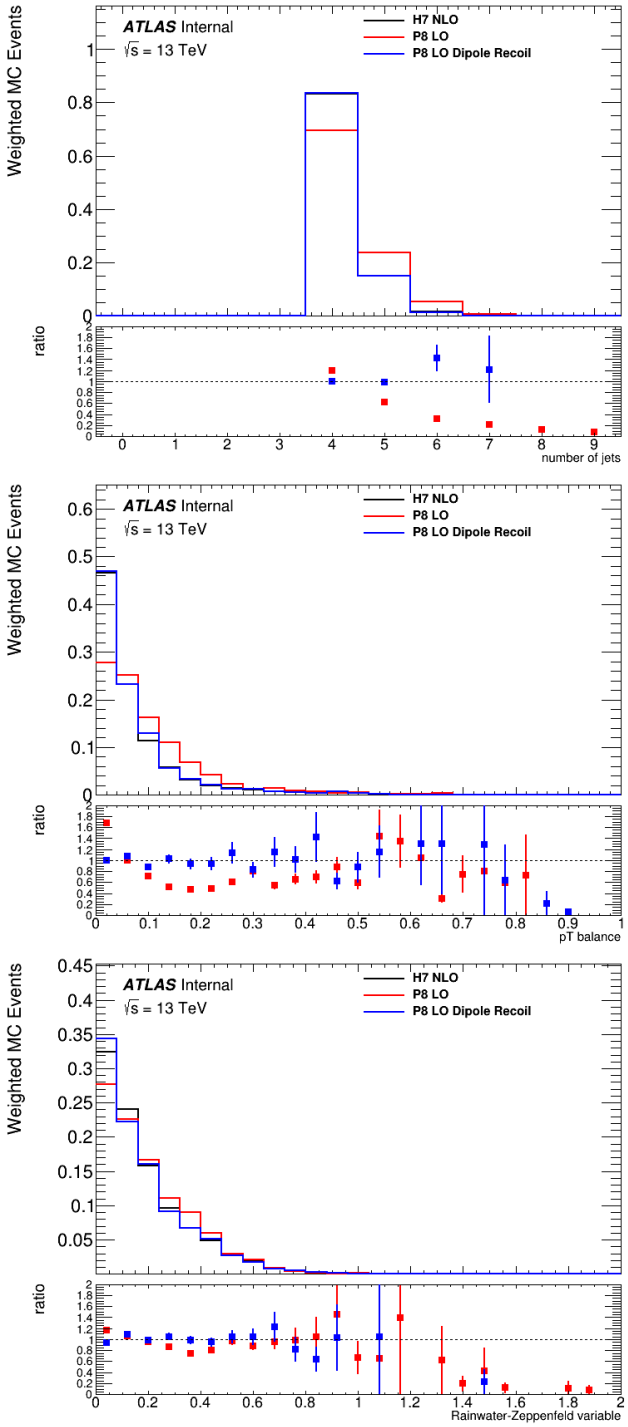

Figure .2: Truth-level comparison of Pythia 8 LO (with and without dipole-recoil) and Herwig 7 NLO MC distributions.

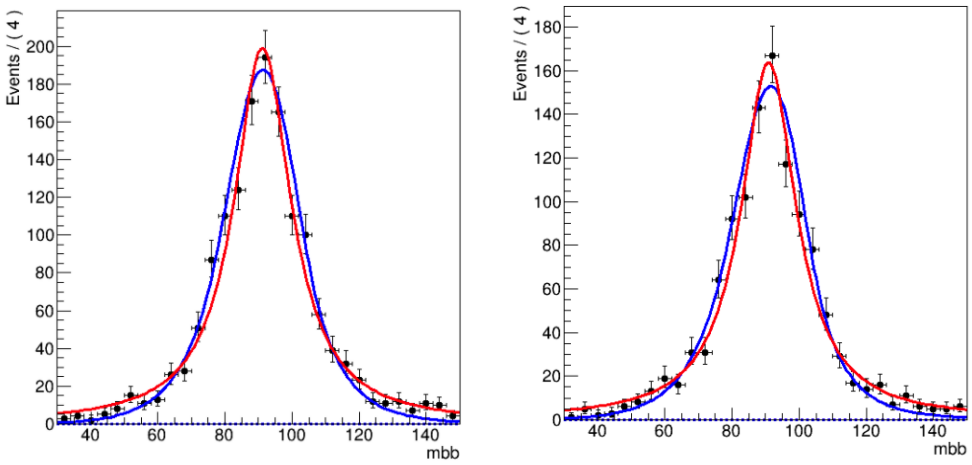

(a) EMTopo + MV2c10: $\sigma_p = 11.13 \pm 0.41$ (b) PFlow + DL1r: $\sigma_p = 10.86 \pm 0.50$

Figure .3: Bukin (blue) and Breit-Wigner (red) fits of Zγjj EWK peak comparing jet and b-tagging algorithms.

E Physics Object Selection

E.1 Jet Algorithms

The PFlow Jet algorithm and DL1r b-tagging was used for this legacy analysis. These updates decreased the Zγjj EWK peak width by about 3%. Both a Bukin fit and Breit-Wigner fit were checked and are shown in Figure .3.

E.2 Truth versus Direct Tagging

Studies were done comparing the effects of direct tagging to truth tagging on kinematic distributions. Truth tagging is advantageous when MC statistics are limited because b-jets that do not have a high enough value are given a "truth-tag" weight representing the likelihood of it being a b-jet, instead of being thrown out.

Sample	mc16a	mc16d	mc16e	Total
Direct Tag Signal	16.976	23.477	30.879	71.33
Truth Tag Signal	16.340	22.46	29.666	68.47
Direct Tag Background	14207.45	20258.73	26678.46	61144.64
Truth Tag Background	13101.86	18622.72	24481.04	56205.62

Table .2: Comparison of direct tagging and truth tagging methods show similar yields for mc16a, d, and e. Signal yields match within 5%, while background yields match within 8%.

Cut	Number of events	% of previous step
$p_T^J = 15$ GeV, $p_T^a = 20$ GeV, $m_{JJ} = 500$ GeV, & $p_T^{BB} = 0$	83535	8.44%
$m_{JJ} = 800$ GeV	36238	43.38%
p_T^a	24497	67.55%
p_T^J	8676	35.45%
p_T^{BB}	3474	40.04%

Table .3: Cutflow showing how many events pass each cut for a subset of the QCD $b\bar{b}\gamma jj$ sample.

Yield and shape were compared for weighted truth-tagged and direct-tagged signal (DSID 346485) and QCD background (DSID 344180) MC samples.

E.3 Cutflows

Cutflows show the number of events passing each cut, and are useful for determining where large portions of events are lost to cuts. In the QCD $b\bar{b}\gamma jj$ sample, the largest portion of events are lost from the jet p_T cut after the generator-level cuts as shown in Table .3.

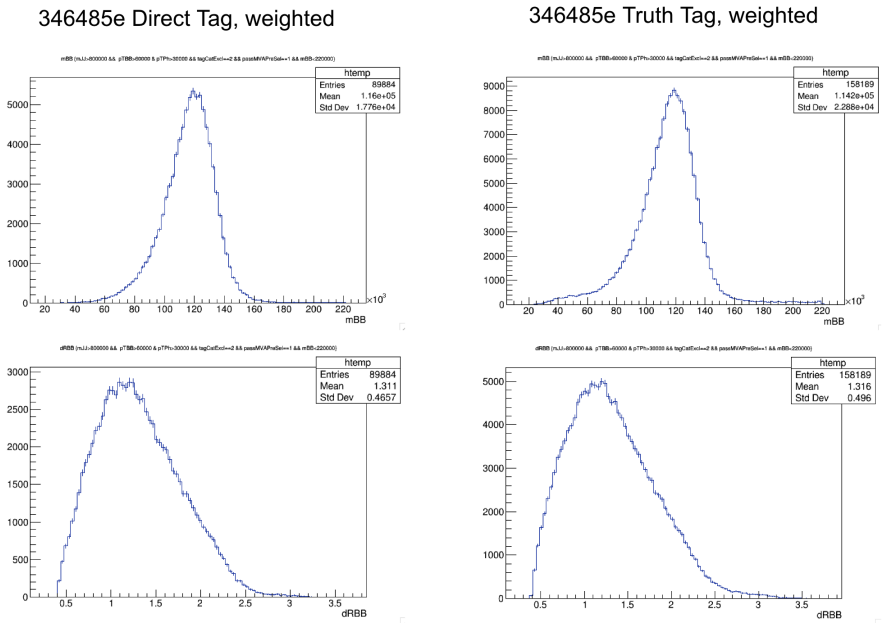

Figure .4: Truth tagging and direct tagging methods show similar m_{BB} and $dRBB$ shapes for signal and background MC samples after kinematic cuts. The low-end tail is slightly higher in the truth-tagged m_{BB} signal distribution, while the high-end tail is slightly higher in the truth-tagged $dRBB$ signal distribution.

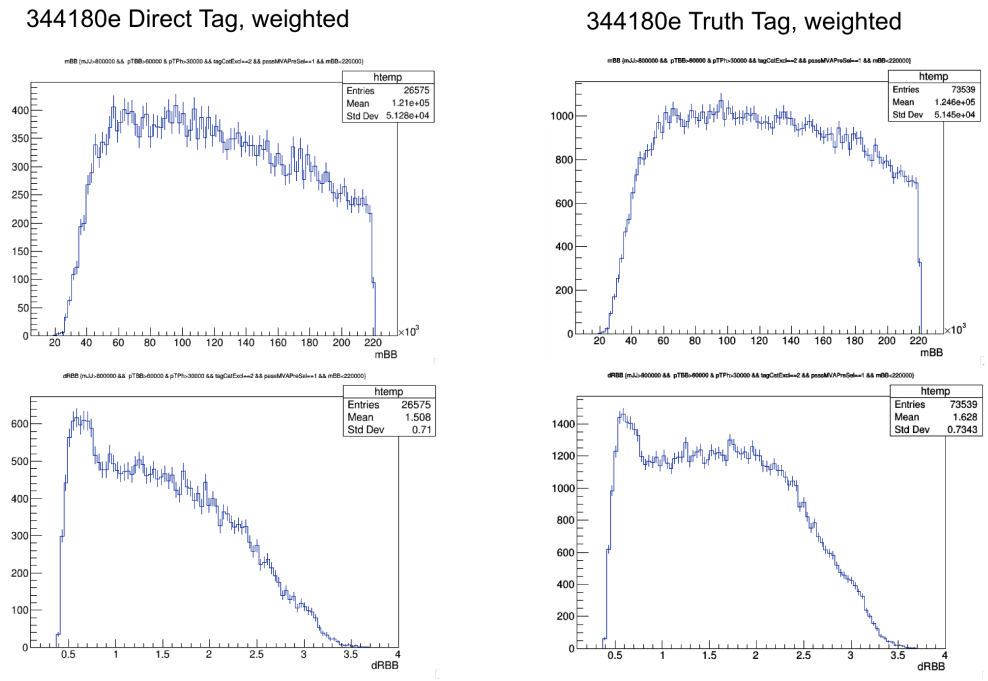

Figure .5: Truth tagging and direct tagging methods show similar m_{BB} and $dRBB$ shapes for signal and background MC samples after kinematic cuts. The background m_{BB} and $dRBB$ at distributions at higher values are slightly flatter in the truth-tagged distribution.

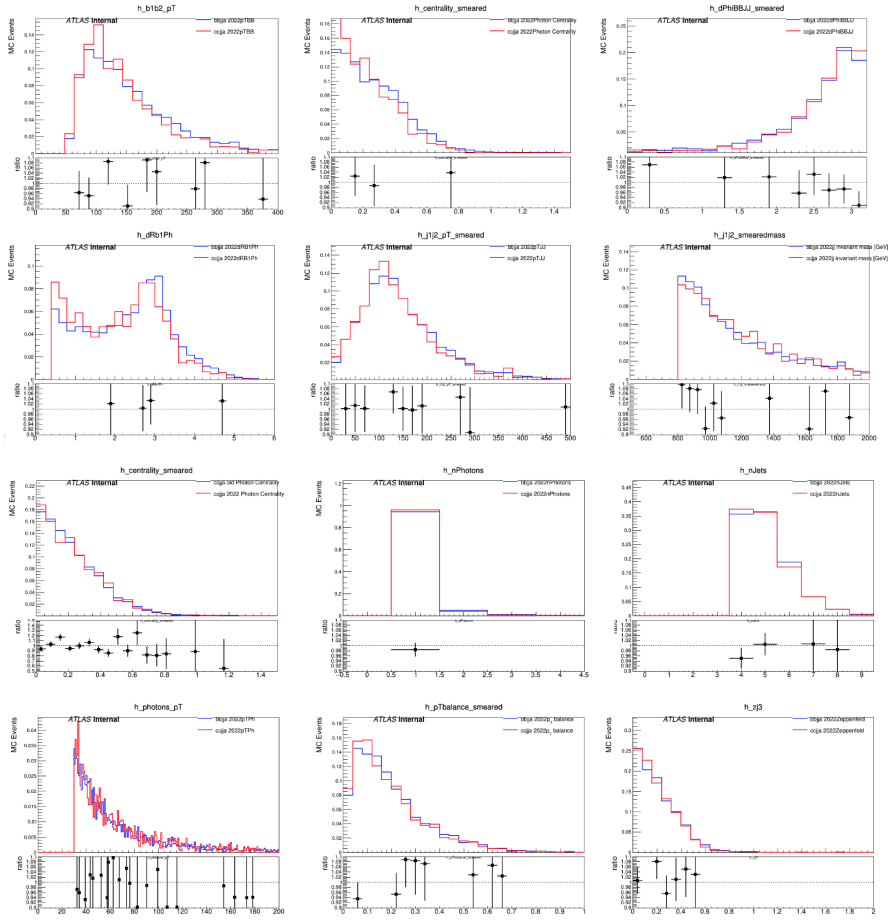

Figure .6: Comparison of $b\bar{b}\gamma jj$ and $c\bar{c}\gamma jj$ kinematic distributions.

F $b\bar{b}\gamma jj$ versus $c\bar{c}\gamma jj$ Kinematic Distribution Comparison

We compare the kinematic distributions for the two dominant backgrounds, $b\bar{b}\gamma jj$ and $c\bar{c}\gamma jj$. The differences in the distributions arise from the higher charge of the c-quark, making it more likely that photons will radiate off of the flavour-tagged jets rather than a non-flavour tagged jet. Thus, differences are most evident for distributions involving the photon relative to one of the jets, such as dRb1Ph or photon centrality.

G $c\bar{c}\gamma jj$ Contribution Calculation

The contribution from QCD multi-jet production from c-quarks in association with a photon is smaller than that of the QCD multi-jet production from b-quarks in association with a photon, as follows from these considerations:

- $\epsilon_{\text{tag}}(c) \sim 18.35\%$, for 77% b-tagging efficiency WP with DL1r tagger from 20-300 GeV
- $\epsilon_{\text{tag}}(b) \sim 78.19\%$.
- The ratio between $b\bar{b} + \gamma + jets$ and $c\bar{c} + \gamma + jets$ contributions is calculated as:

$$\frac{N(c\bar{c}\gamma jj)}{N(b\bar{b}\gamma jj)} = \frac{\epsilon_{\text{tag}}(c) \times \epsilon_{\text{tag}}(c) \times \sigma(c\bar{c}\gamma jj)}{\epsilon_{\text{tag}}(b) \times \epsilon_{\text{tag}}(b) \times \sigma(b\bar{b}\gamma jj)} = 0.055 \times \frac{\sigma(c\bar{c}\gamma jj)}{\sigma(b\bar{b}\gamma jj)} \tag{.1}$$

- Accounting for the cross section ratio, $\frac{\sigma(c\bar{c}\gamma jj)}{\sigma(b\bar{b}\gamma jj)}$, which is roughly 2.5 for electroweak production, the contribution from the $c\bar{c}\gamma jj$ process is about 13.8% of the $b\bar{b}\gamma jj$ contribution.

Because of the estimated 13.8% contribution, a new $c\bar{c}\gamma jj$ MC sample was generated for this legacy analysis as described in Section 5.2.2.